Max-Planck-Institut für Metallforschung
Stuttgart

Magnetism of amorphous and highly anisotropic multilayer systems on flat substrates and nanospheres

Edward Prabu Amaladass

Dissertation
an der
Universität Stuttgart

Bericht Nr. 222
Dezember 2008

Magnetism of amorphous and highly anisotropic multilayer systems on flat substrates and nanospheres

VON DER FAKULTÄT MATHEMATIK UND PHYSIK DER UNIVERSITÄT STUTTGART ZUR ERLANGUNG DER WÜRDE EINES DOKTORS DER NATURWISSENSCHAFTEN (DR. RER. NAT.) GENEHMIGTE ABHANDLUNG

Vorgelegt von

Edward Prabu Amaladass

geboren in Thachambady (Indien)

Hauptberichter:	Prof. Dr. G. Schütz
Mitberichter:	Prof. Dr. G. Denninger
Tag der mündlichen Prüfung:	10. Dezember 2008

Max-Planck-Institut für Metallforschung, Stuttgart

2008

I wish to dedicate this thesis to my late grand Father, Mr. M. Mariadoss, Indian Air Force. He taught me to persevere and prepared me to face challenges with faith and humility. He was a constant source of inspiration in my life. Although he is not here to give me strength and support I always feel his presence, which urges me to strive to achieve my goals in life.

கேடில் விழுச்செல்வம் கல்வி யொருவற்கு
மாடல்ல மற்றை யவை

திருவள்ளுவர்

Learning is wealth none could destroy
Nothing else gives genuine joy

Thiruvalluvar

Contents

Chapter 1

Introduction

1.1 Motivation

Magnetism has been the subject of a huge research effort due to various technological applications. Magnetic systems with reduced dimensions provide the building blocks for data storage technology, magnetic sensors, and spintronic applications. Due to the geometrical confinement, low dimensionality and proximity effects among different constituents, magnetic nanostructures often exhibit new and enhanced properties compared to the bulk counterpart [1, 2]. Engineering of such unique properties has already lead to many new technological innovations. Impressive examples are the giant magneto resistance (GMR) read heads used in computer hard disks [3–7] and tunneling magneto resistance (TMR) memory elements in non volatile magnetic random access memory (MRAM) [8, 9]. Employing GMR read heads has enabled a tremendous increase in the storage density to values of about 200 $Gbit/in^2$ [10, 11]. Due to this high impact, the invention of GMR by Peter Grünberg and Albert Fert has been acknowledged with the Nobel Prize in physics in 2007 [12].

The innovations in magnetism are fueled by scientific and technological developments in three key areas:

- Development of new magnetic materials with enhanced properties.
- Progress in theoretical understanding that facilitates exploring and designing the material properties.
- Development of novel experimental techniques to study nanoscale properties.

A brief overview about these three research areas is given in the following paragraphs.

The demand for miniature and high efficient motors for mechanical applications has triggered immense activities in hard magnetic materials such as NdFeB

or CoSm. In addition, soft magnetic materials that find their way in magnetic and magneto-optical recording, power electronics, and magneto-caloric refrigeration are also under continuous progress, e.g., CoNi, thin films and alloys of RE-TM systems, and permalloy. The need for spintronic devices has accelerated research on heterostructures like ferromagnet(FM)/antiferromagnet(AF), FM/semiconductor, FM/superconductor, and diluted magnetic semiconductors (DMS) such as ZnO and TiO_2 doped with 3-d transition metals (Co, Ni, and Fe), and Mn doped GaAs and Si. In addition, perovskite manganites such as $La_{1-x}Ca_xMnO_3$, $La_{1-x}Sr_xMnO_3$, and $Nd_{1-x}Sr_xMnO_3$ have gained attention due to the effect of colossal magnetoresistance and high spin polarization. These systems are also believed to have considerable potential applications in the sensor technology and in hybrid systems with semiconductors. A broad spectrum of applications have been anticipated from the development of molecular magnets based on metal-organic compounds like hexafluoroacetylacetonate or tetracyanoethylene. Furthermore, high density magnetic storage technology has raised immense interest on self-organized and nanostructured superlattices of FePt, CoPt, CoPd systems. Apart from electrical, electronical, mechanical, and optical applications, biocompatible nanomagnets offer attractive possibilities in the field of biomedicine. In particular, for laboratory diagnostics, drug delivery, tagging or labeling of the desired biological entity, and as contrast agent for magnetic resonance imaging (MRI). A prominent example is superparamagetic iron oxide nanoparticle (SPION).

The advancement of theoretical studies contribute to understand and analyze the properties of the nanostructures. For example, density functional theory (DFT) in the local spin density approximation plays a vital role in manifesting the electronic and magnetic properties of different complex systems. In addition, the advancement in supercomputers and parallel computing platforms simultaneously lead to the further development of the mean field theory, ab-initio quantum Monte Carlo, and micromagnetic simulation [14, 15]. Several scientific disciplines benefit from the calculation of intrinsic properties, phase diagrams, magnetic ground state, and magnetization process.

Experiments that can directly probe electronic and spin states as well as the magnitude of atomic magnetic moments and the magnetic micro structure have been reported. Especially, techniques based on synchrotron radiation, such as x-ray magnetic circular dichroism (XMCD), spin-resolved photoemission, magnetic scattering and surface diffraction have been proved to be unique tools to study the magnetic properties of a material with element specificity, high spatial and temporal resolution [2, 16]. Pump and probe experiments such as time resolved XMCD, and magneto optical Kerr effect (MOKE) are reported to be viable techniques to address time domain information with picosecond ($10^{-12}s$) and femtosecond ($10^{-15}s$) resolution. Also recent developments in scanning probe techniques such as magnetic force microscopy (MFM), and spin polarized scanning tunneling microscopy and spectroscopy (SP-STM/STS) have succeeded in

resolving the magnetic properties of single magnetic atoms [17, 18].

Technological developments in many frontiers of information technology create a huge demand for fast, non volatile, high capacity, low power consumption, long stability, and cost efficient memory devices. Existing classes of nonvolatile memory devices include magnetic memory devices, such as hard disk drives (HDD), semiconductor memory devices like FLASH, optical and magneto optical memory devices, like compact disk (CD), digital versatile disk (DVD),High-definition digital versatile disk (HD DVD), and Blue-ray disk. None of the above mentioned memory technologies satisfy all the demands simultaneously, indeed the subtle balance causes some techniques to lead the market. For example, the high capacities and low price per bit achieved by magnetic storage techniques has a higher priority than the fast access and write time offered by semiconductor memories like FLASH drives. However, due to the declining price, very high density FLASH memories are also feasible in near future. In the following section the challenges and the future techniques of magneto-optical and magnetic recording are described briefly.

Magneto-optical recording

Magneto-optical (MO) recording is a technique combining magnetic and optical recording. In the writing process the MO media is subjected to a magnetic field and simultaneously heated by a laser. When a small region of the magnetic medium is heated by a focused laser, the saturation magnetization M_s and the coercive field H_c decreases. By applying a magnetic field during the heating, the magnetic medium in the local region is magnetized along the field direction, as shown schematically in Fig. 1.1 (b). Two kinds of recording methods namely light intensity modulation (LIM) and magnetic field modulation (MFM) have been used. In the former one, the laser intensity is modulated according to the recording signal and in the later one the applied field is modulated. During the process of reading, the Magneto-Optical Kerr effect[1] is utilized. The unique temperature dependence of many properties, the amorphous nature, and the perpendicular magnetic anisotropy (PMA) found in RE-TM binary and ternary systems (e.g., TbFeCo, FeGd, FeTb and DyFe alloys and multilayer system) makes them well suited for MO recording.

Achieving higher density MO recoding is a two fold process. First the spot size of the laser in the process of writing has to be reduced and secondly, very small domain patterns have to be read with high signal to noise ratio. Solid immersion lenses (SIL), and recent developments in superlenses have lot of potential to improve the writing process beyond the diffraction limit [19, 20]. To overcome the difficulties in the read out process, new techniques have been devel-

[1]When a linearly polarized light is reflected from a magnetic media the polarization angle is rotated. By using polarizers and photodiodes the rotation can be detected as the change in the intensity of the light.

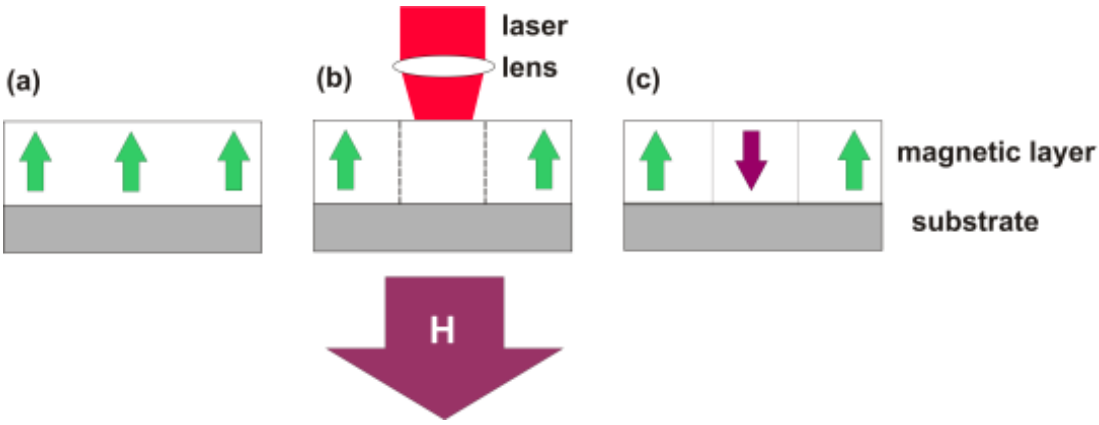

Figure 1.1: *Schematic diagram of a thermomagnetic recording (a) before, (b) during writing, and (c) after writing. The reduction in the M_s and H_c upon heating causes the magnetization in the medium to align with the external field direction.*

oped. They incorporate at least two magnetic layers. One is a recording layer to store the information, and the other is a read out layer to detect the information. Both layers are coupled by either exchange or magnetostatic interaction. Some of these techniques are magnetic superresolution (MSR), magnetic amplifying magneto optical system (MAMMOS), and domain wall displacement detection (DWDD). In MSR technique a temperature dependent spin reorientation transition from in-plane to out-of-plane magnetization direction is used to transfer the magnetic information from the recoding to the readout layer. In the other two techniques domain wall expansion phenomena are used during the readout process. New hybrid techniques that combine the MO recording and the GMR readout techniques are also proposed for higher density.

Magnetic recording

As mentioned before, the storage density in the present hard disks has already attained several hundreds Gbit per $inch^2$ (Gb/in^2). In future it is expected to reach the Terabyte regime (Tb/in^2). The recording head and the magnetic media are the two key devices controlling the miniaturization and the exponential growth of the hard disk density. Continued advancements of hard disk drives require even higher densities and thus smaller bits. The energy barrier between the two magnetic states used to store the bits is given by

$$\Delta E \propto K_{eff} V, \tag{1.1}$$

where K_{eff} and V represents the effective magnetic anisotropy and the particle volume, respectively. As the magnetic grains in the magnetic media become

smaller, the volume V decreases. Consequently, the energy barrier ΔE reduces and the random thermal vibration at ambient temperature overcomes the energy barrier, ΔE. As a result, the magnetic orientation reverses, which is known as the superparamagnetic effect (SPE) [21].

To overcome the constrains imposed by the SPE and to increase the areal density (bits/inch^2), different methods have been realized, e.g., perpendicular magnetic recording, patterned media, and thermal assisted writing.

Perpendicular magnetic recording

In 1975 Iwasaki and Takemura proposed the perpendicular recording technology for higher storage density as well as to reduce the demagnetizing field caused by the shrinking of the bit size [22, 23]. The bits are stored perpendicular to the film surface, whereas in the conventional longitudinal media they are stored in the film plane. Two different types of media have been considered for the use in this recording systems. Type 1 consists of a recording media with uniaxial perpendicular magnetic anisotropy (PMA) deposited on a high permeable, soft magnetic under layer as shown schematically in Fig. 1.2. The soft under layer (SUL) guides the magnetic flux from the write pole to the collector pole and theoretically doubles the write field. Magnetic materials with high uniaxial PMA such as Co alloys (CoPt, CoPd, CoCrPt, CoCrTa, CoCrNb, CoCrPtNb, CoCrPtB) [24], and Fe alloys (FePt, TbGdFe, TbFe, and GdFe) [25–27] are some of the promising candidates for perpendicular magnetic recording. Materials that are magnetically soft such as NiFe, CoFe, CoFeB etc are under investigation to be used as SUL. Type 2 is similar to type 1 without the SUL and uses a conventional ring head as in longitudinal media. For more detail refer to [24, 28, 29].

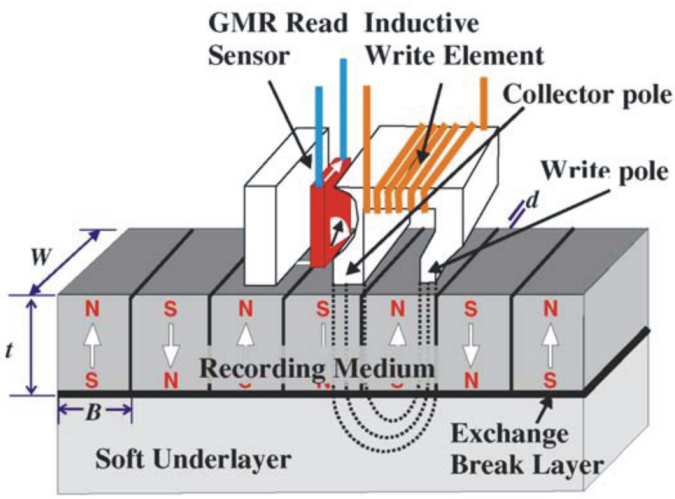

Figure 1.2: *Schematic illustration of a perpendicular media with a write and read head flying above the media, t is the thickness of the material, W is the width of the recorded track and B is the size of a bit. The bits are stored perpendicular to the disk plane [2].*

Thermal assisted writing

According to Eqn. 1.1, a material with a high PMA (K_u) can overcome the superparamagnetic limit due to its high K_{eff}. However, the large switching field resulting from the high K_u of the material remains as a big challenge for current writing heads. In order to circumvent this problem heat assisted writing, as discussed in the section about MO recording is used [31, 32].

Patterned media

Another promising method to overcome the SPE is the use of patterned media. Here the bits are stored on predefined magnetic nanostructures, contrary to conventional media where the bits are stored in a granular film [30]. Fig. 1.3 shows a schematic diagram of a patterned media, where each element stores one bit. For instance, magnetization up (+M) represents 1 and magnetization down (-M) represents 0. In conventional recording, the bit boundary is determined by the grain boundary which causes randomness in the bit positions called transition jitter. On the other hand, if the magnetic entities are perfectly patterned and isolated from each other, the bit boundary is the isolating space and the jitter can be reduced. Another major difference between conventional and patterned media recording schemes is that, in conventional media, the signal to noise ratio (SNR) will decrease if the track width is reduced. On the other hand, in patterned media, the SNR does not change even if the track width is reduced.

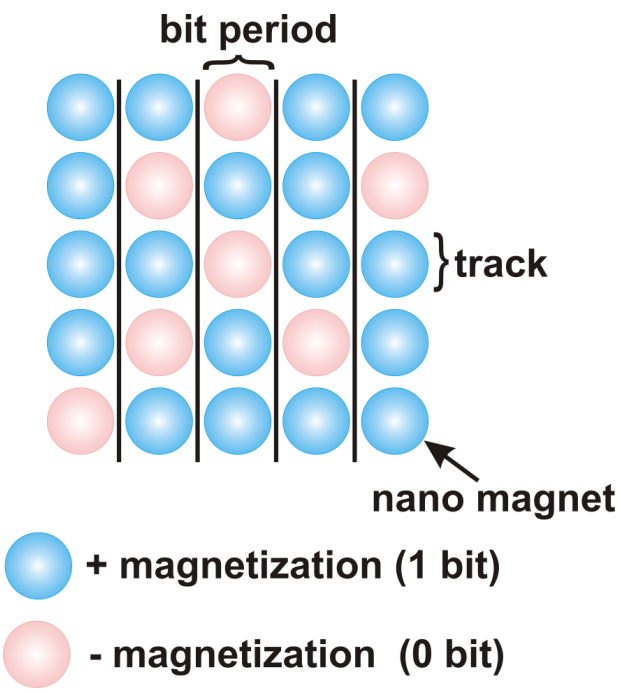

Figure 1.3: *Schematic diagram of a patterned media in which the bits are stored on predefined magnetic nanostructures. Magnetization up (+M) represents 1 and magnetization down (-M) represents 0.*

Many companies have increased the density by using perpendicular magnetic media as described above. This has already pushed the SPE to higher limits. Most likely, the next technology for high storage density is the patterned media.

A wide range of new techniques and methods have been reported to produce magnetic nanostructures [33]. "*Top down*"-approaches which comprise lithographic techniques like, focused ion beam lithography(FIB), e-beam lithography [34, 35], x-ray lithography [36], interference or holographic lithography [37] have been widely used. However, all these techniques are slow, expensive, and allow only structuring of small areas. In contrast, structuring by "*bottom up*" techniques can overcome these draw backs. Several methods have been proposed, for example, micellar and reverse micellar techniques to produce magnetic nano clusters [38, 39], the use of anodic porous alumina as a mask for film deposition [40], and the use of nanospheres (e.g., polystyrene, silica) as a mask for film deposition [41]. These techniques are capable of patterning large areas in a quick, simple and cost-effective way. Albrecht *et al.* [42] proposed a new method, analogous to the sphere lithography where, by depositing magnetic thin films on self-assembled nanospheres, a new class of magnetic nanostructures with crescent shaped cross section is formed. The curved nature of the substrate and the diameter of the spheres provide additional degrees of freedom to tailor the hard and soft magnetic properties of the material. Fe/Gd and Co/Pt multilayers deposited on nanopsheres are studied in this thesis. More emphasis is given to the Fe/Gd system.

1.2 Aim and outline of the thesis

Fe/Gd multilayer films show many interesting properties such as the presence of a compensation temperature (T_{comp}), perpendicular magnetization, a very low H_c, a high spin density, and the existence of different magnetic phases, as well as a spin reorientation transition (SRT) as a function of either the film thickness, the composition, or the temperature. So far very few studies have been done on amorphous Fe/Gd multilayers and even less on nanostructures [43–47]. The primary aim of this thesis is to study the magnetic properties of Fe/Gd films with a thickness of few nanometers deposited on flat substrates and on self-assembled nanospheres in a systematic way.

The thickness and temperature dependent SRTs, the domain configuration during these transitions and the structural changes in the multilayers shall be studied in detail on flat substrates. In order to see the influence of the curved nanostructures the magnetic properties of an in-plane and out-of-plane magnetized Fe/Gd system shall be investigated on self-assembled nanospheres. Emphasis shall be given to the changes in the magnetization reversal mechanism and the magnetic anisotropy by varying the diameter of the spheres and the thickness of the layers.

Chapter 2 describes the basic theoretical aspects of magnetism which are relevant in the context of this work. It includes the different energy terms in micromagnetism, the theory of domains, and various reversal mechanisms. In addition, the basics of micromagnetic simulations are explained.

Chapter 3 gives a brief description of the different characterization techniques used in this thesis, which include magneto optical Kerr effect (MOKE), superconducting quantum interface device (SQUID), low angle x-ray reflectivity (XRR), transmission x-ray microscope (TEM), and magnetic imaging techniques based on x-ray magnetic circular dichroism (XMCD). In XMCD imaging, the theoretical aspects of the XMCD effect, basics of synchrotron radiation and principles of two different x-ray microscopies, namely scanning transmission x-ray microscopy (STXM) and x-ray photo emission electron microscopy (X-PEEM) are briefly explained.

Chapter 4 describes and discusses the experimental results of Fe/Gd multilayers deposited on flat silicon substrates. After a brief description of the magnetic properties of FeGd systems, the sample preparation technique is explained. More emphasis is given to experimental and simulation studies of thickness and temperature driven SRTs. The domain configuration during the SRT is imaged with X-PEEM and compared with micromagnetic simulations. Furthermore, XRR and TEM measurements are carried out to address the temperature driven changes in the layered structure of the magnetic film.

Chapter 5 addresses the properties of perpendicularly and in-plane magnetized Fe/Gd films, deposited on self-assembled nanospheres. The spin structure of Fe/Gd systems and its reversal mechanism has been studied by STXM as a function of the size of the nanospheres and the thickness of the Fe/Gd multilayers. In addition, experimental results are compared with micro magnetic simulations.

The last part of the thesis, chapter 6, explains the magnetic properties of Co/Pt multilayers deposited on self-assembled nanospheres. The sample preparation and the simulations presented in this chapter are done in collaboration with T.C. Ulbrich from the University of Konstanz. SRTs at a nanoscale level on each individual sphere are studied by STXM and compared with micromagnetic simulations. After a short summary and outlook in chapter 7 the thesis ends with bibliographic references, appendices and acknowledgments.

Chapter 2

Micromagnetic theory

2.1 Energetics of Ferromagnetism

Micromagnetics and domain theory are governed by the well established Landau-Lifshitz equation [48]. The reduced magnetization of a magnetic system $\mathbf{m(r)} = \mathbf{M(r)}/\mathbf{M}_s$, with $\mathbf{M}_s$ denoting the saturation magnetization, is chosen to minimize the total free energy under the constraint $\mathbf{m(r)}^2 = 1$. The total free energy of a ferromagnet is given by

$$E_{Tot} = \int \left[\underbrace{E_{ex}(\mathbf{m})}_{exchange} + \underbrace{E_{an}(\mathbf{m})}_{anisotropy} + \underbrace{E_h(\mathbf{m})}_{Zeeman} + \underbrace{E_d(\mathbf{m})}_{strayfield} + \underbrace{E_{stric}(\mathbf{m})}_{magnetostrictive} \right] dV \tag{2.1}$$

2.1.1 Exchange energy

Exchange energy is purely quantum mechanical in origin. According to Pauli's principle and Coloumb interaction, the magnetic moments in a ferromagnet tend to align parallel to each other (in anti ferromagnets-anti parallel). Any deviation from this ideal case invokes an energy penalty, which can be described by the stiffness expression [49]:

$$E_{ex} = \mathbf{A}\nabla(\mathbf{m})^2 \tag{2.2}$$

where A is a material constant, the so-called exchange stiffness constant.

2.1.2 Anisotropy

In a magnetic sample the magnetization $\mathbf{M}$ tends to lie along one or several axes. It costs energy to turn it into any direction different from the preferred axis, called *easy axis*. The energy necessary to rotate the magnetization direction from the easy into the hard axis is defined as the magnetic anisotropy energy. The energy density E_{an} is an even function of the angle θ enclosed by $\mathbf{M}$ and the magnetic axes as shown in the Fig. 2.1:

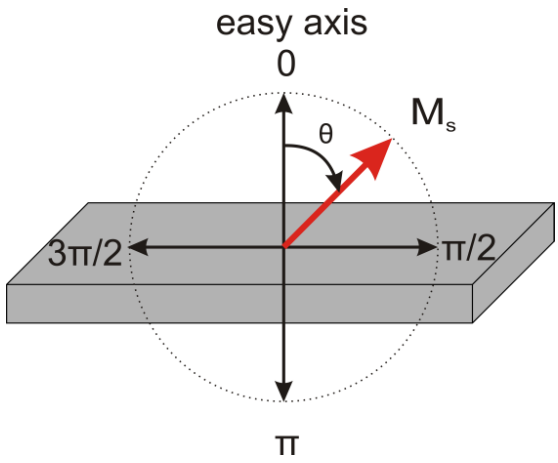

Figure 2.1: *The direction of saturation magnetization M_s with respect to a easy axis of the sample [50].*

$$E_{an} = K_1 sin^2\theta + K_2 sin^4\theta + K_3 sin^6\theta + ..., \tag{2.3}$$

where K_i (i=1,2,3,...) are the anisotropy constants.

The first term K_1 in Eqn. 2.3 is usually much larger than the other terms. The anisotropy term can be approximately written as:

$$E_{an} = K_{eff} sin^2\theta = (K_u + K_d) sin^2\theta \tag{2.4}$$

where K_{eff} is the macroscopic measurable effective anisotropy and it is the sum of the magneto crystalline anisotropy (K_u) generated by the atomic structure and bonding and the shape anisotropy $K_d = -\mu_0 M_s^2 N/2$. N is the demagnetization factor.

In thin films and multilayers K_u may be positive and large. If $(K_u + K_d)>$ 0, the film is magnetized perpendicular to the sample plane but for $(K_u + K_d)<$ 0, it is magnetized in the sample plane. Therefore, the easy magnetization axis of a sample is determined by the competition between the magneto-crystalline anisotropy, the shape anisotropy and the interface anisotropy.

The micromagnetic origin of the magnetic anisotropy in transition metals has been debated ever since the early work of Van Vleck suggesting that the spin-orbit interaction is the origin of magneto crystalline anisotropy (MCA). The Bruno model states that the orbital moment is larger along the easy magnetization direction, and that the difference between the orbital moments along the easy and hard directions is proportional to the magneto crystalline anisotropy [51].

2.1.3 Zeeman or external field energy

The interaction energy of the magnetization with the external field H_{ex} is known as the Zeeman energy or the external field energy:

$$E_H(m) = -\mu_0 \int H_{ex} \cdot M dV \tag{2.5}$$

It is reduced when all the magnetic moments align parallel to the external field.

2.1.4 Magnetostatic energy

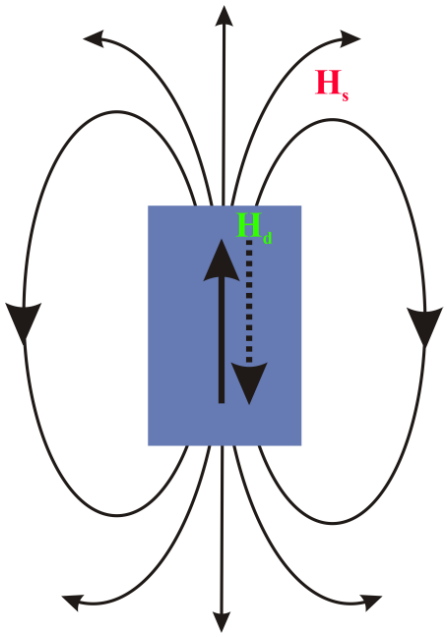

Figure 2.2: *Stray field and demagnetizing field in a magnetic sample.*

The stray field energy is connected with a magnetic field generated by the magnetic body itself. The field H is called H_d (demagnetizing field) inside and H_s (stray field) outside the magnetic material as shown in the Fig. 2.2. The magnetic stray field H_s generated by a magnetic body contains energy. The total energy E_d is given by

$$E_d = \frac{\mu_0}{2} \int_{allspace} H^2 dV = -\frac{1}{2}\mu_0 \int_{sample} H_d \cdot M dV \tag{2.6}$$

2.1.5 Magnetostrictive energy

Magnetostriction is the property of magnetic materials that causes them to deform under the influence of a magnetic interaction and vice versa. This deformation leads to an energy term, E_{stric} that contains symmetric and asymmetric tensors. For more detail refer to [49].

2.2 Domain Theory

Magnetic material is often subdivided into magnetic domains in which the magnetization is uniform. Domains are formed in order to reduce the free energy of a magnetic system. Each energy term in Eqn. 2.1 has its own criterion to reduce the total energy of the system as given below,

- Exchange energy (E_{ex}) is minimized when all the magnetic moments $\mathbf{m}$ over the entire body are aligned parallel to each other.
- Anisotropy energy (E_{an}) is minimized when the local magnetic moments align to a certain preferred direction known as easy axis.
- Magnetostatic energy (stray field energy) (E_d) is minimized when a magnetization follows a closed path (no net magnetic moment) inside the body.
- Zeeman energy (E_H) is minimized when all the magnetic moments align parallel to the external field.

Therefore, the competition between the various energy terms gives rise to different ground states such as (a)uniform magnetization (single domain), (b) domain structure, and (c) vortex structure as shown in the Fig. 2.3.

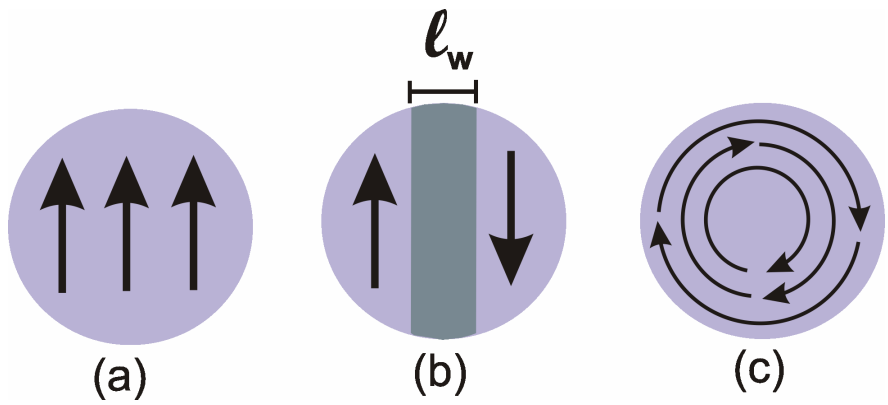

Figure 2.3: *Various domain configurations in a disc (a) uniform magnetization, (b) domain structure, (c) vortex structure [52].*

Domain walls, the region in which the magnetization changes continuously are formed between domains to reduce the magneto static energy. To rotate the magnetization by $\gamma = \pi$ it has to enclose an angle $0 < \gamma < \pi$ with the easy axis over a distance of l_W. When the magnetic anisotropy energy is large, the moments are strongly held along the easy axis. The wall width l_W will be small to minimize the length of the rotation from the easy axis. When the exchange energy between the moments is large the moments will form a stiff chain that

resists bending, so the wall thickness l_W will be large to minimize the wall energy. Hence the width of a domain wall is determined by the competition between the exchange and anisotropy energies:

$$l_W = \pi\sqrt{\frac{A}{K_u}} \tag{2.7}$$

The pre-factor in Eqn. 2.7 depends on the definition of domain wall width, here the classical definition introduced by Lilley is used [49, 53]. Domain walls in bulk material generally scale with the exchange length of the anisotropy energy:

$$l_{ex1} = \sqrt{\frac{A}{K_u}} \tag{2.8}$$

In thin films the shape anisotropy, K_d, is dominant and therefore the domain wall scales with the exchange length of the stray field:

$$l_{ex2} = \sqrt{\frac{A}{K_d}} = \sqrt{\frac{2A}{\mu_0 M_s^2}} \tag{2.9}$$

More detailed explanations on theory of magnetic domains can be seen in [49].

2.3 Magnetization process

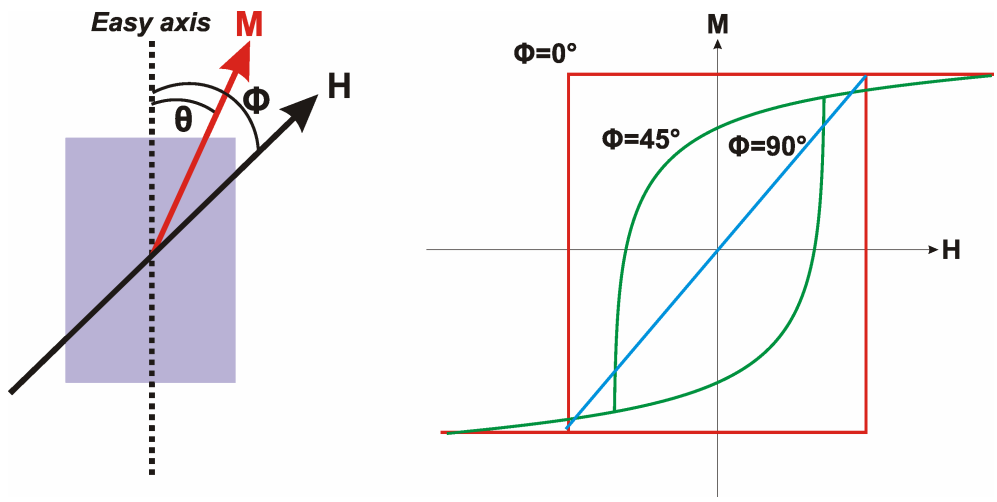

Figure 2.4: *Dependence of the component of **M** along the direction of the applied field **H** on the field strength according to the Stoner-Wohlfarth model.*

The magnetization process is the result of complex and intricate rearrangements that involve a large number of degrees of freedom, in principle the whole

vector field ***M(r)*** characterizing the magnetization state of the body. Basic reversal mechanisms are (a) coherent rotation (Stoner-Wohlfarth model), (b) nucleation and (c) domain wall motion.

Coherent rotation (Stoner-Wohfarth Model): Magnetic samples that are smaller than the characteristic lengths defined in Eqns. 2.8 and 2.9, behave like a single domain particle. On applying external magnetic fields the magnetization changes are then expected to occur solely by uniform rotation of M.

For the simplest case of a sample with uniaxial anisotropy constant K which includes shape and crystalline contributions, the energy of a single domain particle with magnetization M and volume V, in a magnetic field H, is given by

$$E = KVsin^2\theta - MVHcos(\phi - \theta) \tag{2.10}$$

where θ and ϕ are the angles enclosed by M and H, respectively, with easy axis of magnetization as shown in Fig. 2.4. The magnetization loop depends on the orientation ϕ of the external field relative to the easy axis (Fig. 2.4).

Nucleation: In contrast to coherent rotation of magnetic moments, in an uniformly magnetized sample, domains of opposite magnetization nucleate under the influence of an external field. Figure 2.5 shows the Kerr images of a Fe/Gd sample in which the magnetization reversal takes place by nucleation processes. At remanence an uniform magnetization is noticed in Fig. 2.5 (a). Upon increasing the magnetic field, see Fig. 2.5 (b)-(d), domains of opposite magnetization nucleate and reach a saturated state.

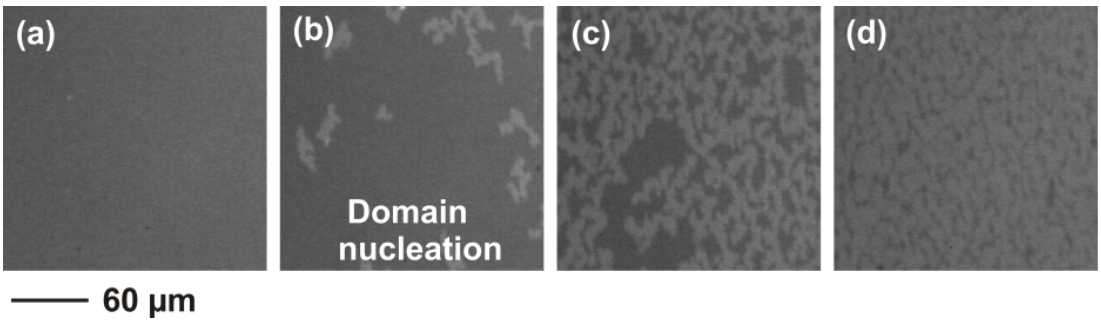

Figure 2.5: *(a)-(b), Images of a Fe/Gd sample taken by a Kerr microscopy show the magnetization reversal by nucleation. The external perpendicular magnetic field H_{ex} is increased on moving from left to right, (a) 0 Oe (remanence state), (b) 50, (c) 110, and (d) 180 Oe.*

Domain wall motion: Magnetic samples larger than the critical length possess domains separated by domain walls. In the simplest case consider there are two domains with opposite magnetization as shown in Fig. 2.6. On applying an in-plane external magnetic field, domains with magnetization close or parallel to the field direction expand at the expenses of other domains with opposite magnetization by domain wall motion, see Fig. 2.6 (a)-(d).

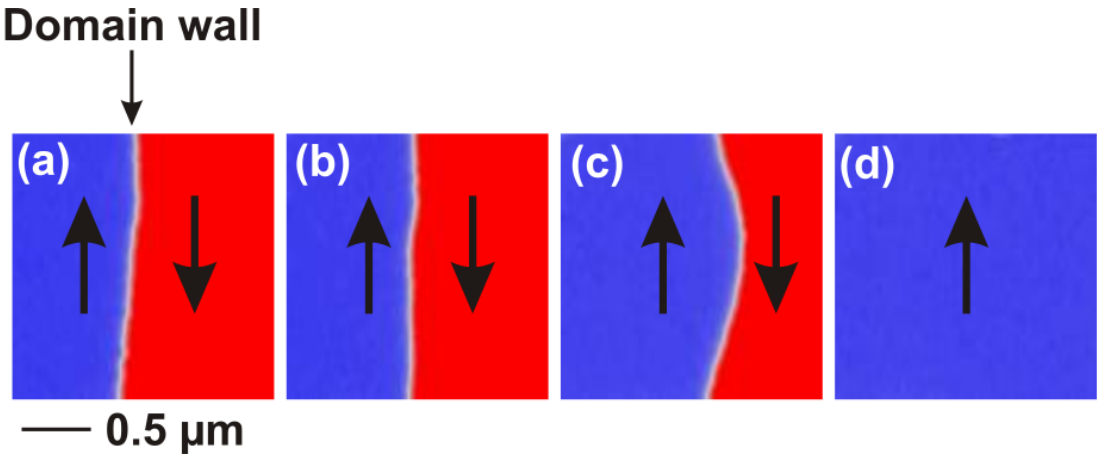

Figure 2.6: *(a)-(d), images of a Fe/Gd sample taken by x-ray microscopy show the motion of a domain wall, i.e, the light line between the color coded blue and red domains. The external in-plane magnetic field H_{ex} is increased on moving from left to right, (a) 0 Oe (remanence state), (b) 62 Oe , (c) 338 Oe, and (d) 600 Oe. The arrows denote the magnetization direction within a domain.*

2.4 Micromagnetic simulation

The program developed by Sebastian Macke at the Max-Planck-Institute for Metals Research and the program MAGPAR [54] have been used for micromagnetic simulations. These softwares use the hybrid finite element method (FEM)/boundary element method (BEM)[1]. Therefore, there are three steps necessary to simulate a magnetic nanostructure, namely pre-processing, simulation, and post processing. In pre-processing, the desired structure is modeled geometrically and discretized into small elements called cells. Consider for example a circular disk shaped magnetic nanostructure with a diameter of 200 nm and a thickness of 25 nm. Using a mesh generation softwares like GID [55] or NETGEN [56] a disk of required size is defined geometrically and discretized into small tetragonal volume elements with a side length of 15 nm as shown in Fig. 2.7. The size of each cell in the mesh is a crucial parameter because within the micromagnetic simulation, the magnetization inside each cell is considered to be uniform. Therefore, the average cell size should always be smaller than the exchange lengths given in Eqns. 2.8 and 2.9.

The mesh data created in the previous step and the material parameters the anisotropy constant (K_u in units of J/m^3), exchange constant (A in units of J/m^3), saturation magnetization (M_s in units of A/m), and the damping term (α dimensionless parameter) are necessary input parameters for the simulation. In order to study the magnetization dynamics, variational calculus of the total

[1]The hybrid solver takes the strengths of both FEM and BEM. The BEM handles the open regions and linear solution while the FEM handles the non-linear areas.

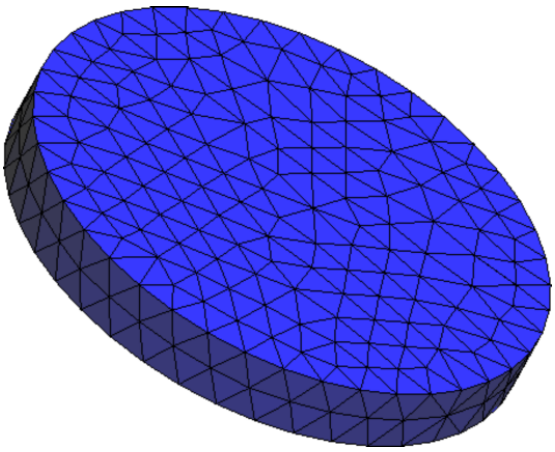

Figure 2.7: *Finite element mesh for a circular disk.*

free energy (Eqn. 2.1) with boundary conditions [49] derives a set of differential equations. The solution of the variational problem takes the form of a stability condition to be fulfilled at equilibrium. This condition is expressed in terms of an effective field $H_{\mathbf{eff}}$, defined at each point inside the body [52].

$$H_{\mathbf{eff}} = \frac{2}{\mu_0 M_s}\nabla \cdot (A\nabla m) - \frac{1}{\mu_0 M_s}\frac{\partial F_{an}}{\partial m} + H_{\mathbf{ex}} + H_{\mathbf{d}} \tag{2.11}$$

where F_{an} is the anisotropy energy density, $H_{\mathbf{ex}}$, $H_{\mathbf{d}}$ are the external and the stray field, respectively. The effective field exerts a torque on the magnetization. For the system to be in equilibrium, this torque must be zero.

$$m \times H_{\mathbf{eff}} = 0 \tag{2.12}$$

Dynamically, the angular momentum connected with the magnetic moment will lead to a gyrotropic reaction if a torque $m \times H_{\mathbf{eff}}$ exists, which is described by the following equation:

$$\frac{\partial m}{\partial t} = \gamma_G m \times H_{\mathbf{eff}} \tag{2.13}$$

where $\gamma_G = \mu_0 g_e/m_e \cong$ -2.21 10^5 $\mathrm{mA^{-1}s^{-1}}$.

By introducing a damping factor α which describes the local or quasi-local dissipative phenomena like relaxation at magnetic impurities or scattering of spin waves on the lattice defects, Eqn. 2.13 leads to the so called *Landau-Lifshitz-Gilbert* equation.

$$\frac{\partial m}{\partial t} = \gamma_G m \times H_{\mathbf{eff}} - \alpha m \times m \times H_{\mathbf{eff}} \tag{2.14}$$

Using numerical methods, the solution of Eqn. 2.14 is computed for each element of the mesh.

Finally, in post-processing, the output files from the simulation are viewed by paraview [57] and microavs [58] visualization tools.

Chapter 3

Characterization techniques

Structural characterization

3.1 X-ray reflectivity (XRR)

When X-rays are incident on a surface of a thin film at grazing incidence, most of them are reflected. The plot of the reflected intensity as a function of the incident angle, gives information about the film thickness, interface roughness, intermixing and the density of the sample [59]. Consider α_i and α_f are the incident and exit angle of an X-ray on a flat surface as shown in the inset of Fig. 3.1. If the corresponding wave vector are $\vec{k_i}$ and $\vec{k_f}$, respectively, the momentum transfer along the z direction is given by

$$\left|\vec{Q_z}\right| = \left|\vec{k_f} - \vec{k_i}\right| = \frac{4\pi}{\lambda} sin\alpha_i \tag{3.1}$$

For an ideal, flat interface the Fresnel reflection coefficient r is given by

$$r = \frac{r_z - r_z^{'}}{r_z + r_z^{'}} \tag{3.2}$$

where r_z and $r_z^{'}$ are the projection of incident and transmitted light onto the z direction respectively. The reflected intensity is given by

$$R = |r|^2 \tag{3.3}$$

For $\alpha_i < \alpha_c$ (critical angle), total external reflection takes place and the transmitted reflection coefficient $r_z^{'}$ is purely imaginary. Above the critical angle the reflectivity falls off rapidly by

$$R \propto \frac{1}{\alpha_i^4} \tag{3.4}$$

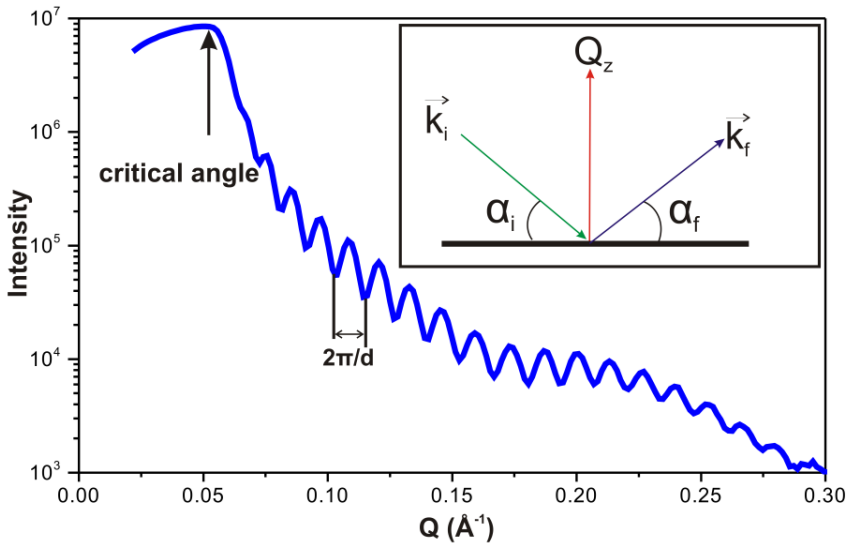

Figure 3.1: *The X-ray reflectivity curve measured on a Fe/Gd multilayers deposited on a silicon substrate. The geometry is shown in the inset where α_i and α_f are the incident and exit angle of an X-ray and $\vec{k_i}$ and $\vec{k_f}$ are the corresponding wave vector. Q_z the momentum transfer along the z direction.*

If the sample has more than one interface, the waves from different interfaces interfere constructively and destructively, and lead to an oscillation in the reflected intensity, as seen in Fig. 3.1. These oscillations are called "*Kiessig fringes*". Their periodicity in Q_z is related to the thickness of the sample d by

$$Q = \frac{2\pi}{d} \tag{3.5}$$

The shape of the *Kiessig fringes* depends upon many important parameters such as the interface roughness and the intermixing of the individual layers. If a periodic structure of layers with different refractive indexes, such as ABAB....ABAB are prepared, Bragg reflection is seen in the low angle reflectivity plot. The angle at which the Bragg peak occurs is related to the period of the multilayer (t_A+t_B).

3.2 Transmission electron microscopy (TEM)

A conventional Transmission electron microscope (TEM) is composed of an electron gun, magnetic lenses, apertures and a sample holder. If a thin sample is illuminated with an electron beam, some electrons transmit directly through the specimen and some interact with the atoms of the specimen by scattering, diffraction and absorption processes. Images are formed either by a direct beam or by

the scattered electrons [60]. There are two different modes in TEM, the diffraction and the image mode. Diffraction mode is used to get the diffraction pattern of the sample, whereas the lattice structures and grain boundaries are imaged in the image mode. In this thesis only the imaging mode has been used.

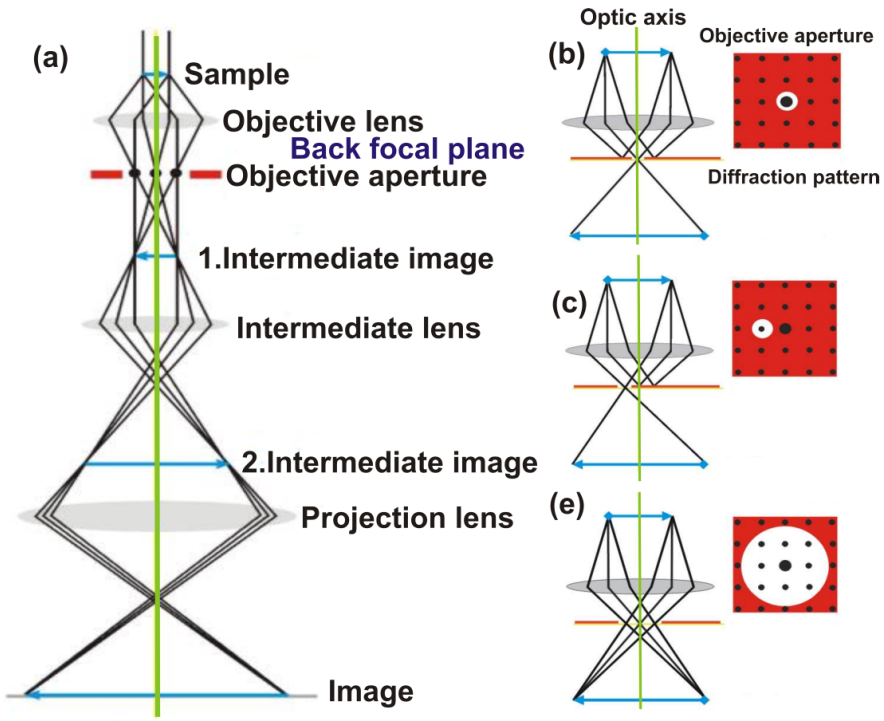

Figure 3.2: *Ray diagram of a TEM operating in image mode (a). Three basic imaging modes of TEM: bright field image (b), dark field image (c) and high resolution image (d) [61]. In bright field image (BF), the diffracted beam is blocked by the objective aperture and only the direct beam passes through the sample. In the dark field image, the transmitted beam is blocked and the image is formed by the diffracted beam. By choosing a large objective aperture the interference between the direct and the diffracted beam results in a high resolution image.*

Figs. 3.2 shows the ray diagrams of a TEM operating in the image mode. The three basic images obtained in TEM are the bright field image, the dark field image and the high resolution image. In bright field image (BF), the objective aperture is placed on the back focal point of the objective lens so that the diffracted beam is blocked and only the direct beam passes through the sample. In such case the contrast in the image is due to the thickness variation and the scattering difference. In the dark field image, the transmitted beam is blocked and the image is formed by the diffracted beam by moving the object aperture or by tilting the beam direction. By selecting spots in the diffraction pattern, the dark field image gives information about the size or the shape of specific grains.

The high resolution image can be obtained by choosing a large objective aperture. The image is formed by the interference between the transmitted and the diffracted beam. High resolution TEM images are used to study complex micro structures such as interfaces, oxide films and multilayers in atomic range. Figs 3.2 (b)–(e) show the ray diagrams of the three different TEM imaging modes.

Magnetic characterization

3.3 Magneto optical Kerr effect (MOKE)

When linearly polarized light interacts with a magnetic film, the polarization of the light becomes elliptically and the principle axis rotates. This change is called *Magneto optical effect*. Depending upon the direction of magnetization and the measurement geometry, the magneto optical effect is named *Faraday effect* in transmission and *Kerr effect* in reflection mode, as shown in Fig. 3.3 (a), and (c)-(e). In *Voigt effect* or *linear birefringence*, the magnetization direction is perpendicular to the beam direction as shown in Fig.3.3 (b).

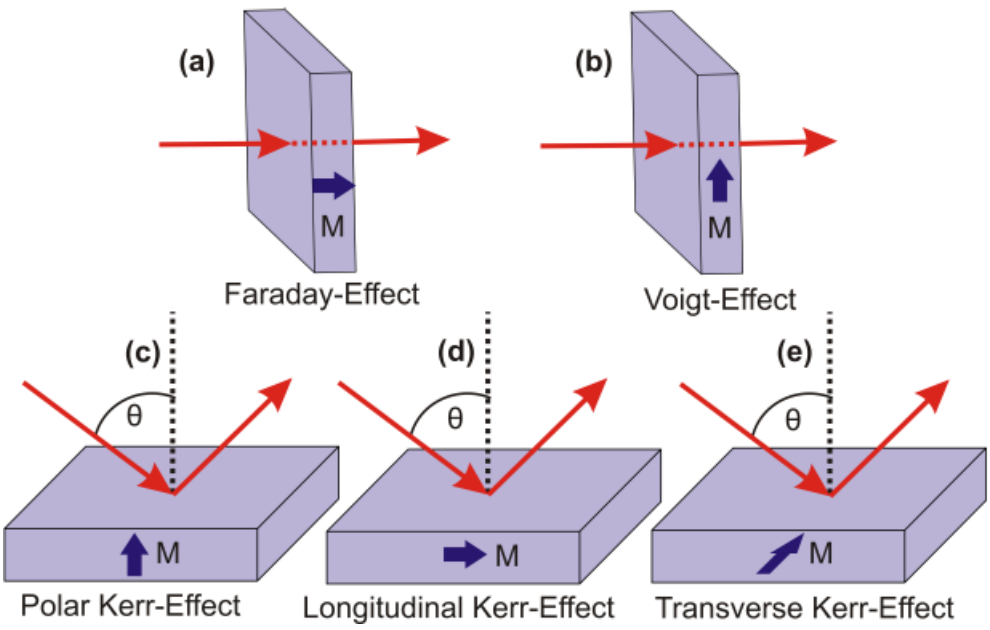

Figure 3.3: *Geometrical illustrations of different magneto-optical-effects. (a) Faraday-effect, (b) Voigt-effect, (c) Polar Kerr-effect, (d) Longitudinal Kerr-effect and (e) Transverse Kerr-effect.*

In reflection mode, depending on the magnetization direction with respect to the sample plane and the plane of incidence the magneto optical Kerr ef-

fect (MOKE) has three different geometries, namely polar MOKE, longitudinal MOKE and transverse MOKE, (see (c)-(d) in Fig. 3.3). In polar MOKE the magnetization direction is perpendicular to the sample plane and parallel to the plane of incidence whereas, in the longitudinal MOKE the magnetization is parallel to the sample plane and the plane of incidence. In the case of transverse MOKE the magnetization is parallel to the sample plane and perpendicular to the plane of incidence.

Upon reflection the polar and longitudinal geometry yield orthogonally polarized components therefore they are widely used. Since the transverse geometry affects only the amplitude of incident polarization it is scarcely used. The samples studied in this thesis are magnetized perpendicular to the sample plane. Therefore, polar MOKE has been used to characterize the samples as explained below [49][62].

If the magnetization is oriented perpendicular to the surface, a linearly polarized light beam will induce electrons to oscillate parallel to the plane of polarization, i.e., the plane of the electric field E of the light. Regularly reflected light is polarized in the same plane as the incident light. Let $\mathbf{r}$ be the amplitude vector of this magnetization-independent reflected light. The Lorentz force induces a small component of vibrational motion perpendicular to the primary motion and to the direction of magnetization. This secondary motion, which is proportional to $v_{Lor}=-M\times E$, generates secondary amplitude known as Kerr vector $\mathbf{k}$ as shown in Fig. 3.4. The values of $\mathbf{r}$ and $\mathbf{k}$ dependent on the sample and the optical arrangement used to probe the sample (Polar or Longitudinal MOKE). The value of $\mathbf{k}$ solely depends upon the magnetization of the sample. Therefore, change in the magnetization direction will change the sign of $\mathbf{k}$. For simplicity, consider two anti-parallel directions. Vectorial addition of $\mathbf{k}$ and $\mathbf{r}$ gives amplitude reflection vector r_A and r_B for opposite magnetization direction which makes an angle θ_K with $\mathbf{r}$. θ_K is referred as Kerr rotation angle. An analyzer $\mathbf{P}$ positioned with a polarization angle φ with respect to $\mathbf{k}$ also makes an angle Ψ_A and Ψ_b with r_A and r_B, respectively.

The transmitted optical amplitude through the analyzer is given by

$$t_A = r_A cos(90 - \varphi - \theta_k) = r_A sin(\varphi + \theta_k) \tag{3.6}$$

$$t_B = r_A sin(\varphi - \theta_k) \tag{3.7}$$

Therefore, the transmitted intensity through the analyzer for opposite magnetization is

$$I_A = I_0^2 sin^2(\phi + \theta_k) \tag{3.8}$$

$$I_B = I_0^2 sin^2(\phi - \theta_k) \tag{3.9}$$

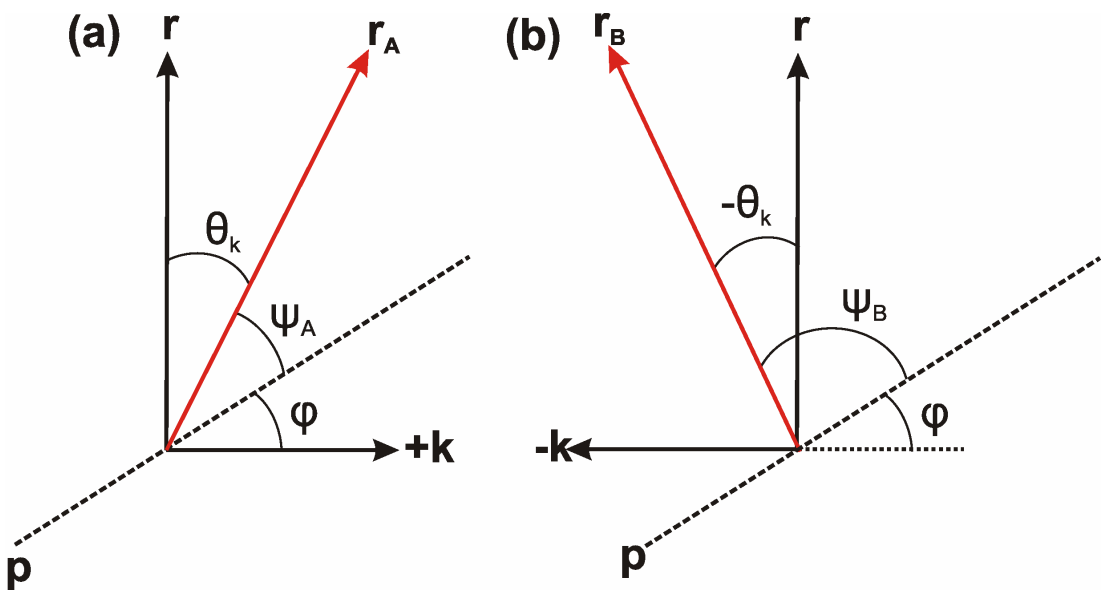

Figure 3.4: *Schematic diagram of polarized light amplitude vector reflected from samples with opposite magnetization (a) and (b) [62].*

since $I_0 \propto r_A^2 = r_B^2$.

The average of I_A and I_B is

$$\overline{I} = \frac{I_0}{2}(1 - cos(2\phi)cos(2\theta_K)) \tag{3.10}$$

The difference between I_A and I_B is called the MOKE Signal

$$\Delta I = I_0 sin(2\phi)sin(2\theta_K) \tag{3.11}$$

By dividing Eqn. 3.11 with Eqn. 3.10 one gets the normalized MOKE signal.

$$\frac{\Delta I}{\overline{I}} = \frac{2I_0 sin(2\phi)sin(2\theta_K)}{(1 - cos(2\phi)cos(2\theta_K)} \approx \frac{4\theta_K}{tan\phi}(\text{for small } \theta_K) \tag{3.12}$$

Therefore, the normalized MOKE signal is directly proportional to the Kerr rotation (θ_K) which in turn is proportional to the magnetization of the sample. Different techniques have been employed to detect the Kerr angle θ_K.

A schematic diagram of the MOKE setup used in this thesis is shown in Fig. 3.5 [63]. The signal to noise ratio is increased by using lock-in techniques. The polarized laser beam is modulated by an electro optical modulator and split into two beams of light using a beam-splitter. One of the beams is used as a reference signal whereas the other beam of light is reflected back from the sample mounted between the pole pieces of the electromagnet. The difference between the reference signal and the reflected signal gives the Kerr angle θ_K, which is proportional to the magnetization of the sample.

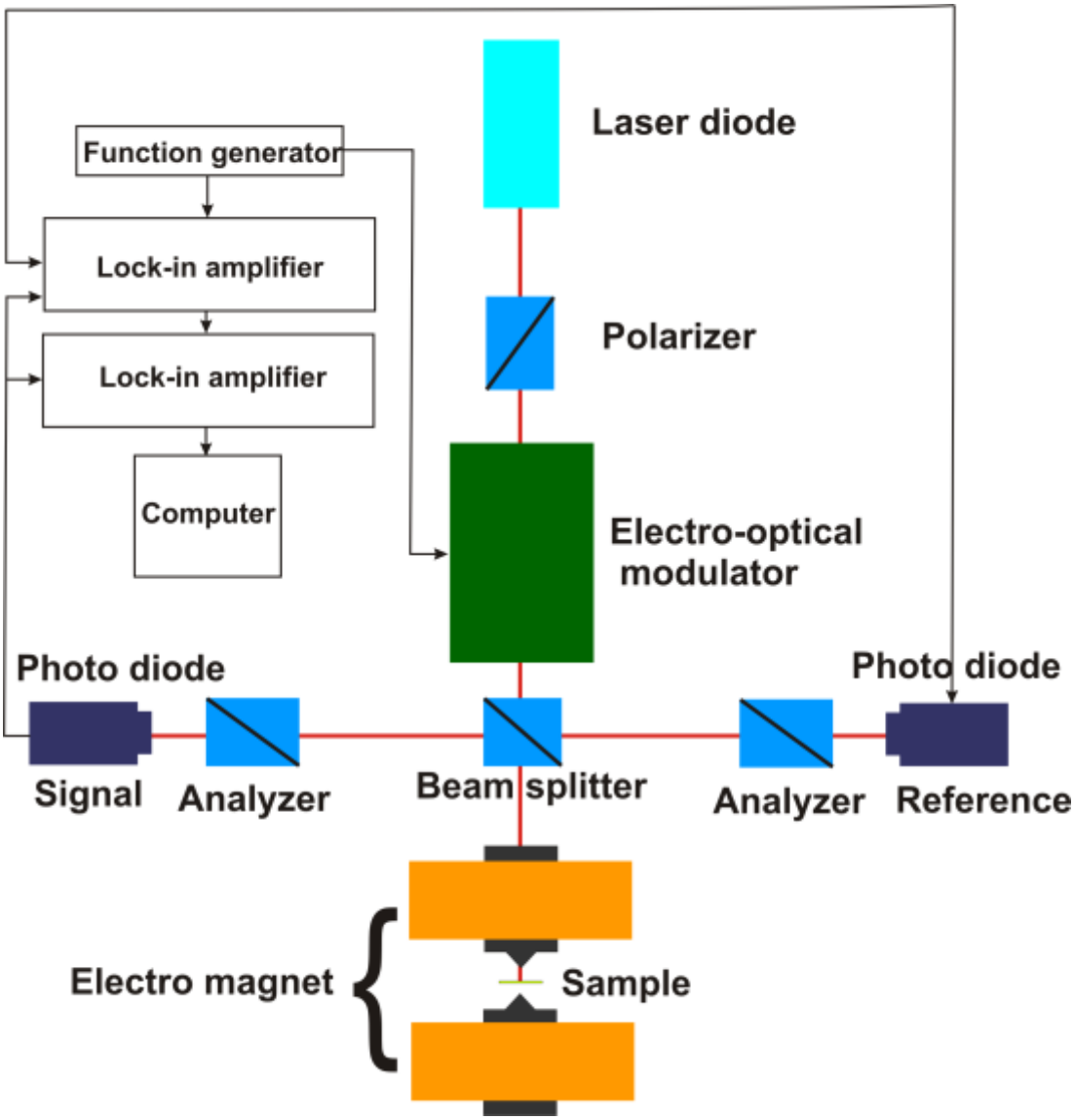

Figure 3.5: *Schematic diagram of a polar MOKE. The signal to noise ratio is increased by using lock-in techniques. The polarized laser beam is modulated by an electro optical modulator and split into two beam of light using a beam-splitter. One of the beams is used as a reference signal whereas the other beam of light is reflected back from the sample mounted between the pole shoes of the electromagnets. The difference between the reference signal and the reflected signal gives the Kerr angle θ_K, which is proportional to the magnetization of the sample.*

3.4 Superconducting quantum interference device (SQUID)

A commercial Superconducting quantum interference device (SQUID) from Quantum design is used to determine the magnetic hysteresis loops and temperature dependence of the magnetization. The working principle is based on flux quantization and Josephson tunneling [64]. Flux quantization is a process in which magnetic flux threading a closed superconducting ring is quantized in units of one flux quantum, $\Phi_0 = \frac{h}{2e}$=2.07×10^{-15} Wb, where h is Planck's constant and $2e$ is the charge of a Cooper pair. Thus, on cooling a superconducting ring in a magnetic field below the superconducting temperature and then removing the field, a persistent supercurrent exists in the ring with flux quanta $n\Phi_0$, where n is an integer number. On applying an external magnetic flux the supercurrent adjusts itself so that the net flux remains $n\Phi_0$.

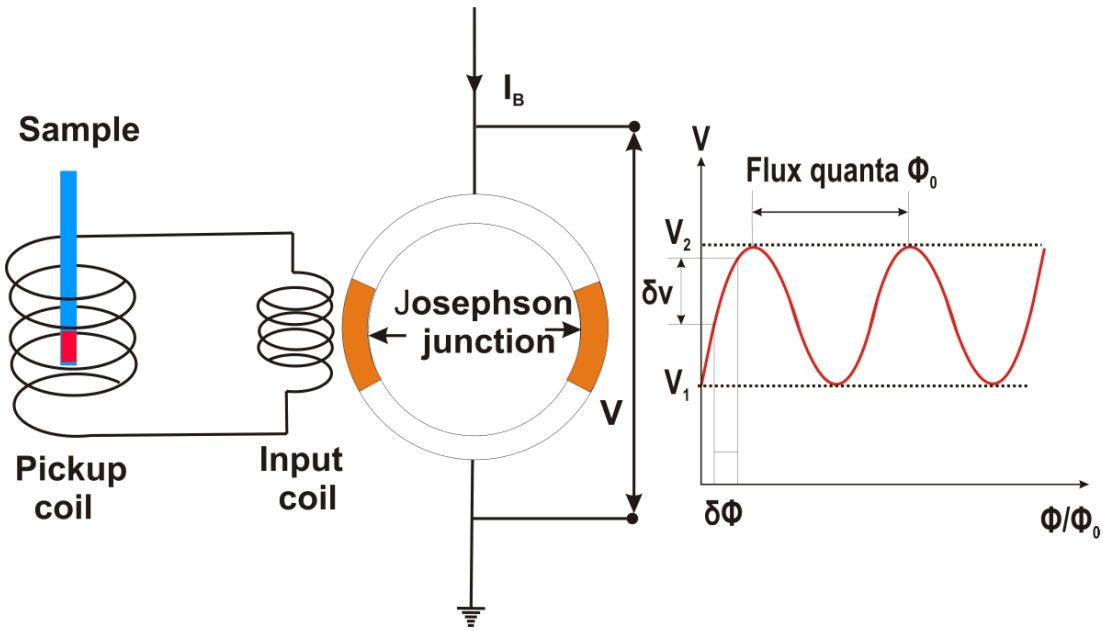

Figure 3.6: *Schematic diagram of SQUID magnetometer in which the superconducting detection coil is inductively coupled to the Josephson junctions in a parallel connection. By moving the sample through the superconducting pickup coil, the magnetic moment in the sample induces an electric current in the superconducting circuit which in turn changes the magnetic flux in the SQUID sensor through the input coil. The critical current in the sensor oscillates with a period of* Φ_0*. If the SQUID is biased with a current* I_B*, the voltage correspondingly oscillates between* V_1 *and* V_2*. Any change in the flux* $\partial\Phi$ *is proportional to the change of voltage* ∂V*.*

The Josephson junction consists of two superconducting materials separated by a thin insulator. Cooper pairs tunnel coherently through the junction and maintain the supercurrent I_0, which is the zero voltage current. When the current exceeds I_0 a voltage is created at the junction and the super current oscillates at a frequency $2e.V/h = V/\Phi_0$ which is called Josephson effect.

A SQUID consists of two Josephson junctions connected in parallel which are inductively coupled to the superconducting detection coil as shown in Fig. 3.6. By moving the sample through the superconducting pickup coil, the magnetic moment in the sample induces an electric current in the superconducting circuit which in turn changes the magnetic flux in the SQUID sensor through the input coil. The critical current in the sensor oscillates with a period of Φ_0. If the SQUID is biased with a current I_B, the voltage correspondingly oscillates between V_1 and V_2 as shown in Fig. 3.6. Any change in the flux $\partial\Phi$ is proportional to the change of voltage ∂V. With the help of modern electronics the SQUID sensor is capable of detecting very small magnetic moments ($\leq 10^{-15}$ Tesla).

3.5 X-ray imaging techniques

X-rays were a remarkable discovery by Röntgen in 1895 at the university of Würzburg. In the electromagnetic spectrum they occupy a region between the extremely ultraviolet radiation and the Gamma radiation. Fully polarized and tunable X-rays from synchrotrons serve as a cutting edge tool to study the magnetic characteristics of materials. In this section, the interaction of X-rays with matter, basics of x-ray magnetic circular dichroism (XMCD), and synchrotron radiation are addressed. In addition, two different x-ray microscopic techniques namely, scanning transmission x-ray microscopy (STXM) and x-ray photoemission electron microscopy (X-PEEM) are explained briefly.

3.5.1 Interaction of X-rays with matter

In the non-relativistic x-ray energy regime, i.e., below 0.1 $m_e c^2 \approx 50$ keV, the interaction of electromagnetic radiation with matter of thickness t is determined by photo absorption and can be described by Beer's law:

$$I(E, Z) = I_0 e^{-\mu(E,Z)t} \tag{3.13}$$

The absorption coefficient μ strongly depends on the atomic number of the absorbing atom and the energy of the incident photon E. Since the energy regime of x-ray photons includes the energies of many atomic resonances, x-ray techniques are element selective and also sensitive to the chemical state of an atom which depends on the binding energy of the inner core level.

For photons with a wave vector $\mathbf{q}$, energy $\hbar\omega$, and polarization π, the absorption coefficient $\mu^{\mathbf{q}\pi}$ can be calculated using Fermi's Golden Rule within first

order perturbation theory [65]:

$$\mu^{\mathbf{q}\pi}(\omega) \propto \sum_i \sum_f |\langle \psi_f \,|\, X_{\mathbf{q}\pi} \,|\, \psi_i \rangle|^2 \delta(\hbar\omega - E_f + E_i) \tag{3.14}$$

Here, $X_{\mathbf{q}\pi}$ denotes the electron-photon interaction operator and $\mu^{\mathbf{q}\pi}$ is absorption coefficient for excitation from a specific core level. Therefore, the summation in Eqn. 3.14 includes all the available final states ψ_f with energy E_f and the initial state ψ_i that corresponds to a specific core level with energy E_i. This is the key factor that makes any x-ray absorption technique element selective.

3.5.2 Synchrotron radiation: Source of circularly polarized X-rays

Radiation is produced when charged particles are accelerated. Synchrotron radiation is generated when charged particles like electrons or positrons move at relativistic speeds on a curved trajectory. The relativistic electrons are injected into the ring from a linear accelerator (Linac) and a booster synchrotron as shown in Fig. 3.7. Various magnetic lenses are used to maintain the electron in the desired trajectory. Modern synchrotrons consist of many straight sections with arrays of permanent magnets (undulators or wigglers) to increase the spectral brightness. Bending magnets are used between the straight sections to turn the electron from one straight section to another. As the electrons travel through the insertion devices (bending magnets, undulator and wigglers) synchrotron radiation is emitted as a narrow cone tangential to the path of the particle. A more detailed description can be found in [66].

3.5.3 Undulators and Wigglers

Undulators and wigglers are insertion devices that consist of periodic arrangements of permanent magnets as shown in the Fig. 3.7. This periodicity causes the electron to experience a harmonic oscillation as it moves in the axial direction. In undulators the weak magnetic fields cause a small amplitude of this oscillation resulting in a narrow cone of radiation. In contrast, in wigglers the magnetic field is large, therefore the oscillation amplitude and subsequently the radiated power and the radiating cone is large. The wavelength of radiation from an undulator with a period of magnet λ_u is given by the *undulator equation*:

$$\lambda_n = \frac{\lambda_u}{2\gamma^2 n}\left(1 + \frac{K^2}{2} + \gamma^2\theta^2\right) \tag{3.15}$$

Where n is the harmonic number, γ is the relativistic electron energy, θ the angle of observation, and K the magnet deflection parameter which is given by

$$K = \frac{eB_0\lambda_u}{2\pi mc} \tag{3.16}$$

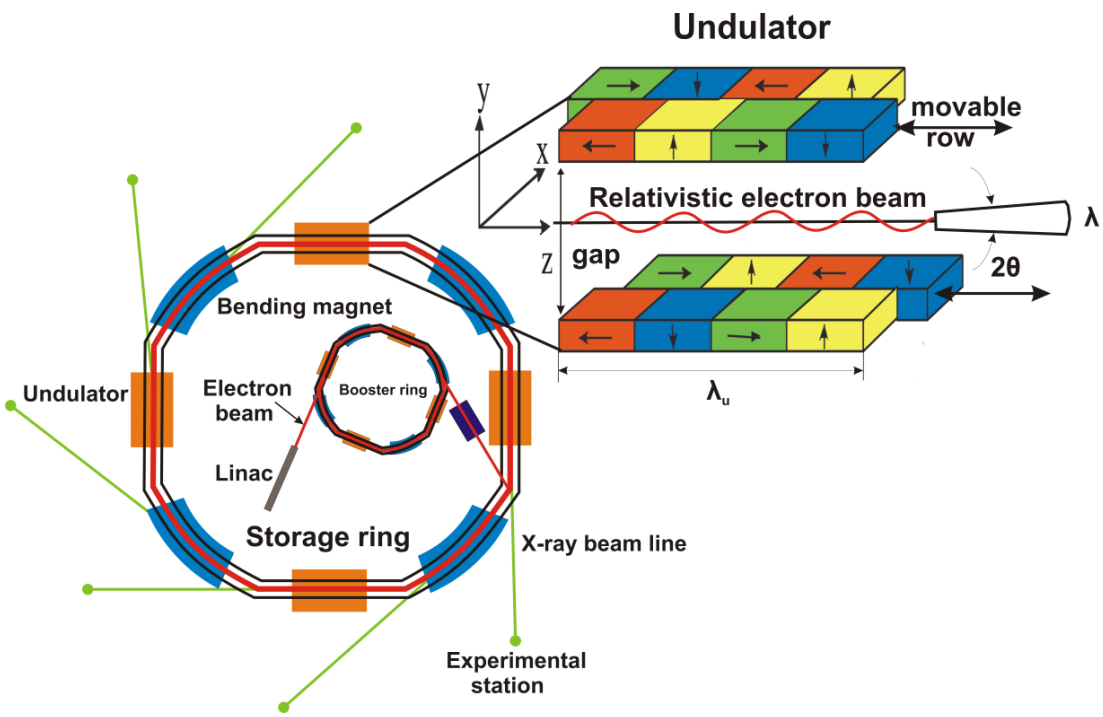

Figure 3.7: *Schematic diagram of a synchrotron storage ring and an undulator. The relativistic electrons are injected into the ring from a linear accelerator (Linac) and a booster synchrotron. Various magnetic lenses are used to maintain the electron in the desired trajectory. Modern synchrotrons consist of many straight sections of permanent magnets arrays (undulators or wigglers) and bending magnets. As the electrons travel through the insertion devices (bending magnets, undulator and wigglers) synchrotron radiation is emitted as a narrow cone tangential to the path of the particle.*

For magnet strengths characterized by $K \leq 1$, undulator type radiation with narrow bandwidth and narrow radiation cone is emitted, for $K \geq 1$ wiggler radiation with higher radiated power is emitted.

The wavelength of radiation can be tuned by K, i.e., by changing the gap of the magnets. In addition, by changing the phase between different arrays of permanent magnet as shown in Fig. 3.7, different modes of polarization, like circular polarization (right and left), linear polarization, and vertical polarization can be achieved.

3.5.4 Basics of x-ray magnetic circular dichroism (XMCD)

According to classical physics, the refractive index of a material, n, is used to describe various optical effects. In general, it depends on the frequency and the polarization of the electromagnetic wave (EM). For a given sample, the fre-

quency dependence is particularly important around specific resonant frequencies and close to such resonances the refractive index is described as a complex dimensionless quantity according to [50][65][66]:

$$n(\omega) = 1 - \delta(\omega) + i\beta(\omega) \tag{3.17}$$

The real part $\delta(\omega)$ is associated with the refraction and the imaginary part $\beta(\omega)$ with absorption of the EM wave in the medium. The polarization dependence of the refractive index is called *birefringence* and the polarization dependence of the absorptive part $\beta(\omega)$ is referred as *dichroism*. In the x-ray energy range, the dependence of the absorption of circularly polarized X-rays on the spin distribution (magnetization) of the sample is called as *x-ray magnetic circular dichroism* (XMCD). This has been observed for the first time at the K-absorption edge of iron by Schütz *et al.* [67]. Later, Chen *et al.* observed the XMCD effect in the soft x-ray energy range ($\approx$ 0.25-2.5 keV) at the $L_{2,3}$ edges of the 3d transition metals and the $M_{4,5}$ edges of rare earth elements [68][69].

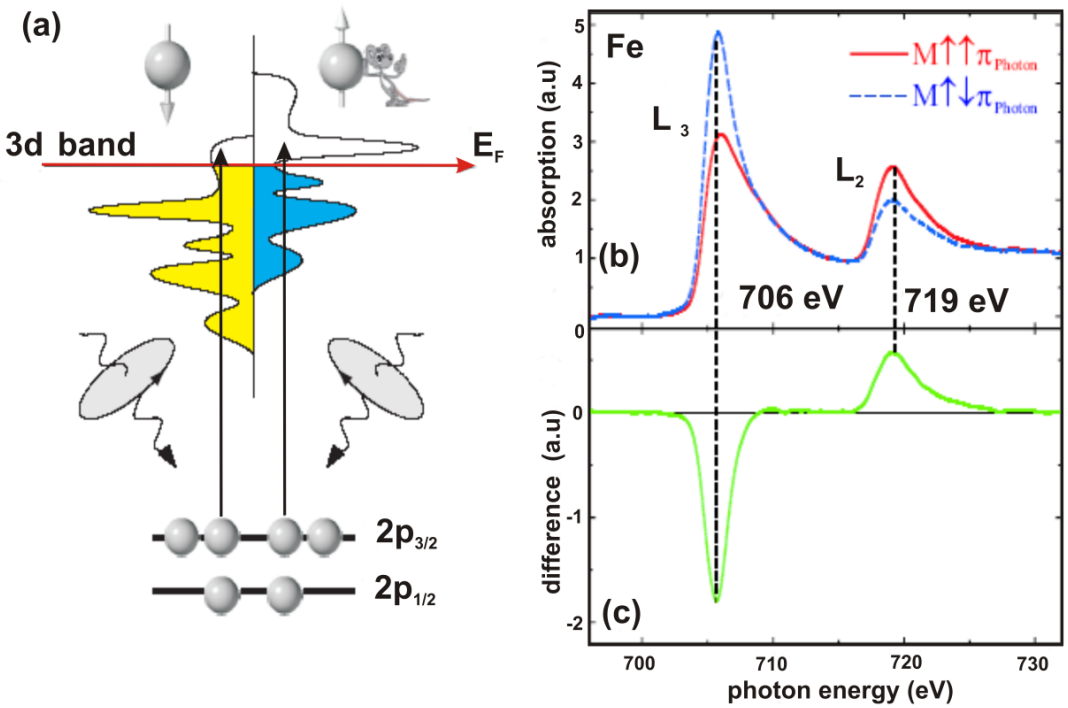

Figure 3.8: *Illustration of the XMCD effect. (a) The 2p core electrons are excited to an unoccupied 3d state at the Fermi level by circularly polarized X-rays [50], (b) Absorption spectrum at the Fe $L_{2,3}$ absorption edges of a iron thin film, taken with right (π^+) and left (π^-) circularly polarized X-rays. The difference between the two spectra gives the XMCD spectra as shown in (c)[47].*

The XMCD effect can be understood as a two step process. In transition metals the magnetic properties arise from the exchange split 3d valence shell, as shown in Fig. 3.8 (a). Due to the spin-orbit coupling the 2p state is split into $2p_{3/2}$ and $2p_{1/2}$ states. In the first step, when circularly polarized X-rays are incident on the sample, conservation of angular momentum requires a transfer of angular momentum of the incident X-rays to the excited photoelectrons. If the photoelectron is excited from a spin-orbit split state, e.g., the $2p_{3/2}$ level (L_3 edge), the angular momentum of the photon can be transferred in part to the spin through the spin-orbit coupling and the excited photoelectrons are spin polarized. The spin polarization is opposite for incident X-rays with positive ($+\hbar$) and negative ($-\hbar$) photon spin. Also, since the $2p_{3/2}$ (L_3) and $2p_{1/2}$ (L_2) level have opposite spin-orbit coupling (l+s and l-s, where l and s are orbital and spin quantum numbers.) the spin polarization will be opposite at the two edges.

In the second step the exchange split valence shell with unequal spin up and spin-down population acts as the detector for the spin of the excited photoelectrons. Therefore, the intensity of the X-ray absorption spectrum changes according to the change in the magnetization direction or the circular polarization of the X-rays. Fig. 3.8 (b) shows the absorption spectrum of circularly polarized X-rays at the Fe $L_{2,3}$ edges of a fully magnetized iron film, for parallel and anti-parallel orientation of the sample magnetization $\mathbf{M}$ with respect to the helicity π of the radiation. The difference between the signals, the XMCD spectrum, is plotted in Fig. 3.8 (c). The different signs for the Fe L_3 and the L_2 edges are due to the opposite spin-orbit coupling of the $2p_{3/2}$ (L_3) and $2p_{1/2}$ (L_2) levels as explained before.

The intensity of the XMCD spectrum depends on the projection of the normalized magnetic moment $\mathbf{m} = \mathbf{M}/|\mathbf{M}|$ onto the photon propagation direction, $\mathbf{e}_z$, and on the degree of circular polarization, P_{cir}:

$$I_{XMCD} \propto P_{cir}\mathbf{m} \cdot \mathbf{e}_z \tag{3.18}$$

3.5.5 Scanning transmission x-ray microscopy (STXM)

In scanning transmission x-ray microscopy, a monochromatic x-ray beam is focused to the smallest possible spot size and the x-ray intensity transmitted through the sample is monitored as a function of the beam position on the sample. A schematic digram of a STXM is shown in Fig. 3.9. In this thesis, the scanning transmission x-ray microscope located at beamline 11.0.2 at the Advanced Light Source (ALS), Berkeley, CA has been used. The annotated computer aided design (CAD) diagram of the system is shown in appendix A.1. Here the X-rays from a elliptical undulator are focused by a zone-plate lens onto the sample [70]. The sample is raster scanned by a piezo stage with a precession of a few nanometers. For course translation of the sample, another x, y, z stage controlled by stepper motors is used. The relative position of the sample stage and the zone plate lens

is controlled by a laser interferometer. In order to increase the signal to noise ratio by suppressing unwanted diffraction, the zone plate is fabricated with a beam stop. In addition, a small pinhole, the order selection aperture (OSA) is placed between the sample and the zone plate to allow only the first diffraction order to pass. The spatial resolution depends on the numerical aperture (NA) of the zone plate. It is determined by the size of the outermost zone width Δr at a fixed wavelength of the incident X-rays [NA = $\lambda/(2\Delta r)$]. Today, the best resolution is about 15 nm and a resolution below 10 nm is expected in the future [71]. Since the focal length of the zone plate lens changes with the photon energy, the STXM microscope has to be refocused synchronously if the photon energy changes. The transmitted photon intensity is detected by a photomultiplier or by an avalanche photo diode (APD). The spectral energy resolution E/ΔE is about 2500-7500. The maximum raster scan range is 20 mm$\times$4 mm, while the minimum step size is 2.5 nm. Images with up to 3000$\times$2000 pixels can be acquired at any spatial size within these limits.

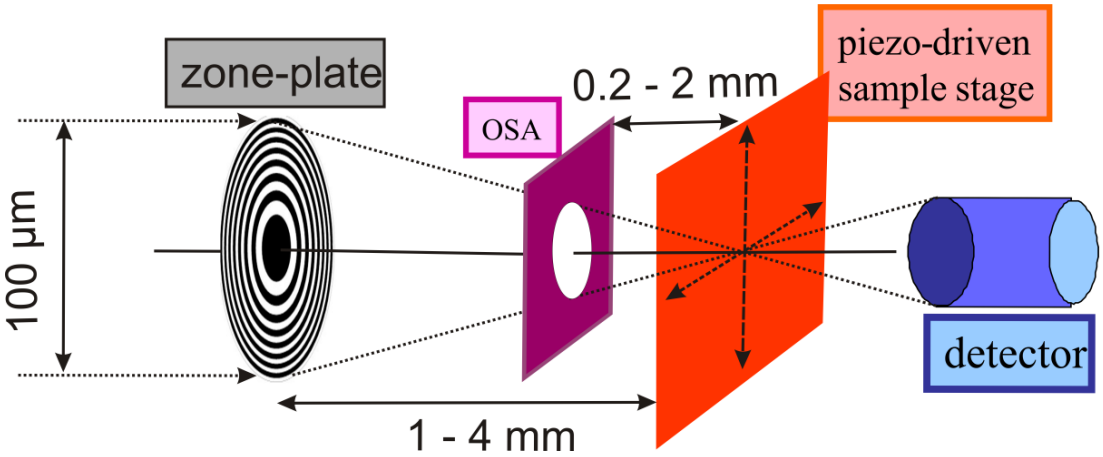

Figure 3.9: *A schematic diagram of a scanning transmission x-ray microscope in which the synchrotron radiation is focused onto the sample by a zone-plate. An order selection aperture (OSA) allows only the first order diffraction to pass. While scanning the sample in x, y direction, the transmitted intensity is detected by a photo multiplier or a avalanche photo diode (APD).*

XMCD as a magnetic contrast

When a thin, transparent magnetic sample is illuminated with circularly polarized X-rays whose energy is tuned to the element-specific absorption edge, the transmitted intensity probes the magnetization distribution, i.e., the domain structure of the sample, according to Eqn. 3.18. The images of a magnetic sample at left and right circularly polarized X-rays are shown schematically in Fig. 3.10. Due

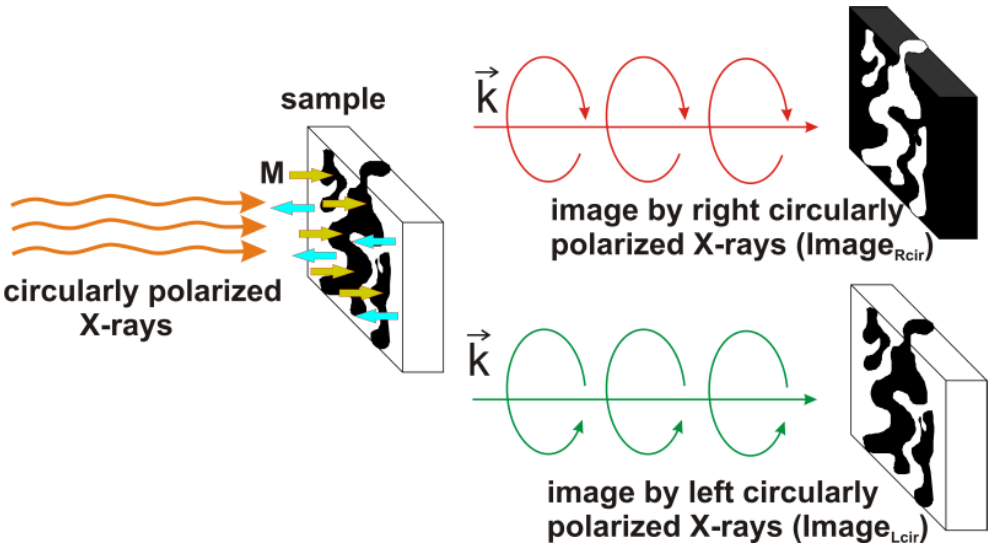

Figure 3.10: *Schematic diagram of XMCD magnetic contrast. A thin magnetic sample with domains is illuminated with circularly polarized X-rays. Images taken with right and left circularly polarized x-rays exhibit opposite magnetic contrast due to the spin dependent absorption.*

to the spin-dependent absorption the polarity of the magnetic contrast changes upon changing the polarization of the X-rays. In order to increase the signal to noise ratio and to eliminate non magnetic contributions, the difference between images taken with the right ($Image_{R_{cir}}$) and left ($Image_{L_{cir}}$) circular polarization is divided by the non magnetic contribution, i.e., the sum of both images. In general, the XMCD image ($Image_{XMCD}$) can be expressed as

$$Image_{XMCD} = \frac{Image_{R_{cir}} - Image_{L_{cir}}}{Image_{R_{cir}} + Image_{L_{cir}}} \tag{3.19}$$

XMCD images of a Fe/Gd multilayers deposited on a flat Si_3N_4 membrane and on nanospheres are shown in Fig. 3.11 (a) and (b), respectively.

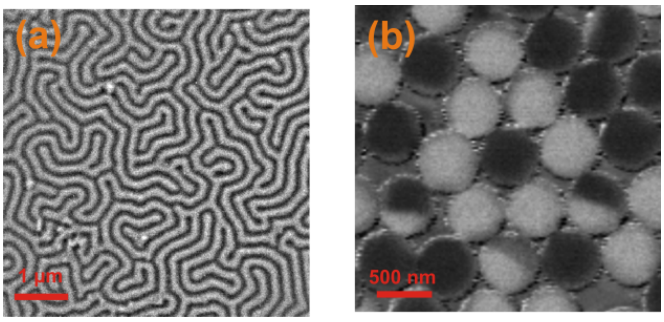

Figure 3.11: *XMCD images of Fe/Gd multilayers deposited on (a) flat Si_3N_4 membrane [47], and (b) on nanospheres with a diameter of 800 nm.*

Quantitative magnetic imaging with STXM

Scanning transmission x-ray microscopy is an versatile tool to study magnetic nanostructures using XMCD contrast mechanism with high spatial and temporal resolution. The magnetization reversal behavior of nanostructures can be studied by applying a static perpendicular or in-plane magnetic field. Such studies are possible because STXM is a photon-in/photon-out method. The magnetization dynamics of nanostructures can also be studied at a picosecond temporal resolution [72][73]. In this thesis the static magnetization reversal mechanism is addressed on a nanometer scale.

There are two different methods to study the magnetization reversal at STXM. The first method is called "*magnetic field imaging*" as explained below.

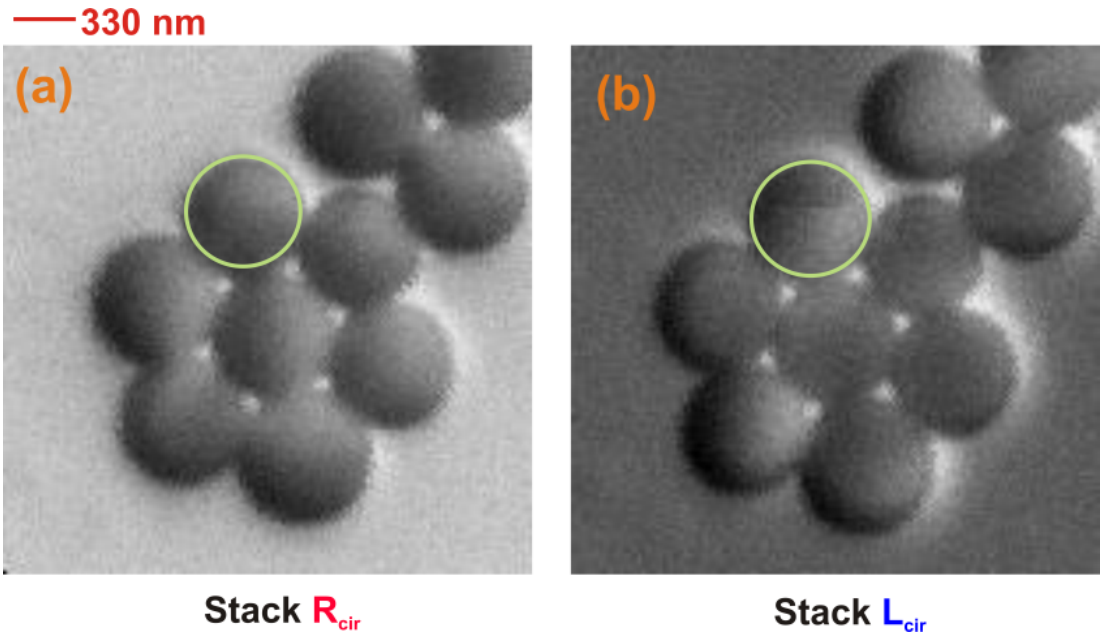

Figure 3.12: *A stack of aligned images, taken with right circularly polarized X-rays (a) and left circularly polarized X-rays (b). The intensity of each image in the stack is integrated within the circle marked on a nanosphere with a diameter of 330 nm.*

Fig. 3.12 shows silica nanospheres with a diameter of 330 nm coated with Fe/Gd multilayers. The energy of the x-ray photons are set to the L_3 absorption edge of Fe. The sample is imaged with right and left circularly polarized light at different external fields. Images taken at right and left circularly polarized X-rays are aligned and converted to two different stacks, designated as *stack* R_{cir} and *stack* L_{cir} respectively [see Fig. 3.12 (a) and (b)]. In order to study the magnetization reversal of an individual nanosphere, the intensity within the circle shown in Fig. 3.12 is integrated on each image in the stack. The integrated

intensity from the image taken at right and left polarization are designated as I^+ and I^-, respectively. The XMCD intensity is proportional to the magnetization of sample and calculated by

$$I_{XMCD} = \frac{ln(I^+) - ln(I^-)}{ln(I^+) + ln(I^-)} \propto \mathbf{m} \cdot e_z \tag{3.20}$$

According to Beers law [see Eqn. 3.13], $ln(I^{\pm})$ in Eqn. 3.20 is proportional to the absorption coefficient, $\mu^{\pm}$ of the sample. The local hysteresis loop of an individual sphere is deduced by plotting the calculated XMCD intensity as a function of the corresponding field value of the image.

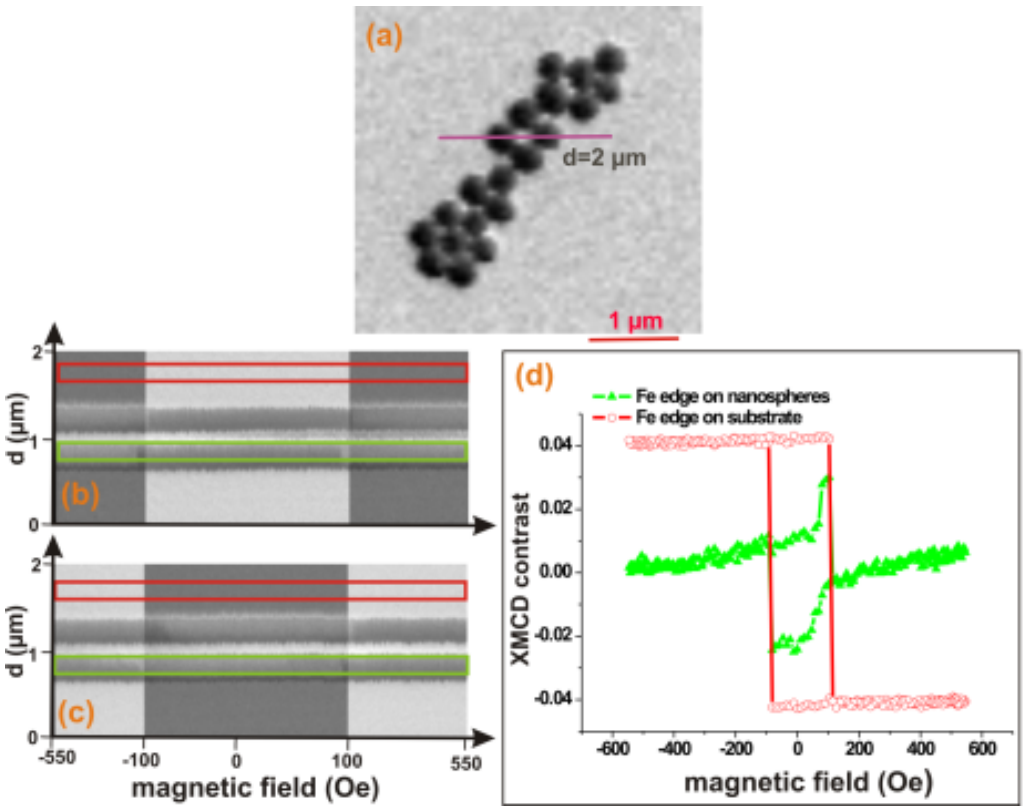

Figure 3.13: *(a) Overview image of silica nanospheres of 330 nm in diameter covered with Fe/Gd multilayers. The 2 µm line marked in (a) is scanned at different magnetic fields with right (b) and left (c) circularly polarized X-rays. The x-axis corresponds to the field values and the y-axis denotes the length of the scanned line. Local hysteresis loops deduced by averaging the intensity in rectangle on a flat region (red) and on spheres (green) are shown in (d).*

The next method is called "*magnetic field linescan imaging*". Here, a line marked on an image, as shown in Fig. 3.13 (a) is scanned at different external fields. Fig. 3.13 (b) and (c) shows such magnetic field linescans taken with right

and left circularly polarized X-rays. The x-axis corresponds to the magnetic field and the y-axis corresponds to the length (μm) of the scanning line. The line marked in Fig. 3.13 (a), covers a flat region of the substrate and two individual spheres. By averaging the intensity on a flat region as indicated by the red rectangle [1] in Fig. 3.13 (b) and (c), a local hysteresis loop is deduced. Likewise, averaging the intensity on an individual sphere, (green rectangle) the local magnetization reversal on a sphere is deduced. Fig. 3.13 (d) shows both local hysteresis loops.

All the images used in this work are analysed by different image processing softwares, which includes ImageJ [74], IDL, PEEM analyser, PEEM vission [75], and Axis [76].

3.5.6 X-ray photoemission electron microscopy (X-PEEM)

X-ray photoemission electron microscopy (X-PEEM) is a X-rays-in/electron-out imaging method. The PEEM-II located at beam-line 7.3.1.1 of the Advanced Light Source in Bekeley, CA has been used [77][78]. The bending magnet beam line provides X-rays with an energy between 250 and 1300 eV. A movable aperture is used to change the photon polarization from linear to left and right circular. A x-ray beam focused to a spot size of ≈ 30 μm is incident on the sample at an angle of 30° to the sample plane. The energy resolution of the beamline, optimized for high flux, is between $E/\Delta E \approx$ 1000-1800. A schematic diagram of X-PEEM is shown in Fig. 3.14. The CAD diagram of the PEEM-II microscope at the ALS is shown in appendix A.2.

The microscope spatially resolves and images the secondary electrons emitted from a sample upon illumination with X-rays. Four electrostatic lenses are used for focusing and projection of the electrons. The electrons are accelerated by a strong electric field ($\approx$20 kV) between sample and the objective lens of the microscope. After a magnification by a factor of 1000-2000, the electrons hit a phosphor screen which is detected by a CCD (charge coupled device) camera. An aperture in the back focal plane of the second lens (transfer lens) is used to reduce the spherical and chromatic aberrations of the electron optics. The typical spatial resolution for magnetic imaging is about 50 to 100 nm. In addition, deflector and stigmator elements located in the back focal plane of the objective lens and the first projection lens are used to correct for small mechanical misalignments of the microscope.

The contrast in the images taken at PEEM is a superposition of chemical, magnetic and topographical contribution. The magnetic contrast scales with the XMCD effect according to Eqn. 3.19. Therefore, images are taken with left and right circularly polarized X-rays whose energy is tuned to the absorption edges

[1] Each pixel along the length of the rectangle corresponds to the magnetic field. The intensity is averaged over every pixel along the width of the rectangle.

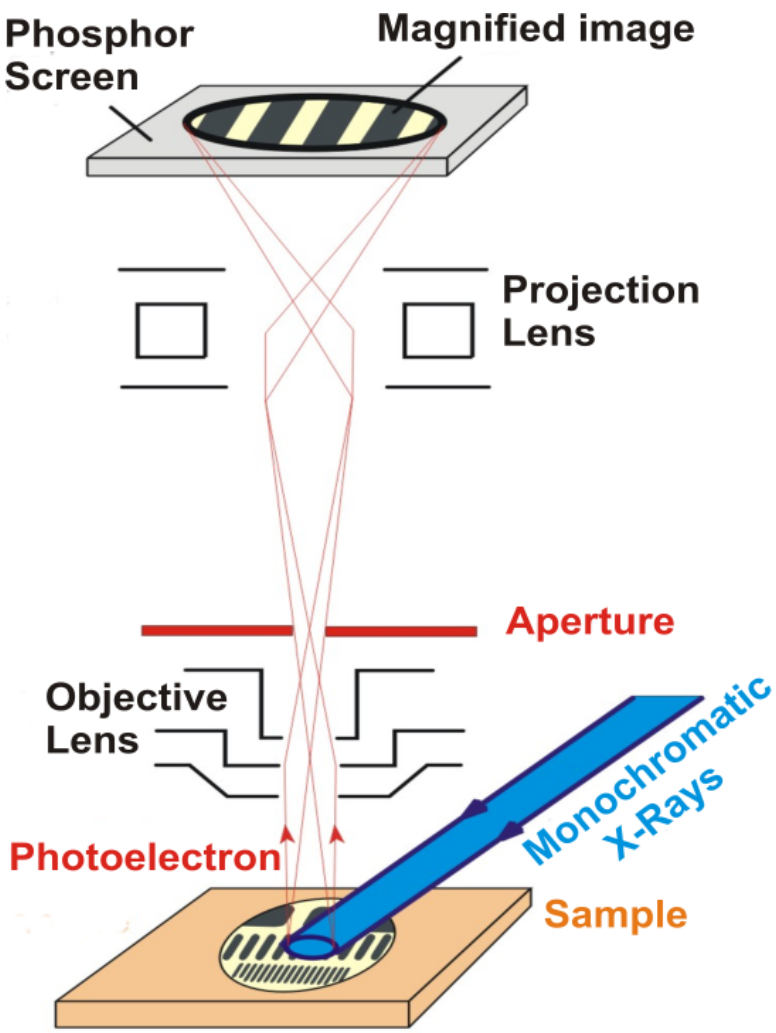

Figure 3.14: *Schematic diagram of a X-ray photoemission electron microscope. Secondary electrons are emitted from a sample upon illumination with X-rays. These electrons are focused and projected onto the phosphor screen by different electrostatic lenses. [50].*

of the element under study. Since the intensities of images taken with left and right circularly polarized light are close to each other, it is common to divide both images to get a quantitative magnetic image. If R and L designate the images at right and left circular polarization, one can assume that $R = L+\delta$ and simple mathematical transformation shows that: $(R\text{-}L)/(R+L) \approx (R\text{-}L)/(2L+\delta) \approx 0.5$ (R/L)–0.5. Therefore, division of images gives approximately the same result of magnetic contrast with respect to the XMCD contrast stated in Eqn. 3.19 [78].

Chapter 4

Fe/Gd multilayers on flat substrates

The magnetic properties of compositionally modulated films (CMF) have attracted lot of research interest in recent years. The study of properties like perpendicular magnetic anisotropy (PMA) and spin-reorientation transitions (SRT), constitute fertile areas of fundamental research. In an application perspectives, these properties are promising for perpendicular magnetic recording, magneto optical recording and magnetic sensors. Different types of CMF have been studied both theoretically and experimentally. Most prominent examples are the multilayers of rare earths (RE)/transition metals (TM) (RE = Gd, Tb, Dy, Nd and TM =Co, Fe, Ni)[79–81], Co/Pd [82–85], Co/Pt [86–88], Fe/Cr[89, 90], Fe/Si[91], Fe/Pt[92] etc. In this chapter the properties of Fe/Gd systems are discussed in detail.

4.1 Properties

Pure Fe and Gd metal

The magnetic moments in Fe and other ferromagnetic transition metals are entirely due to $3d$ electrons. The spin moment plays a dominant role and the contribution of orbital moment is about 5 % for Fe, 10 % for Co and 8 % for Ni. In rare earth metals the well localized and atomic like $4f$ shell contains more number of unpaired electrons and therefore the magnetic moment is dominated by $4f$ electrons. The spin and orbital configuration is given by Hund's rules. According to Hund's rule when the $4f$ shell is less than half-filled the spin and orbital angular momentum couple antiparallel to each other and the total angular momentum is given by J = $|L - S|$. On the other hand for more than half filled shell, the spin and orbital angular momenta prefers parallel alignment and the total angular momentum is given by J = $|L + S|$. Gd metal has the special property of half filled $4f$ shell, therfore the $4f$ orbital moment is zero.

The direct exchange between the Fe atoms leads to a ferromagnetic coupling whereas in Gd atoms the indirect or RKKY interaction between 4f atomic moments mediated by outer s and p electrons gives rise to a ferromagnetic ordering. The fact that the magnetic ordering temperature is below room temperature indicates a rather weak exchange coupling, J, i.e., $J_{Gd-Gd} << J_{Fe-Fe}$. In addition, there is a direct overlap of the $4f$ and the $5d$ electrons and yield a strong direct exchange and polarizes the $5d$ electrons parallel to the $4f$ moments. Therefore the total moment of Gd in the pure metallic state consists of a 7.0 μ_B from $4f$ contribution and 0.6 μ_B from $5d$ contribution [93].

	atomic config	**at. radius**	**lattice parameter (nm)**	μ/**Atom**	T_c
Fe	[Ar]3d^6 4s^2	0.128 nm	bcc, a=0.286	2.2 μ_B	1043 K
Gd	[Ar]4f^7 5d^1 6s^2	0.180 nm	hcp, a=0.362, c=0.575	7.55 μ_B	289 K

Table 4.1: Properties of Fe and Gd.

Fe-Gd system

In a Fe-Gd system the exchange between the Fe $3d$ electrons and the Gd $5d$ electrons induce a negative exchange integral producing an antiparallel alignment of the magnetic moment. The large misfit between the basic properties of Fe and Gd atoms, as shown in Tab. 4.1, leads to many interesting properties in these systems.

Cameley and co workers reported a theoretical phase diagram for crystalline FeGd alloys as a function of temperature and external magnetic fields [94, 95]. The competition between the exchange and the Zeeman energy terms result in different phases. There are aligned phases in which either the Fe spins or the Gd spins align with the external field and twisted phases where the spins are at an angle to the external field. The existence of such phases is also observed experimentally [96, 97].

Since the Fe-Gd system exhibit ferrimagnetic behavior the temperature dependence of the net magnetization is different from the temperature dependence of sub-network magnetization of Fe and Gd as shown in Fig. 4.1. At the compensation temperature, T_{com}, the two subnetwork magnetization are equal and opposite. Consequently the net magnetization of the system becomes zero (M_s = 0). For temperature below T_{com} the sub-network magnetization of Gd dominates the net magnetization whereas for temperature above T_{com} the sub-network magnetization of Fe dominates [99, 100].

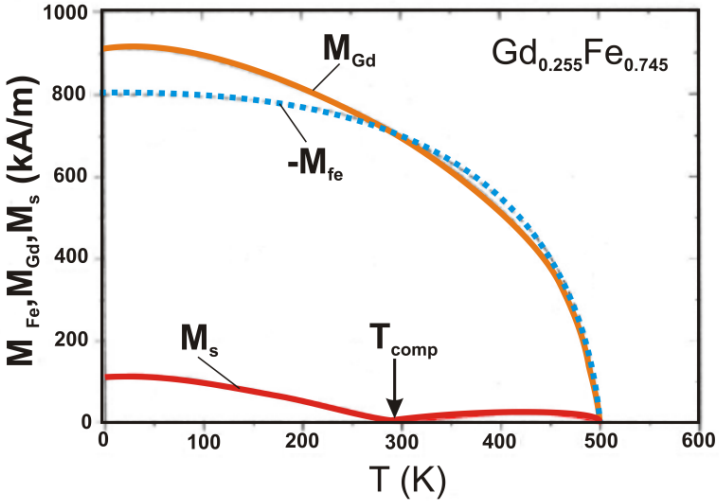

Figure 4.1: *Temperature dependence of the saturation magnetization and the sub-lattice magnetization for an amorphous Gd-Fe alloy exhibiting a compensation temperature [98].*

Perpendicular magnetic anisotropy

Fe-Gd system manifests a perpendicular magnetic anisotropy (PMA) at room temperature. The origin of this anisotropy has been attributed to many different mechanism, e.g, pair ordering [101], columnar microstructures [102], and exchange anisotropy [103]. Hansen *et al.* demonstrated the strong influence of alloy composition on sign and magnitude of K_u. These results have been explained by pair ordering and dipolar interaction model [104]. On the other hand in multilayer system the situation is much more complex. Nawate *et al.* found a perpendicular magnetization in a sputter deposited multilayer system and ascribed it to the contribution of Fe-Gd alloys formed at the interface [105].

The preparation conditions and structural properties are also reported to play a vital role in the PMA. For example, in Fe/Gd multilayers the Fe layer changes from a crystalline bcc state to a amorphous state below a critical thickness, t_{Fe} (1.7 nm - 2 nm) [106, 107]. The exact origin of the PMA, however remains unclear. In general, perpendicular magnetic anisotropy (PMA) may include additive or competing contributions from several of the mechanism as postulated as follows [108]:

- The anisotropic distribution of atoms which arises from different crystal structures and the stress induced in the samples.
- The interaction between the constituent atoms, including the magnetic dipolar interaction and the spin-orbit interaction that leads to the single ion anisotropy.

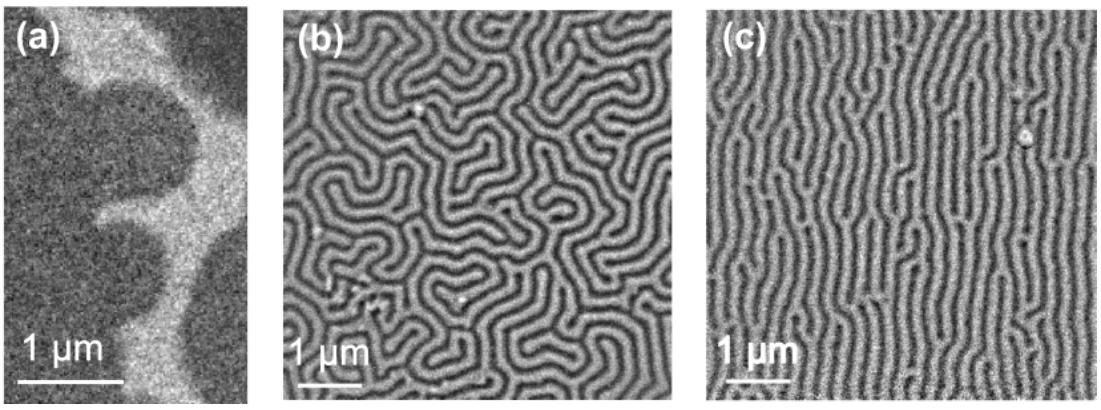

Figure 4.2: *(a) Magnetic transmission x-ray microscopy images of Fe/Gd system prepared on a polyimide substrate show an irregular domain structure. Similar system on Si_3N_4 membrane shows a maze like, (b) or parallel stripe domains (c) at remanence after saturating the sample with an out-of-plane field and in-plane field, respectively [47].*

Eimüller *et al.* demonstrated the strong influence of the substrate and magnetic history on the domain configuration of the Fe/Gd multilayers [47]. Deposited on a polyimide substrate Fe/Gd system shows an irregular domain structure with pinning centers, see Fig. 4.2 (a). In contrast, a maze or parallel stripe domains are seen on Si_3N_4 membrane. A maze pattern is obtained at remanent state, if the sample is saturated along out-of-plane direction (Fig. 4.2 (b)), whereas parallel stripe domains are seen if the sample is saturated along in-plane direction (Fig. 4.2 (c)).

Spin reorientation transition

Another interesting property of Fe/Gd systems is the spin reorientation transition (SRT). A spin reorientation transition is a phenomena in which the magnetization direction of a magnetic thin film changes from one plane to the other due to an increase of its thickness, or its temperature. It is caused by the presence of two or more competing anisotropies preferring different easy directions of the magnetization. The two different types of SRTs are "*the normal SRT*" and "*the reverse SRT*" [109]. In the normal SRT the magnetization direction changes from a perpendicular to an in-plane direction with increasing temperature, T, or film thickness, t, as shown schematically in Fig. 4.3 (a). Prominent examples for such a SRT are Fe/Ag [110–112], Fe/Cu [113–115], Co/Au [116–118] thin films and multilayer systems. In the reverse SRT, the magnetization direction changes from in-plane to perpendicular direction upon increasing the temperature, T, or the thickness, t, of the film (see Fig. 4.3 (b)). The Fe/Gd[119], Fe/Si[91], Co/Pd [120, 121] and Co/Pt [122, 123] multilayer systems are a few examples that show

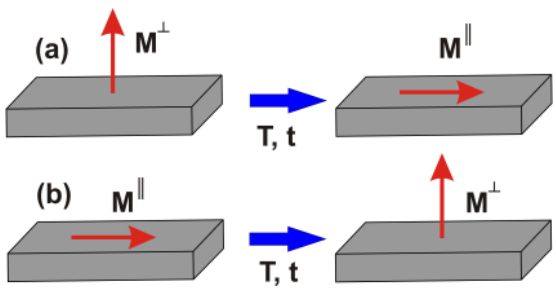

Figure 4.3: *Schematic diagram of the spin reorientation transition in magnetic thin films, (a) the normal SRT in which the magnetization direction changes from a perpendicular to in-plane orientation as a function of temperature T or film thickness t, and (b) the reverse SRT in which the magnetization direction changes from in-plane to perpendicular direction.*

a reverse SRT.

Stavrou *et al.* have done extensive studies of the anisotropy and SRT in amorphous Fe/Gd multilayers as function of the periodicity ($\beta = t_{Fe}+t_{Gd} = 1.2$ nm - 5.3 nm), the temperature (T), and the composition (t_{Fe}/t_{Gd}) [124–127]. However, less is known about the Fe/Gd multilayer with sub-layer thickness of less than 1 nm and with a ratio of 1 ($t_{Fe} = t_{Gd}$). Hence the magnetic and structural properties of such thin Fe/Gd multilayers are addressed in this work. In addition, the domain configuration during the SRT and the structural changes are also studied in detail. The structural properties are studied by transmission electron microscopy (TEM) and x-ray reflectivity measurements.

4.2 Sample preparation

Fe/Gd multilayers have been prepared by RF sputtering. A schematic diagram of the sputtering chamber is shown in Fig. 4.4. It consists of an RF source, a rotatable target holder and a fixed substrate holder in a vacuum atmosphere. Ar ions produced by the RF source are accelerated at high voltage towards the required target material. Due to the bombardment of heavy Ar ions, the atoms from the target are ejected and deposited on the substrate. Four different targets can be mounted on the rotatable holder and selected by a stepper motor. The thickness of the deposited film is controlled by a quartz crystal. Table 4.2 lists the sputtering parameters used to prepare the Fe/Gd multilayers.

Base pressure	**Sputtering pressure**	**Sputter rate**	**RF power**	**RF frequency**
$\approx 2\times10^{-8}$mbar	$\approx 1\times10^{-4}$mbar	$\approx$ 1 Angström /s	120 W	13.56 MHz

Table 4.2: Sputtering parameters used in the preparation of the Fe/Gd multilayers.

All samples possess the same thickness of Fe and Gd layer ($t_{Fe} = t_{Gd}$). Silicon

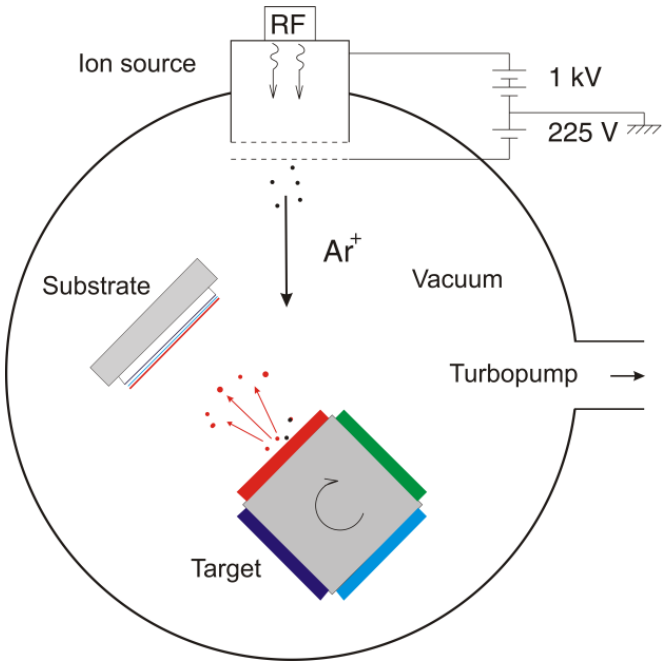

Figure 4.4: *A schematic diagram of a RF-sputtering system. The high energy Ar ions from the ion source hit the target and eject atoms which are deposited onto the substrate.*

is used as a substrate and a 0.8 nm thick film of Al is used as a capping layer to protect the sample from oxidation. In addition, 0.8 nm of Al is sputtered prior to the deposition of the Fe/Gd multilayers to reduce the inter-diffusion of the Gd and Si.

4.3 Thickness driven spin reorientation transition (SRT)

A series of samples are prepared by increasing the periodicity, β=t_{Fe}+t_{Gd}, to study the thickness dependent SRT and the PMA. MOKE and SQUID are used to study the magnetic properties. The structural properties are studied by XRR and TEM analysis. Table 4.3 shows a list of samples and its composition for which the magnetic properties are studied as a function of periodicity (β). Hysteresis loops, presented in Fig. 4.5 (a), are measured using MOKE in a polar geometry. For β = 0.72 nm - 1 nm rectangular shape loops are seen. This indicates that the magnetic easy axis is perpendicular to the sample plane. At β = 1.04 nm a slight deviation from a rectangular shape is noticed and for 1.08 nm a hard axis loop is observed. Therefore, on increasing the sub-layer thickness a continuous transformation from a perpendicular to an in-plane magnetized state is seen.

name	β=t_{Fe}+t_{Gd}	**multilayer structure**
Splib 486	0.72 nm	75x[Gd(0.36 nm)/Fe(0.36 nm)]
Splib 510	0.84 nm	75x[Gd(0.42 nm)/Fe(0.42 nm)]
Splib 511	0.88 nm	75x[Gd(0.44 nm)/Fe(0.44 nm)]
Splib 516	0.96 nm	75x[Gd(0.48 nm)/Fe(0.48 nm)]
Splib 517	1.00 nm	75x[Gd(0.50 nm)/Fe(0.50 nm)]
Splib 524	1.04 nm	75x[Gd(0.52 nm)/Fe(0.52 nm)]
Splib 525	1.08 nm	75x[Gd(0.54 nm)/Fe(0.54 nm)]
Splib 526	1.12 nm	75x[Gd(0.56 nm)/Fe(0.56 nm)]
Splib 527	1.16 nm	75x[Gd(0.58 nm)/Fe(0.58 nm)]
Splib 528	1.20 nm	75x[Gd(0.60 nm)/Fe(0.60 nm)]

Table 4.3: List of samples for which the thickness dependent SRT has been studied.

To get more insight into the magnetic anisotropy of these samples both in-plane and out-of-plane hysteresis loops are measured by SQUID. The effective anisotropy is evaluated by subtracting the integrated area under the in-plane hysteresis loop from the area under the corresponding perpendicular hysteresis loop. For some measurements the saturation magnetization of the in-plane and out-of-plane measurements are found to be slightly deviated from each other. In such cases the saturation magnetization is normalized to an averaged value. The calculated effective anisotropy K_{eff} is plotted as a function of β in Fig. 4.5 (b). In agreement with the MOKE measurement a change in the sign of K_{eff} is noticed at the onset of the spin reorientation transition from perpendicular to the in-plane direction.

This can be understood by the different contributions of the anisotropy energy in multilayered magnetic thin films. The effective anisotropy, see Eqn. 2.4, can be separated into two contributions, namely the surface or the interface anisotropy term K_s and the volume term K_v, see Eqn. 4.1. K_S is proportional to the area of the film and due to the broken symmetries at the surface and the interfaces it prefer the magnetization to be oriented perpendicular to the film plane. Whereas the volume term that contains the anisotropy of the bulk system and the shape anisotropy, prefers an in-plane magnetization.

$$K_{eff} = K_V + 2K_S/\beta \tag{4.1}$$

As the thickness β of the film increases, the volume term (K_V) dominates the surface/interface anisotropy (K_S) and results in the in-plane magnetization of the sample.

Next to the contribution of shape anisotropy, the intermixing at the interface may also contribute to the PMA of the sample. To substantiate this assumption, transmission electron microscopy (TEM) and low angle x-ray reflectivity

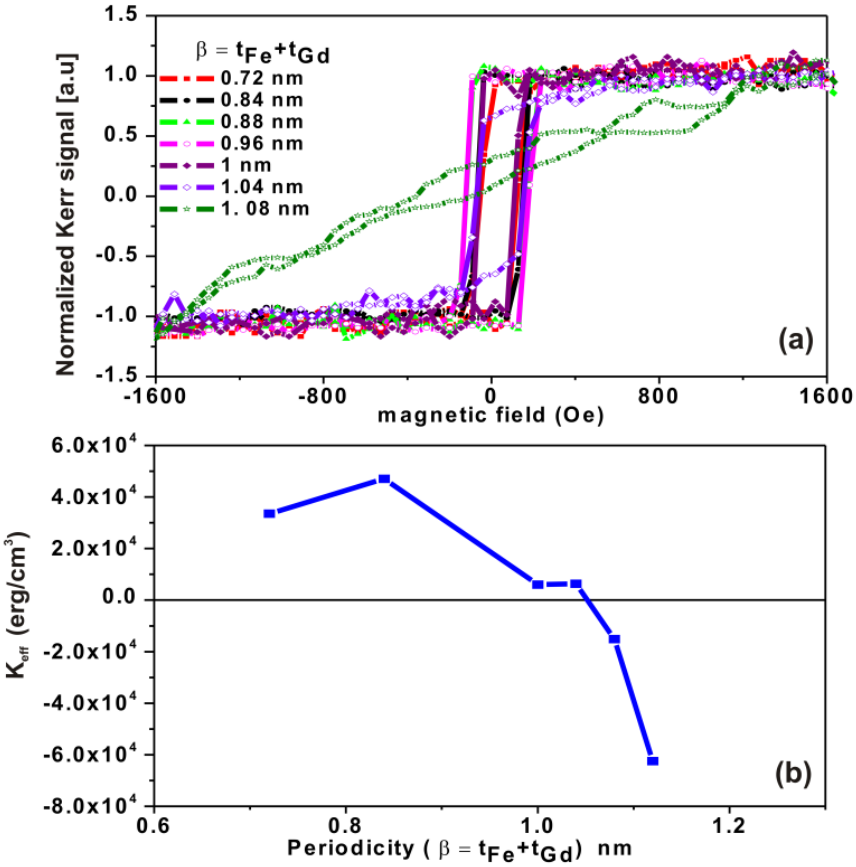

Figure 4.5: *(a) Hysteresis loops measured by a polar-MOKE on increasing the periodicity β, (b) the effective anisotorpy K_{eff} deduced from the SQUID measurements is plotted as a function of the periodicity β.*

(XRR) studies have been performed. The main aim is to compare the structural changes in an in-plane and an out-of-plane magnetized sample. To ease TEM measurements and to ensure uniform treatment of both samples, a sandwich of an in-plane and a perpendicular sample separated by an Al film is prepared. The film composition of splib 526 ([75x(Gd(0.56 nm)/Fe(0.56 nm))]) that shows a hard axis hysteresis loop is sputter deposited on a sample that shows an easy axis loop, splib 517 ([75×(Gd(0.50 nm)/Fe(0.50 nm))]). The TEM image shown in Fig. 4.6 (a) reveals the sandwich structure separated by Al layer. Hysteresis loops measured on both samples are shown in the inset of Fig. 4.6 (a). The easy axis and the hard axis loops confirm that the two samples exhibit an out-of-plane and an in-plane magnetization direction. In Fig. 4.6 (a) a layered structure is seen in both the sample. The Bragg peak (bilayer peak) seen in the low angle

x-ray reflectivity curves also confirms the stacking of Fe and Gd layers, Fig. 4.6 (b). It should be noted that the thickness of the bilayer calculated from the Bragg peak is about 0.3 nm greater than the thickness given by the quartz crystal.

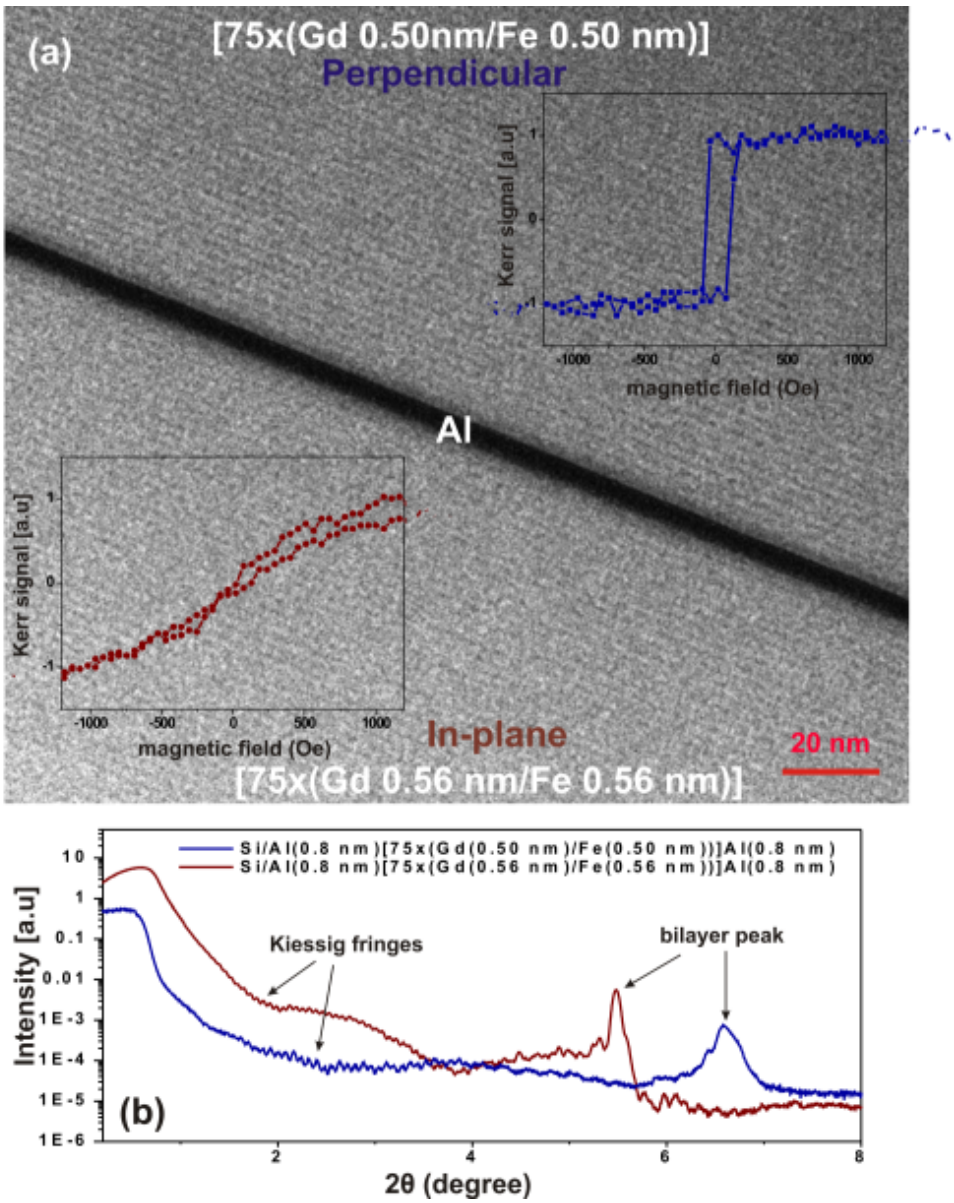

Figure 4.6: *(a) TEM image of the sandwich of in-plane and perpendicular sample separated by an Al layer and their corresponding hysteresis loop measured by polar MOKE, (b) XRR measurement of a reference samples.*

The layered structure in the sample that exhibits a uniaxial perpendicular mag-

netic anisotropy is more prominent than in the sample with in-plane magnetic anisotropy. The in-plane part of the TEM image shows more broken interfaces which in turn lead to the intermixing of the adjacent layers, see Fig. 4.6. Therefore, in-plane magnetization is caused by the inhomogeneous interfaces, whereas almost homogeneous interfaces lead to PMA. These results can be quantitatively understood by the dipolar pair ordering model as explained in the following:

According to this model the intrinsic anisotropy energy K_u is expressed by the subnetwork magnetization of Fe (M_{Fe}) and Gd (M_{Gd}) atoms and the exchange coupling coefficients between the like (G_{Gd-Gd} and G_{Fe-Fe}) and unlike (G_{Gd-Fe}) atoms as shown in Eqn. 4.2 [128, 129].

$$K_u = (G_{Gd-Gd}M_{Gd}^2 - 2G_{Gd-Fe}M_{Fe}M_{Gd} + G_{Fe-Fe}M_{Fe}^2) \tag{4.2}$$

Here K_u is the uniaxial anisotropy energy defined so that $K_u > 0$ for a perpendicular easy direction and $K_u < 0$ for an in-plane easy direction. Due to

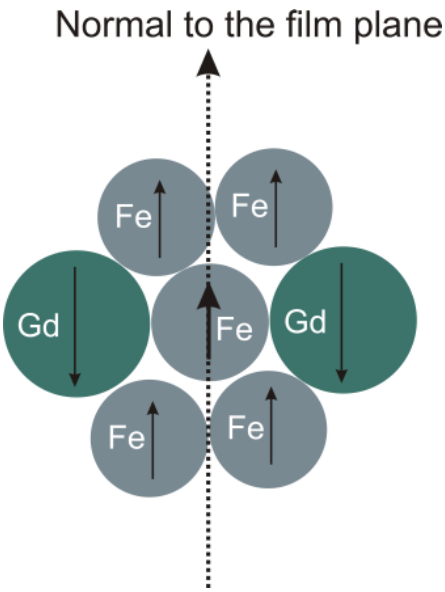

Figure 4.7: *Illustration of atomic scale magnetic moment of Fe and Gd atoms aligned with dipolar field of center Fe atom [128, 129].*

the dipolar interactions, atomic magnetic moments of Fe and Gd atoms align perpendicular to the film plane as shown in Fig. 4.7. Therefore, in an almost homogeneous interface as seen in the perpendicular part of the TEM image (Fig. 4.6) such atomic distribution are believed to be the origin of PMA. On the other hand, upon increasing film thickness the interface roughness increases and lead to an inhomogeneous intermixing at the interface. Consequently the dipolar interaction between the atomic moments may deviate from the situation shown in Fig. 4.7 and lead to an in-plane magnetization. However, the anisotropic intermixing at the Fe/Gd interface may also lead to more complicated cluster like structure with different magnetic phases as proposed by Stavrou *et al.* In such cases the anisotropy energy K_u given in Eqn. 4.2 has to be modified. The coupling coefficients G_{Gd}, G_{Gd-Fe} and G_{Fe} which are a function of the distance

between the Gd-Gd, Fe-Gd, and Fe-Fe atom pairs, respectively, are very sensitive to the preparation conditions. Therefore, undetectable changes during the sample preparation, such as small changes in pressure, temperature, or the bias voltage are also believed to play a vital role in the PMA of the system. Due to this reason some samples, prepared under identical conditions and thicknesses show either an in-plane or a perpendicular magnetic state.

Dependence of magnetic properties on number of bilayers

Another series of samples have been prepared to study the magnetic properties of the sample as a function of the number of bilayers. The thickness of the sub layer and its ratio (t_{Fe}/t_{Gd}) are 0.36 nm and 1, respectively . Table 4.4 shows the list of the samples, their composition, magnetic moment, and the coercive fields (in-plane and out-of-plane). Easy axis and hard axis hysteresis loops measured by SQUID are shown in Figs. 4.8 (a)–(e). K_{eff} of each sample is calculated as described in previous section and plotted as the function of number of bilayers in Fig. 4.8 (f). On increasing the number of bilayers from 20 to 50, K_{eff} shows almost a decreasing behavior but for 75 bilayer it again reaches the maximum value. The in-plane and out-of-plane coercive field shown in table 4.4 also show strong deviation with respect to the number of bilayers. In addition, the atomic magnetic moment calculated assuming a composition of $Fe_{0.5}Gd_{0.5}$ shows an oscillating behavior and reflects the changes in the saturation magnetization and the H_c. These changes in the magnetic properties of the system can be caused by the existence of different magnetic phases at the interface and also due to the non detectable changes during sample preparation.

name	**bilayers**	**thickness** χ	μ/**Atom**	H_c **OOP**	H_c **IP**
Splib 502	20	14.4 nm	0.110 μ_B	9.0 mT	2.5 mT
Splib 503	30	21.6 nm	0.273 μ_B	2.5 mT	2.8 mT
Splib 504	40	28.8 nm	0.102 μ_B	4.8 mT	2.4 mT
Splib 485	50	36 nm	0.111 μ_B	10.7 mT	4.6 mT
Splib 486	75	54 nm	0.200 μ_B	2.6 mT	3.5 mT

Table 4.4: List of samples for which the SRT is studied as a function of the total thickness of the sample.

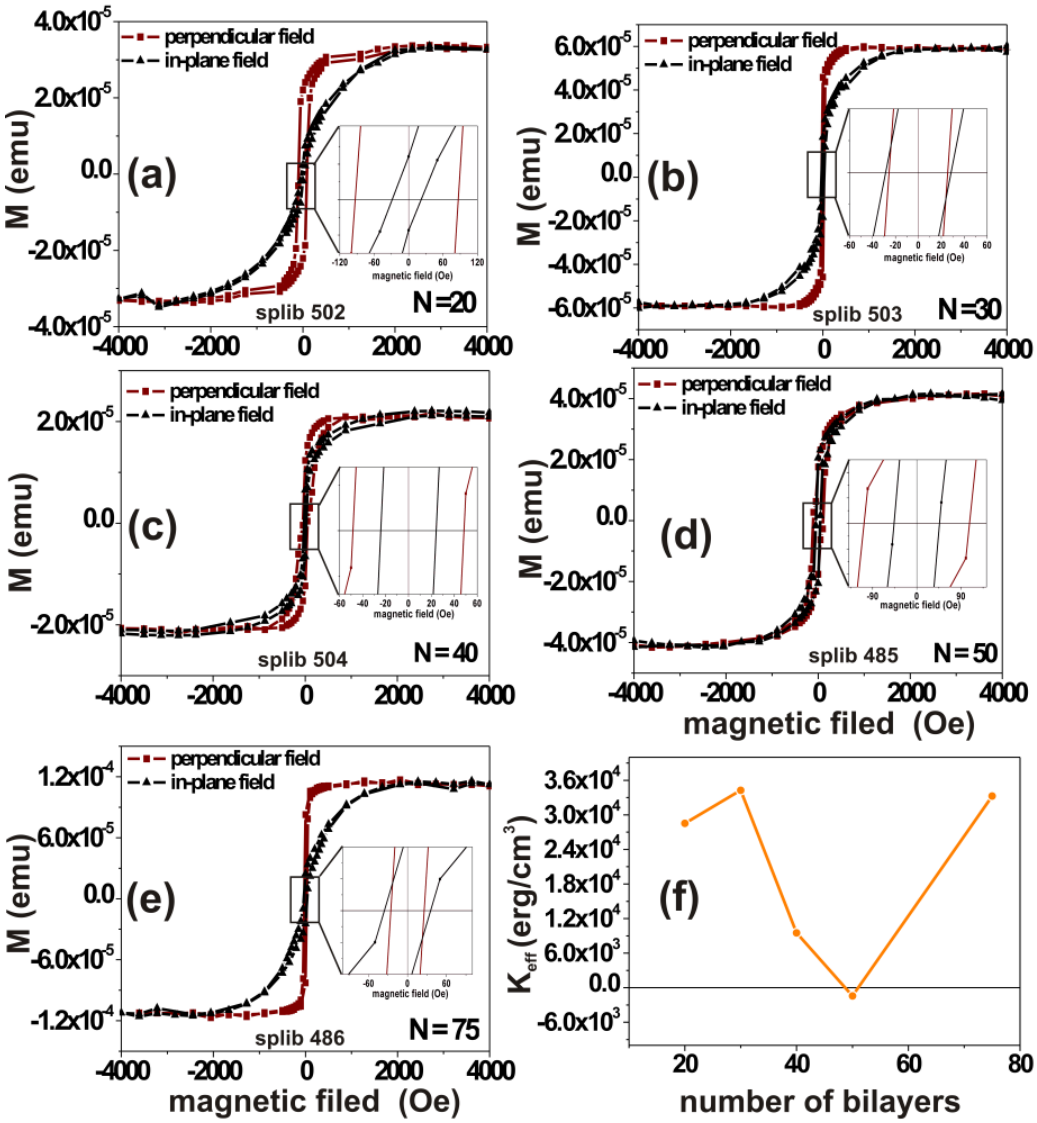

Figure 4.8: *In-plane and out-of-plane hysteresis loops measured by SQUID by varying the bilayers from 20 to 75 (a)-(e). The effective anisotropy, K_{eff}, is plotted as a function of the number of bilayers in (f).*

4.4 Temperature driven spin reorientation transition (SRT)

4.4.1 SRT studied by MOKE

Temperature dependent spin reorientation transitions of Fe/Gd multilayers have been studied by polar MOKE. A sample with a composition of [75×(Gd(0.36 nm)/Fe(0.36 nm))] has been sputter deposited on a silicon substrate. The temperature dependent hysteresis loops are shown in Fig. 4.9. A hard axis hysteresis loop is seen at room temperature (21°C). When the temperature is increased the hysteresis loops transform to a rectangular shape easy axis loop. This transformation is attributed to the reverse SRT in Fe/Gd multilayers where the magnetization direction changes from an in-plane to a perpendicularly magnetized state.

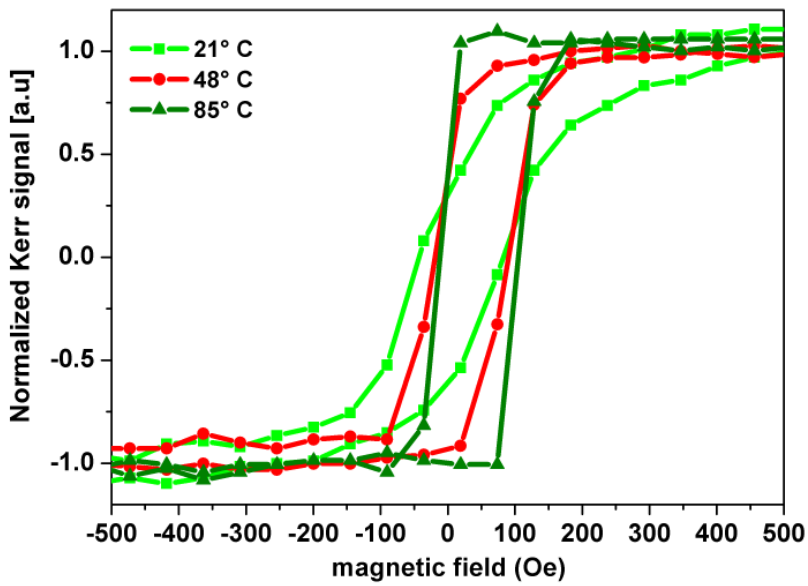

Figure 4.9: *Temperature dependent hysteresis loops measured by MOKE. A spin reorientation transition to a perpendicular magnetization direction is observed at* $85°C$.

4.4.2 SRT studied by X-PEEM

To get more insight into the SRT behavior the domain configurations of the sample have been imaged with x-ray photoemission electron microscopy (X-PEEM)

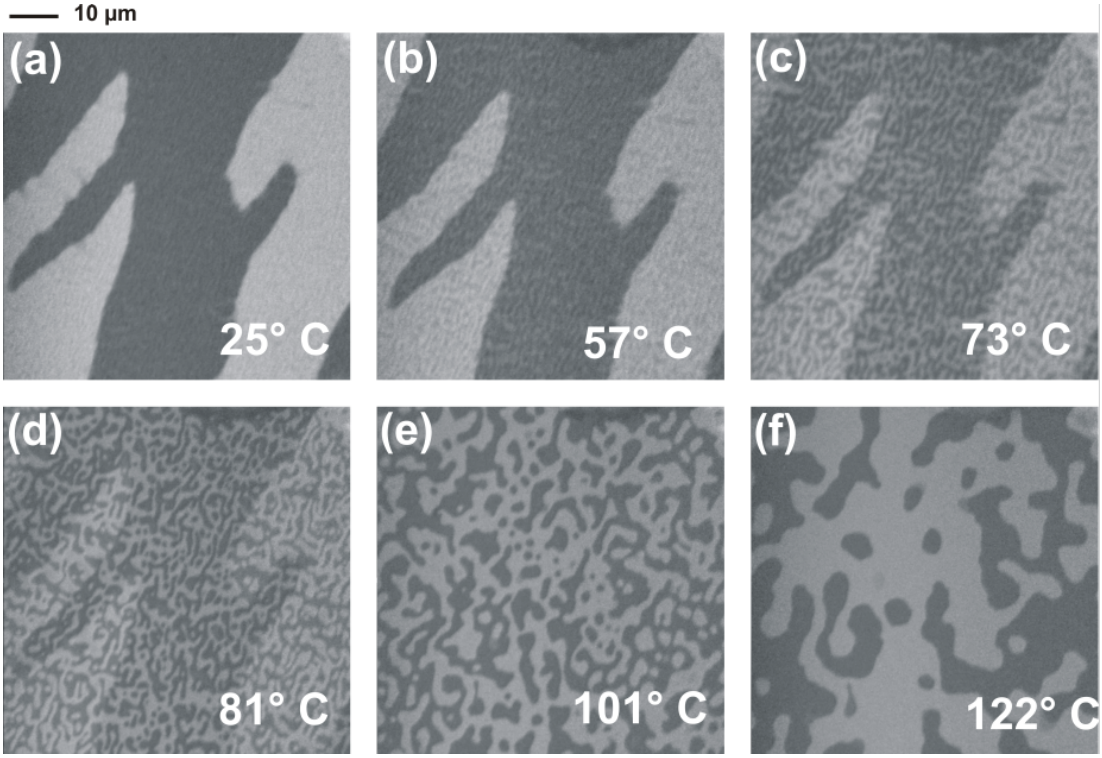

Figure 4.10: *Sequence of XMCD images taken by X-PEEM show a reverse SRT during heating. (a) At room temperature, large in-plane domains can be seen, (b) upon increasing the temperature perpendicular domains nucleate at* $57°C$*, (c), and (d) co-existence of both in-plane and perpendicular domains is visible at* $73°C$*, and* $81°C$*. Perpendicular magnetic domains are seen at elevated temperatures of* $101°C$ *(e), and* $122°C$ *(f).*

at beamline 7.3.1.1 of the Advanced Light Source (ALS). A small filament below the sample holder is used for heating of the sample. Images are taken with left and right polarized x-rays, with the energy tuned to the Fe absorption edge. XMCD images are deduced as discussed in section 3.5.6.

Fig. 4.10 shows the domain configuration of the sample during heating. At room temperature large in-plane domains are seen in Fig. 4.10 (a). This is in agreement with the hard axis hysteresis loop seen in MOKE measurements. Upon heating the sample the magnetic contrast of the in-plane domains decreases and very fine perpendicular domains nucleate, see Fig. 4.10 (b). At 73°C and 81°C a coexistence of in-plane and perpendicular domains is observed in Figs. 4.10 (c) and (d). Upon further heating of the sample the in-plane domains disappear gradually and only perpendicular domains are seen at $101°C$, and $122°C$, Figs. 4.10(e) and (f).

In order to check the reversibility of the SRT, the sample is cooled back to

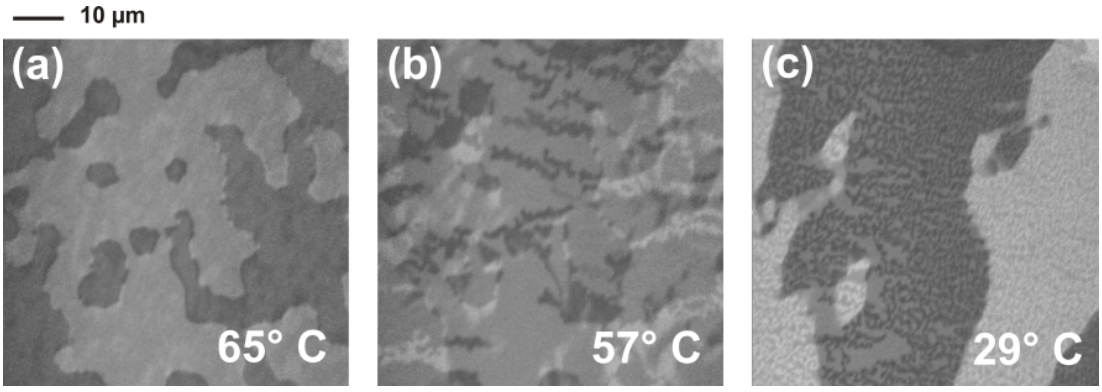

Figure 4.11: *Sequence of XMCD images taken by PEEM upon cooling. (a) At* $65°C$ *the contrast of perpendicular domains decreases dramatically compared to Fig. 4.10 (f), (b) perpendicular and in-plane domains co-exist at at* $57°C$*, (c) upon further cooling the sample to* $29°C$ *large in-plane domains are seen.*

ambient temperature. Fig. 4.11 shows the sequence of domain images taken while cooling the sample. A drastic decrease in the contrast of the perpendicular domains is noticed at $65°C$ in Fig. 4.11 (a) as compared to the image taken at $122°C$ (Fig. 4.10 (f)). Upon cooling the sample to $57°C$ large in-plane domains reappear and a coexistence of both in-plane and perpendicular domains can be seen in Fig. 4.11 (b). At 29°C the contrast of the large in-plane domains is increased, in addition, very fine perpendicular domains with reduced contrast level are also seen, see Fig. 4.11 (c). Comparing Fig. 4.11 (c) with Fig. 4.10 (a), the shape of the in-plane domain seen after heating and cooling cycle is almost the same apart from slight deviation. This infers that the in-plane domains are reversible. These changes in the magnetic contrast upon heating and cooling the sample shows that the SRT takes place by a continuous rotation of the magnetic moments.

4.4.3 Simulations of SRT

Micromagnetic simulations are done using the software MAGPAR [54]. A slab of 2 μm×2 μm × 50 nm of Fe/Gd film is meshed into finite elements, as explained in section 2.4. The exchange lengths of the sample given by Eqn. 2.8 and 2.9 are 21 nm and 26 nm, respectively. Therefore, a average cell size of 20 nm is used. The exchange stiffness A is assumed to be constant and set to A = 2×10^{-12} J/m [130]. Starting from a random orientation of magnetic moments the system is relaxed using the LLG equation. The effect of heating of the sample is incorporated by decreasing the value of the saturation magnetization in each simulation while keeping the other material parameters unchanged. In addition, temperature dependent changes in the intrinsic anisotropy are addressed in another set of

simulations by increasing the value of first order intrinsic anisotropy, $K_{u,1}$, while keeping the other values constant. However, thermal fluctuations can not be included in the simulations. Since only equilibrium conditions are investigated, the damping constant α is set to 1. Considering the random distribution of magnetization as initial condition, the energy of the system is minimized to a low energy domain configuration. Figs. 4.12 (a)-(d) show the x, y, and z component

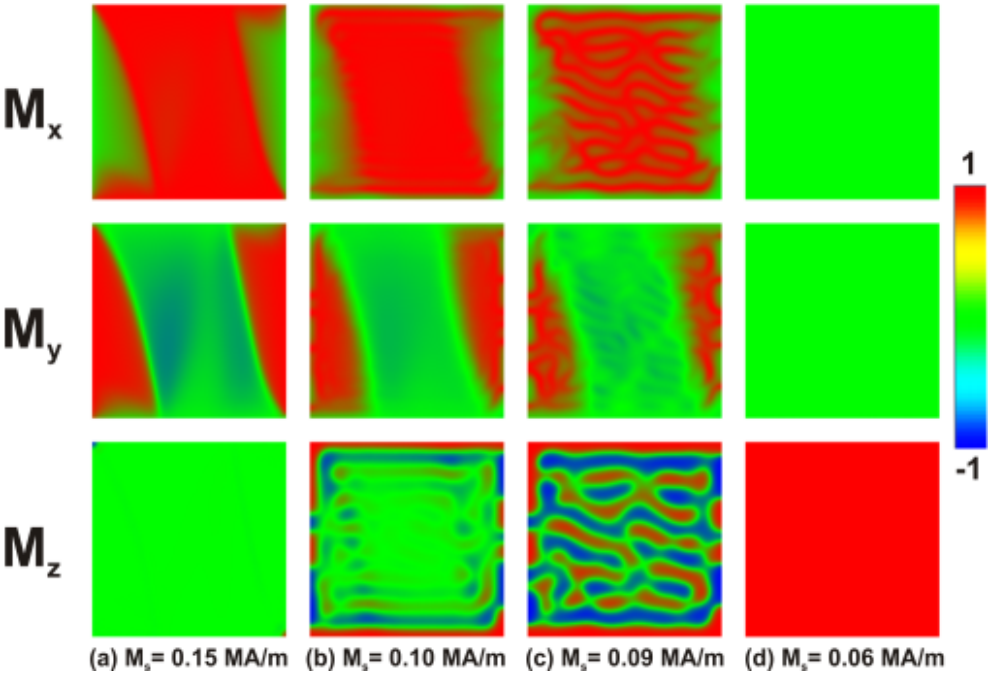

Figure 4.12: *The x,y, and z component of the simulated domain configurations showing the domain coexistence. The saturation magnetization (M_s) is decreased by moving from left to right (a)-(b).*

of the simulated images on decreasing the value of M_s. The first order uniaxial anisotropy $K_{u,1}$ is kept constant and set to $K_{u,1} = 4.4\times10^3$ J/m^3. An in-plane magnetized state is visible for $M_s = 0.15$ MA/m, whereas a perpendicular state is seen at 0.06 MA/m (see Fig. 4.12 (a) and (d)). For an intermediate value of $M_s = 0.10$ MA/m coexistence of both in-plane domains and perpendicular domains are visible in Fig. 4.12 (b). Upon further decreasing of M_s to 0.09 MA/m domain walls and perpendicular domains become more dominant, see Fig. 4.12 (c). The walls of blue and red domains in Fig. 4.12 (c) is more prominent in the x component, whereas the y component is dominant only at the edges. This can be due to the presence of domain walls between two in-plane domains as seen in the x and y component of Fig. 4.12 (a). Large domain wall width implies the low anisotropy constant.

Figs. 4.13 (a)-(d) show the x, y, and z component of the simulated images on

increasing the value of $K_{u,1}$. In this set of simulation the saturation magnetization M_s is kept constant and set to $M_s = 0.08$ MA/m. Similar to the simulation done by decreasing M_s, a coexistence phase is also observed by increasing the value of $K_{u,1}$.

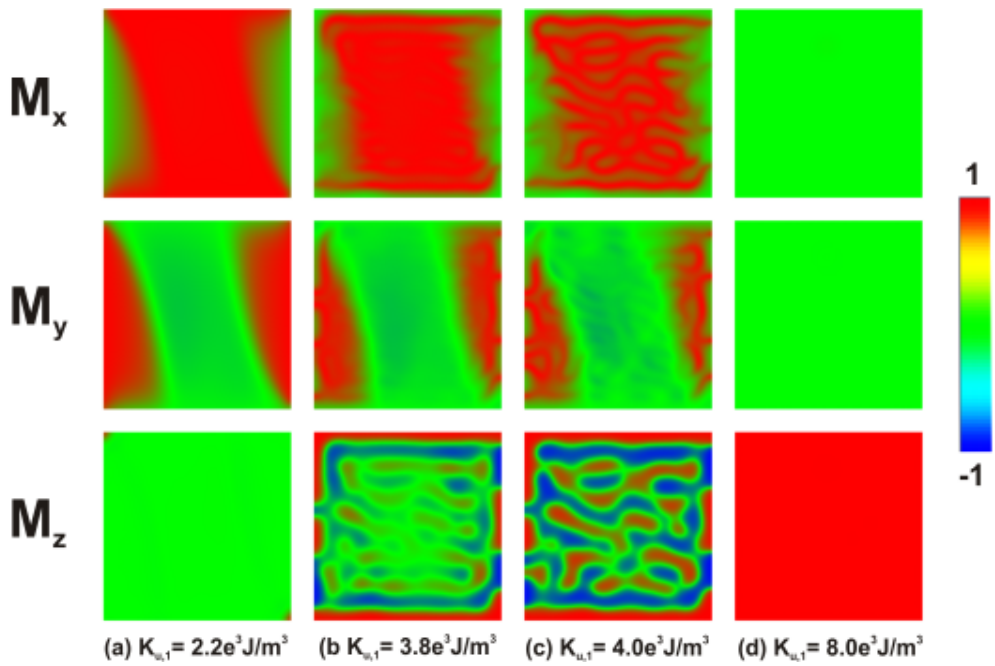

Figure 4.13: *The x,y, and z component of the simulated domain configurations showing the domain coexistence. The anisotropy constant (K_u) is increased by moving from left to right (a)-(b).*

Thus, both the experimental results and the micromagnetic simulation show that the magnetic moments rotate continuously during the SRT from an in-plane magnetized state to a perpendicular magnetized state. In addition, both in-plane and perpendicular domains coexist during these transitions. This is in contrast to the Monte-Carlo simulations [131] which show a coexistence of in-plane and perpendicular-domains for a negative value of second order uniaxial anisotropy $K_{u,2}$. Here, the coexistence phase has been explained by two local minima in the free energy. However, the simulations shown in Figs. 4.12 and 4.13 are performed for $K_{u,2}$=0. This deviation can be due to the thermal activation processes that are neglected in the MAGPAR simulation. Different temperature behavior of the surface anisotropy (K_S) and the volume anisotropy (K_V) may also cause two local minima in the total energy, which leads to the coexistence phase.

4.4.4 Towards a perpendicular magnetic state after repeated SRT cycles

By comparing the domain configurations after heating and cooling cycles, different contrast levels have been noticed in the images taken at ambient temperature.

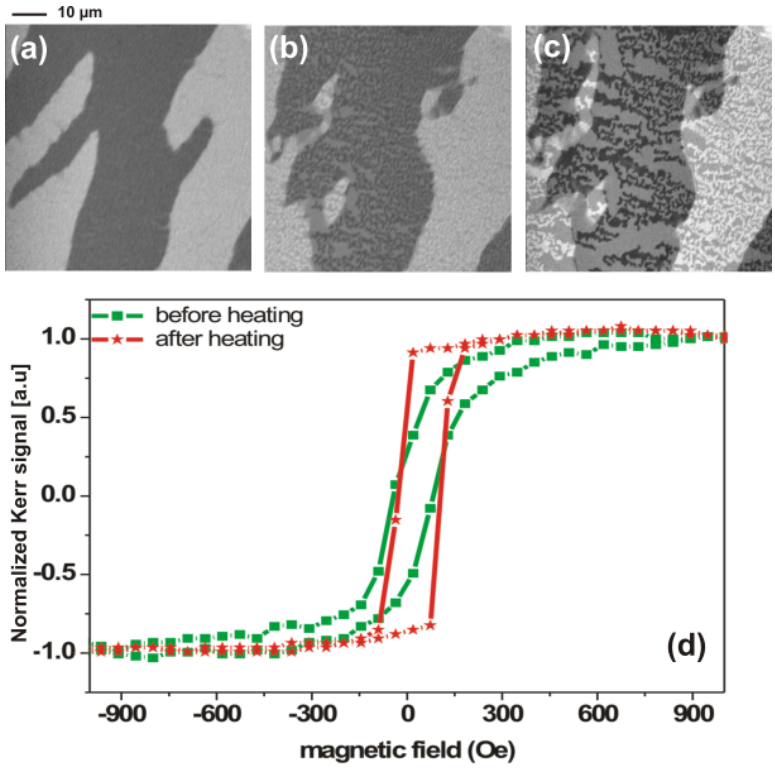

Figure 4.14: *The domain configurations of the sample ([75×(Gd(0.36 nm)/Fe(0.36 nm))]) at ambient temperature. (a) In-plane domains are seen before heating the sample, (b) after the first heating and cooling cycle of the sample, very fine, perpendicular domains coexist with in-plane domains, (c) the contrast of the perpendicular domains is increased after the second cycle, (d) MOKE Hysteresis loops measured before and after PEEM measurements also show that the sample has become more perpendicular.*

In Fig. 4.14 (a) large in-plane domains are present before heating of the sample. After the first cycle of heating and cooling, very fine perpendicular domains coexist with the larger in-plane domains, see Fig. 4.14 (b). The contrast level in the perpendicular domains has increased after the second cycle of heating and cooling , see Fig. 4.14 (c). This shows that the sample becomes more perpendicular after repeated SRT cycles. MOKE hysteresis loops measured on the same sample before and after the PEEM measurement are shown in Fig. 4.14

(d). The hysteresis loop measured after SRT cycles in PEEM is more rectangular than the hysteresis loop measured before. This substantiates that the sample has become more perpendicular after heating. In order to clarify the origin of this behavior the structural properties are studied by TEM analysis.

The same sandwich structure shown in Fig. 4.6 has been heated at 180° for one hour. For comparison, Figs. 4.15(a) and (b) show the TEM images before and after annealing, respectively. The corresponding MOKE-hysteresis loops measured on an in-plane magnetized reference sample are shown in (c) and (d). An easy axis magnetization loop is seen after annealing (Fig. 4.15 (d)). In addition, the layer structure has completely vanished in the in-plane part of the sandwich after annealing (lower part of Fig. 4.15 (b)).

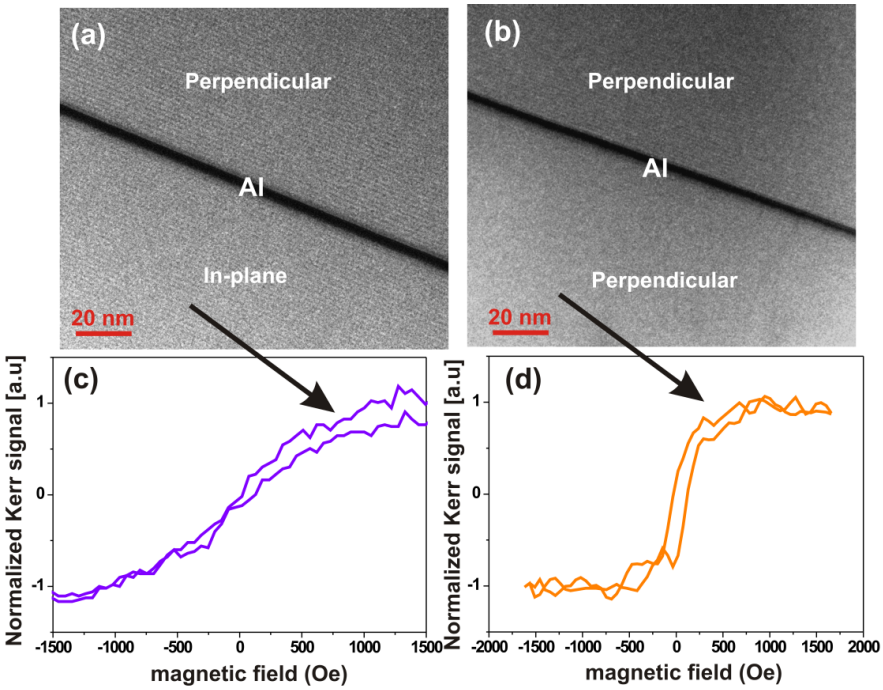

Figure 4.15: *Structural properties of Fe/Gd multilayers before and after annealing. The sandwich of in-plane and perpendicular Fe/Gd sample before (a), and after (b) annealing at 180° for one hour. The corresponding MOKE-hysteresis loops measured on an in-plane magnetized reference sample are shown in (c) and (d). After annealing the layer structure has completely vanished in the in-plane part whereas a faint layer structure are still seen in the perpendicular part.*

However, very faint layer structure is still seen on the perpendicular part of the sample. Since more broken interfaces are seen in the in-plane region of the sandwich structure, the inter-diffusion and inter-mixing after annealing is higher as compared to the perpendicular part of the sample. This infers that the perpen-

dicular magnetization seen after heat treatment is caused by the homogeneous intermixing of Fe and Gd atoms in the sample. Since the compositional dependence of K_u in amorphous GdFe alloys has already been reported [104, 132], the perpendicular magnetization that emerges after heat treatment is due to structural changes in the sample upon annealing.

4.5 Conclusion

1. A spin reorientation transition (SRT) from an in-plane magnetized state to a perpendicularly magnetized state is seen in Fe/Gd multilayers by decreasing the sublayer thickness from 0.60 nm to 0.36 nm. These changes are quantitatively explained by the competition between surface/interface and volume anisotropy terms in the system. From TEM analysis it has been found that almost homogeneous interface between the Fe and Gd layers lead to a perpendicular magnetic anisotropy (PMA) whereas, inhomogeneous intermixing at the interface causes an in-plane magnetization. These analysis show that the distribution of Fe and Gd atoms according to the dipolar interactions (pair ordering model) at the interface plays a major role in PMA of the sample. However, some samples prepared under identical conditions and thicknesses show either an in-plane or a perpendicular magnetic state. The undetectable variations in preparation conditions such as fluctuations in pressure, temperature or the bias voltage are believed to cause such changes in the magnetic properties.

2. The domain configurations during temperature driven SRT has been imaged by x-ray photoemission electron microscopy. A sample (75×[Fe (0.36 nm)/Gd (0.36 nm)]) that showed an in-plane magnetization at room temperature is studied in detail. During the SRT a coexistence of in-plane and out-of-plane domains are seen in a temperature range of 57° - 81° C. Micromagnetic simulations are consistent with the experimental observation. The different temperature behaviors of the surface anisotropy (K_S) and the volume anisotropy (K_V) is believed to cause such coexistence phase.

3. After several SRT cycles the sample equilibrates into a perpendicular magnetic state as a result of the structural and chemical changes in the sample. Transmission electron microscopy images show that the layered structure vanishes after heating of the sample to a maximum temperature of 180°C.

Chapter 5

Fe/Gd multilayers on nanospheres

As described in the introduction, magnetic systems with reduced dimensions are of great importance in high density data storage and sensor technology. Scalability, low cost, and large scale fabrication are important considerations for such applications. The limitations of optical and e-beam lithography have recently been overcome by the so called bottom-up approaches [33]. Albrecht *et al.* [42] proposed a new method to produce magnetic nanostructures based on depositing magnetic thin films on self-assembled polystyrene or silica nanospheres. Regular arrays of magnetic nanocaps can be formed. The thickness gradient in these caps alters the magnetic properties resulting in a new magnetic nanostructure [133]. This chapter deals with the magnetic properties of Fe/Gd multilayers deposited on such self-assembled nanospheres.

After a brief description of sample preparation, the magnetic properties of the system studied by scanning transmission x-ray microscopy (STXM) at the Advanced Light Source (ALS), Berkeley, CA, USA is addressed. First, the size dependence in the magnetization reversal of perpendicularly magnetized Fe/Gd multilayers, deposited on self-assembled monolayers of nanospheres, is discussed. Second, the change in the as-grown domain configuration, the spin structure and the magnetization reversal due to the increase of the total thickness of the film is studied. Experimental results are compared with micromagnetic simulations, done by finite element method using software developed by Sebastian Macke at the Max-Planck-Institute for Metals Research as explained in section 2.4. Finally, the properties of in-plane magnetized Fe/Gd multilayers, deposited on nanospheres, are discussed.

5.1 Sample preparation

A solution of commercially available silica nanospheres produced by Bangs Laboratories [134] is diluted in de-ionized (DI) water. The ratio of dilution is calculated depending on the diameter of the spheres and the density of the solution according to Micheletto *et al.* [135]. Silicon wafers and silicon nitride membranes (for transmission of soft x-rays) were used as substrates. Prior to the deposition of the prepared solution the substrates are cleaned chemically using the conventional RCA[1] wafer cleaning procedure [136] based on a two step wet oxidation treatment. Typically in the first step, known as RCA standard clean 1 (SC-1),

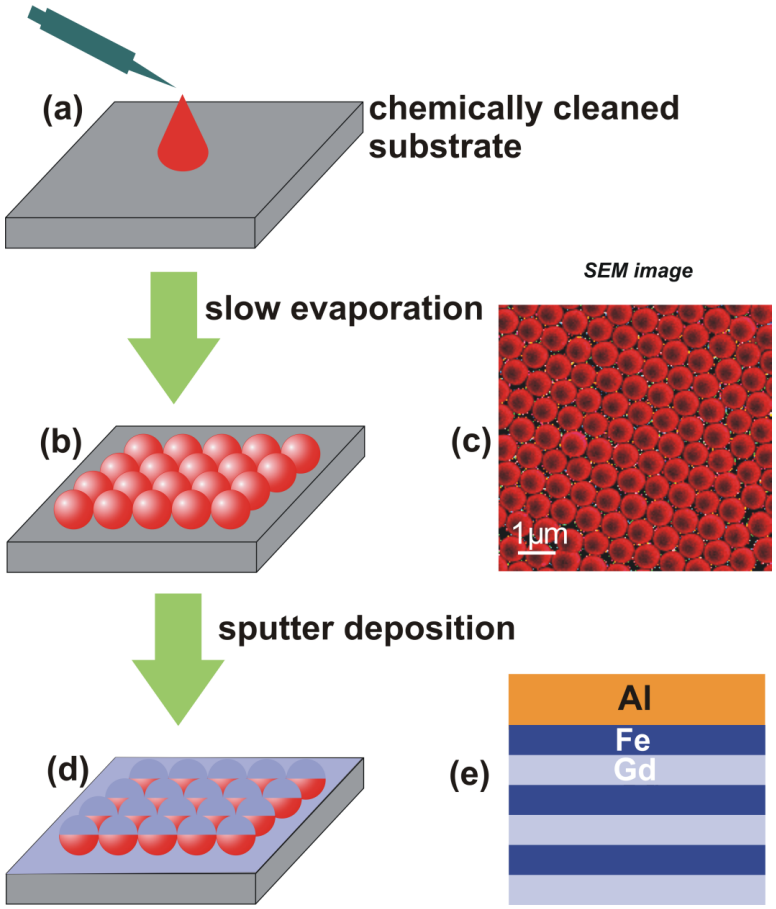

Figure 5.1: *Schematic diagram showing the steps involved in sample preparation, (a) a droplet of nanospheres is placed on a chemically cleaned substrate, (b) by slow evaporation a closely packed monolayer of nanospheres are formed, (c) SEM image of the self-assembled spheres, (d) a Fe/Gd system is sputter deposited on nanospheres, (e) cross section of Fe/Gd film with Aluminium as a capping layer.*

[1]Named after RCA laboratories

the substrates are heated to 70°C for 5 minutes in the mixture of deionized (DI) water, H_2O_2 (30%, aquaous solution), and NH_4OH (29%, aquaous solution) in the ratio of 5:1:1 vol. and followed by quench and rinse with ultra-filtered DI water. This procedure removes any remaining organics by oxidative dissolution and also removes metal contaminants from the surface.

The second step - standard clean 2 (SC-2)-uses a mixture consisting of 6:1:1 vol. DI water, H_2O_2 (30%, "not stabilized") and HCl (37%). The substrates are heated in this solution at 70°C for 5-10 minutes, followed by quenching and rinsing with DI water. SC-2 removes alkali ions and any residual metals that were not completely removed by SC-1, in addition, the surface transforms from hydrophilic to hydrophobic. After the two cleaning steps the substrates are dried with nitrogen. Fig. 5.1 shows the schematic diagram of the procedures involved in sample preparation. Using a Eppendorf micropipette, an appropriate volume of silica or polystyrene solution is pipetted out and placed on the cleaned substrates. In case of 1 cm×1 cm sample, 10 μl of the prepared solution is used and for 0.5 cm × 0.5 cm sample, 5 μl of solution is used. On slow evaporation in an air tight box, a closely packed monolayer of nanospheres is formed. The quality of the sample is checked by scanning electron microscope (SEM) [see Fig. 5.1].

A multilayered Fe/Gd system is sputter deposited on the nanospheres as explained in sec. 4.2. To prevent the sample from oxidation, 0.8 nm of Al is sputter deposited as capping layer. Due to the spherical geometry of the self-assembled nanostructure, a cap with a crescent shaped cross section is formed. The thickness at the center of the sphere reduces in radial direction towards the rim with $d \propto sin\theta$, where d is the thickness of the film and θ designates the position on the particle surface measured from the equator of the sphere [see the inset of Fig. 5.5].

5.2 Size dependence of the magnetic properties of nanospheres

In order to study the dependence of the magnetic properties on the diameter of the nanospheres, a multilayered [Gd (0.36 nm)/Fe (0.36 nm)]×50 system has been deposited on self-assembled silica nanospheres with 800, 330 and 160 nm diameter attached to a Si_3N_4 membrane. The magnetization of the system on a silicon substrate has been found to be perpendicular to the substrate as measured by magneto optical Kerr effect (MOKE) and superconducting quantum interface device (SQUID). Scanning transmission x-ray microscopy (STXM) at the beamline 11.0.2 of the Advanced Light Source (ALS) in Berkeley, CA, is used to study the magnetization reversal process and the domain configuration. X-ray magnetic circular dichroism, discussed in chapter 3.5.4, is used as a contrast mechanism. The sample has been studied in perpendicular geometry, i.e., with the sample

plane perpendicular to the x-ray beam, as shown in Fig. 5.2. A solenoid allows application of an out-of-plane magnetic field.

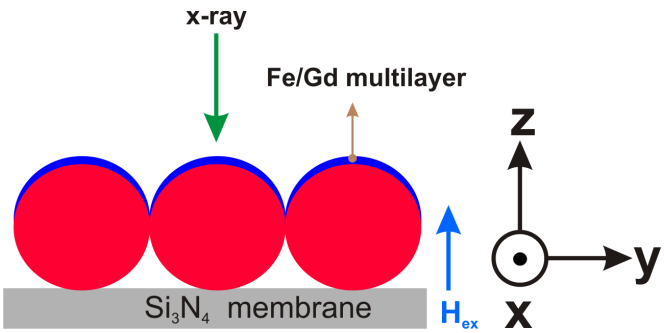

Figure 5.2: *Schematic diagram of the sample geometry used in STXM in which the incident x-ray and the applied field is perpendicular to the substrate.*

5.2.1 Domain configuration

Figure 5.3 shows selected STXM images of 800, 330 nm and 160 nm spheres, taken at the Fe L_3 absorption edge (707 eV) at different magnetic fields. The 800 nm spheres show a saturated state with dark caps at 330 Oe, see Fig. 5.3 (a). By decreasing the magnetic field, bright domains with opposite magnetization nucleate at the rim of the spheres, as shown in Fig. 5.3 (b). At small magnetic fields, magnetization reversal takes place by domain wall motion around the rim. At a field of -160 Oe [see Fig. 5.3 (c)], the bright domain moves over the center of the sphere, leaving behind only a small dark domain at the rim. Finally, saturation occurs at -330 Oe, as shown in Fig. 5.3 (d). The 330 nm and 160 nm spheres exhibit a different reversal behavior as compared to 800 nm caps: Fig. 5.3 (e) reveals that not all caps are saturated at a field of 330 Oe. Already at 92 Oe, i.e., without changing the sign of the magnetic field, most of the 330 nm particles show a two domain state [see Fig. 5.3 (f)]. By further decreasing the magnetic field, magnetization reversal occurs by domain wall motion, similar to the 800 nm caps. Spheres of 160 nm also exhibit similar features [see Fig. 5.3 (i)-(l)]. However, a distinct difference is that, the magnetic contrast is reduced as the magnetic field is increased [see Figs. 5.3(g) and 5.3(h) for 330 nm spheres and Figs. 5.3(k) and 5.3(l) for 160 nm spheres]. Interestingly, for all three diameters, the triangular magnetic structures in the interstices, between the spheres on the flat substrate show opposite contrast with respect to the nanocaps. At 330 Oe, when the spheres are dark, these patterns appear bright [see the marked circles in Fig. 5.3 (a)], and vice versa in Fig. 5.3 (d) at -330 Oe. The opposite sign of the magnetization can be explained by strong dipolar interaction between the soft magnetic multilayers on the spheres and on the flat substrate [137].

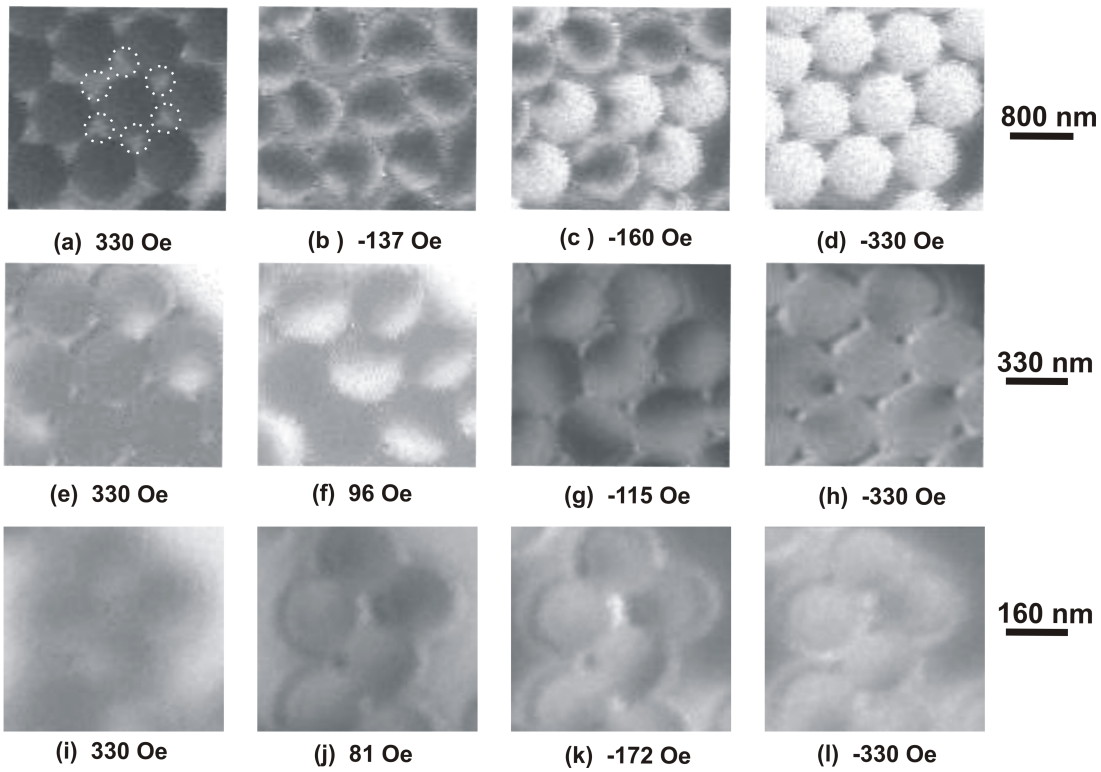

Figure 5.3: *A Fe/Gd multilayer changes its reversal behavior if deposited on spheres with diameters of 800 nm [(a)–(d)] or 330 nm [(e)–(h)] or 160 nm [(i)–(l)]. The STXM images are taken at different applied magnetic fields. Note, that the magnetic film in the interstices between the spheres [some are marked in (a) with dotted circles] show opposite contrast, i.e., reversed magnetization, with respect to the caps on the particles.*

5.2.2 Magnetization loops

As the XMCD signal is proportional to the magnetization of the sample, local, element selective hysteresis loops [45] can be deduced by integrating the magnetic contrast within individual nanospheres (see section. 3.5.5). Figure 5.4 shows that the size of the caps significantly changes the magnetization curve. The S-shaped loop of the 800 nm spheres indicates magnetization reversal takes place by domain wall motion and rotation of magnetic moments. In contrast, the 330 nm spheres show a sharp switching of the magnetization at 110 Oe, obviously induced by a sudden movement of a domain wall. A similar curve but with a smaller coercive field is observed for caps with a diameter of 160 nm. The hysteresis loops for 160 and 330 nm spheres differ drastically from the 800 nm loop. In addition to the sharp switching, the smaller caps show a strong reduction in the XMCD contrast with increasing magnetic field. The reason for this unconventional behavior will be discussed later.

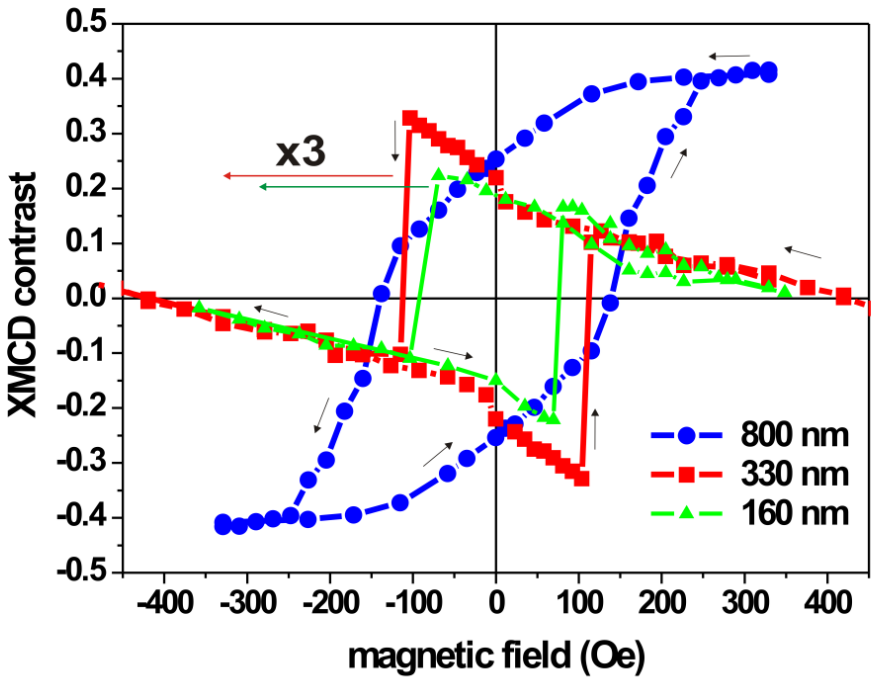

Figure 5.4: *Magnetization loops as deduced from the XMCD signal at the Fe L_3 edge, locally integrated on individual spheres with diameters of 800, 330, and 160 nm. A strong change in the shape of the hysteresis is visible for caps with diameters of 800 and 330 nm, indicating a different, size-dependent reversal mechanism. For clarity, the signals of the 330 and 160 nm spheres have been increased by a factor of 3, and the sign of the XMCD contrast has been reversed.*

5.2.3 Spin configuration

To understand the size dependent changes in the magnetization loops, the spin configuration of the 800 and 330 nm caps has been studied during magnetization reversal process. Since the contrast in the STXM images is proportional to the projection of the magnetization onto the propagation direction of the x-rays, line scans provide quantitative information about the magnetization direction with 30 nm lateral resolution. The signal of two spheres has been averaged for the line scans through the center of the caps as shown in Fig. 5.5. The curves are presented as a function of the azimuthal angle θ, as defined in the inset, and were taken at zero magnetic field with the incident x-ray perpendicular to the sample plane. A symmetric profile with a peak at $\theta = 90°$, i.e., at the top of the cap, is observed for the 800 nm spherules. If a magnetic system with a uniaxial, perpendicular magnetic anisotropy is deposited onto a sphere, a radial magnetization distribution, i.e., locally perpendicular to the surface, is expected. A fit with

such a radial distribution gives good agreement for $\theta = 90°$. For larger angles a deviation occurs due to the stray field of a neighboring sphere. In contrast, a nearly constant signal with no prominent peak can be detected for the 330 nm spheres. This indicates a uniaxial distribution of the magnetic moments, where the moments are nearly parallel at all positions of the cap. Consequently, with

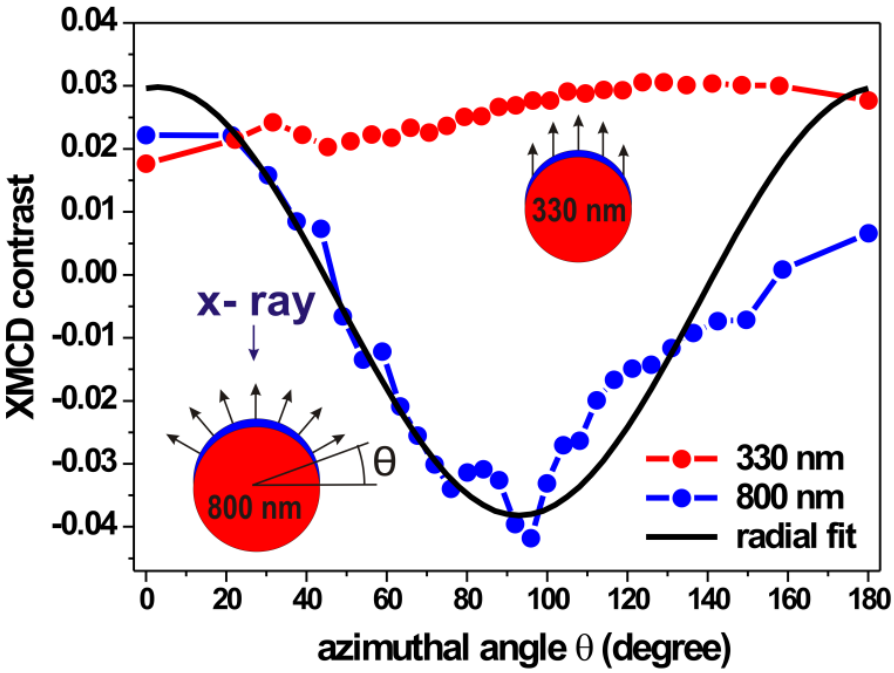

Figure 5.5: *Line scans of 800 and 330 nm caps reveal the spin configurations sketched in the insets. A radial distribution is used to fit the 800 nm signal. Deviations of the STXM data from the fit for angles $\theta > 90°$ result from dipolar interactions with a neighboring sphere.*

decreasing diameter of the caps, a transition in magnetization from a radial into a uniaxial distribution occurs. This transition is a direct consequence of two competing energies the exchange interaction, which favors parallel alignment of the moments and the radial magnetic anisotropy, preferring moments that are locally perpendicular to the surface. For smaller spheres, the curvature increases and thus the angle between adjacent moments also increases, which raises the exchange energy. As a consequence, with decreasing diameter of the caps, parallel alignment of the magnetic moments becomes favorable, resulting in the observed transition from a radial to a uniaxial magnetization distribution. The different magnetic distributions lead to significant changes in the magnetization reversal. For radial magnetization, the magnetic torque exerted by a perpendicular mag-

netic field changes from zero at the top of the cap to its maximum value at the rim. This radial torque gradient causes an inhomogeneous reversal of the magnetization of each cap, occurring in a broad magnetic field range. For uniaxial magnetization there is no gradient in the torque exerted by the perpendicular field on the magnetization, therefore 330 nm and 160 nm spheres show a sharp switching field and the shape of the hysteresis loop is more rectangular compared to the 800 nm spheres.

5.2.4 Comparison with micromagnetic simulation

Simulations of these nanopsheres are done using finite element methods as described in section 2.4. A sphere of 800 nm in diameter with an average cell size of 22 nm is used. The saturation magnetization M_s, the anisotropy constant $K_{u,1}$ and the exchange stiffness A were assumed to be constant and set to M_s = 0.06 MA/m, $K_{u,1} = 4\times10^3$ J/m^3, and A = 2×10^{-12} J/m, respectively. Since only equilibrium conditions are simulated, the damping constant is set to 1. Fig. 5.6 shows the simulated results in case of (a) radial and (b) uniaxial anisotropies. For radial anisotropy, the magnetization direction is radially perpendicular to the curved substrate, in contrast to uniaxial anisotropy, where it is perpendicular to the substrate [schematically shown in Fig. 5.6 (a) and (b)].

Fig. 5.6 (a) shows the domain configurations of the magnetic caps with radial anisotropy at different external fields. The magnetic moments at the rim start to rotate coherently towards the field direction and at - 290 Oe a domain of opposite magnetization nucleates at the rim. On further increasing the field it moves uniformly towards the center of the caps and reaches a saturation state at 330 Oe. In the experiment the spheres with a diameter of 800 nm, show a similar behavior [see Fig. 5.3 (b) - (c)]. However, the evolution of the domains with increasing field is slightly different from that seen in the simulation. This difference can be caused by the dipolar coupling between the neighboring spheres and also due to the strong anti-parallel coupling between the magnetic layer on the spheres and on the flat substrate. Since a single magnetic cap is considered in the simulations such coupling effects are completely ignored. Nevertheless, the shape of the simulated hysteresis loop with radial anisotropy is in good agreement with the hysteresis loop observed for 800 nm spheres in the experiment [see Fig. 5.4].

Simulations done with an uniaxial anisotropy show a different behavior. In Fig. 5.6 (b), with decreasing field a domain of opposite magnetization nucleates close to the center of the spheres. At -697 Oe most of the center region is switched into a two domain state. Between -699 Oe and -710 the domains move towards the rim approaching a saturation state. A similar behavior can be observed in the experiment. A two domain state can be seen in the 330 and 160 nm spheres before reaching a saturation state [see Figs. 5.3 (f) and (g) for 330 nm and (j) and (k) for 160 nm]. In addition, the hysteresis loops of the 330 and 160 nm spheres

are similar to the uniaxial hysteresis loop in the simulation, showing a sharp switching field [Fig. 5.4]. Therefore, the change in the shape of the hysteresis loops upon decreasing the diameter of the spheres, as seen in Fig. 5.4, is due to the transformation of the anisotropy distribution from a radial type into an uniaxial type.

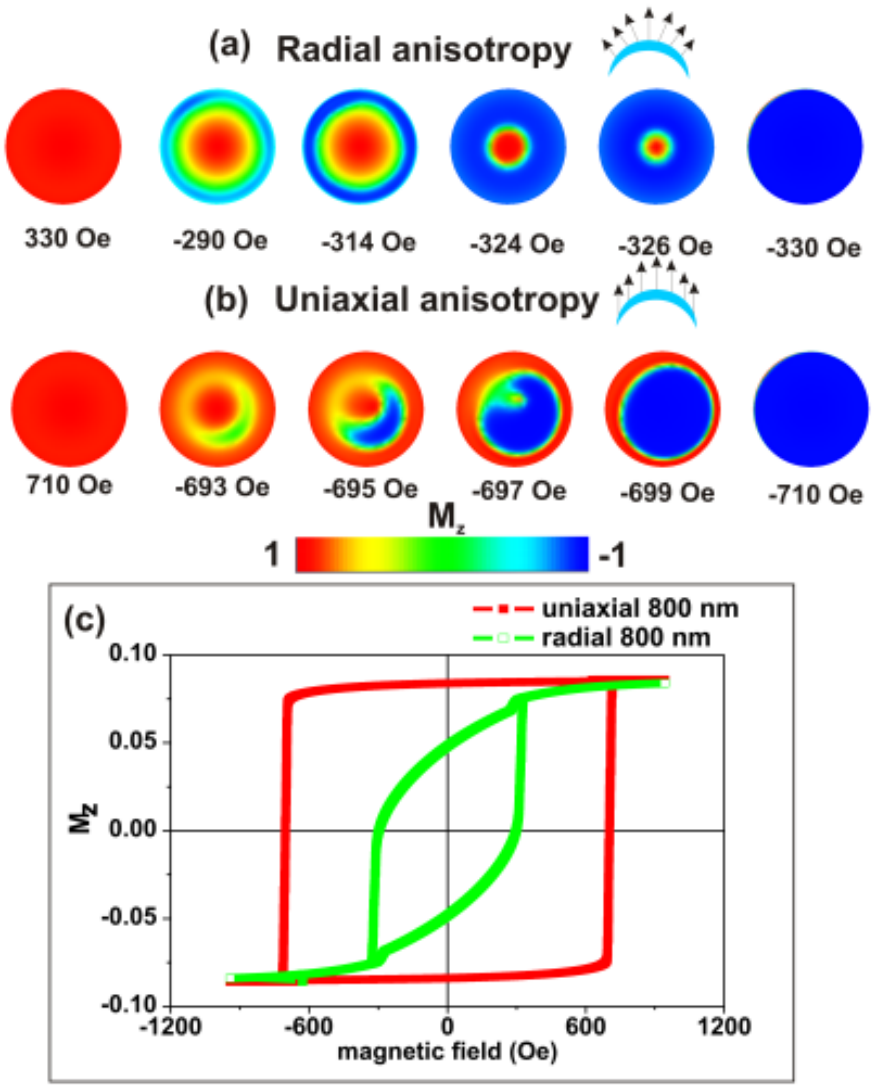

Figure 5.6: *Simulation of 800 nm spheres with (a) a radial and (b) a uniaxial anisotropy, the field is reduced on moving from left to right. (c) simulated hysteresis loops for radial and uniaxial anisotropies. A change in the shape of the hysteresis loop can be seen.*

5.2.5 Twisted magnetic state on smaller spheres

A decrease in the magnetic contrast with increasing magnetic field is seen in the hysteresis loops of 330 and 160 nm spheres (Fig. 5.4). This is due to the existence of a twisted magnetic state in the Fe/Gd multilayers as explained below.

Previous studies on multilayered Fe/Gd systems [94–96, 99, 100], [138, 139], revealed various phases that arise as a function of the bilayer thickness t, the applied magnetic field H, and the temperature T. The different temperature dependencies of the Fe and Gd moments and their antiparallel coupling [140] lead to a compensation temperature T_{comp} at which both moments are identical and thus compensate each other. Below T_{comp}, the Gd aligned phase occurs, whereas the Fe aligned phase is observed above T_{comp}. Finally, around T_{comp}, twisted phases exist, where the Fe and the Gd magnetic moments point under an angle to the applied magnetic field [138].

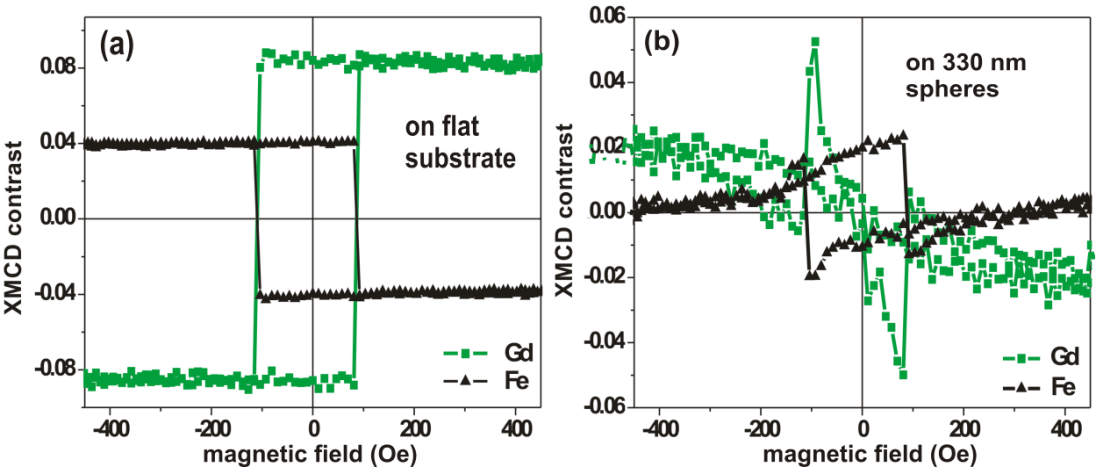

Figure 5.7: *Element selective Fe and Gd magnetization loops, taken at the Fe L_3 (707 eV) and the Gd M_5 (1190 eV) absorption edges. (a) Measurements for the Fe/Gd multilayers at the flat Si_3N_4 substrate. (b) The magnetization curves of the 330 nm caps reveal a twisted magnetic state.*

To investigate the coupling in the system, element selective Fe and Gd magnetization curves have been measured. Hysteresis loops are deduced by "magnetic field linescan" method as described in sec. 3.5.5. Figure 5.7(a) reveals a rectangular loop for the multilayer on the flat Si_3N_4 substrate. The dominance of the Gd signal indicates a Gd aligned state, in agreement with SQUID measurements of the system on a flat substrate that showed no compensation point in the temperature range from 4 to 350 K. However, for the 330 nm caps, distinct differences in the shape of the loops show up in Fig. 5.7 (b). With an exception of the field range between 100 and 200 Oe, the sign of the Gd signal is reversed, indicating a component which is antiparallel to the external magnetic field. Furthermore, the

signal is smaller, showing a nearly vanishing remanence and a peak at around 100 Oe close to the coercive field H_c. The signs of the Fe and Gd peaks suggest a Fe aligned state for fields below H_c [139]. Above H_c, the Fe signal steadily decreases with increasing field, which can also be observed for the 160 nm spheres in Fig. 5.4. This is a clear evidence for a twisted state in which the Fe moments gradually tilt away from the direction of the applied magnetic field. Comparing the Fe magnetization loops of Fig. 5.4, one can deduce that the twisted state occurs only for small nanospheres. Its occurrence might be explained by a reduction of T_{comp} with decreasing size of the nanocaps.

5.3 Thickness dependence of the magnetic properties of nanospheres

In order to study the magnetic properties of the Fe/Gd nano caps as a function of film thickness, a system with an increased number of bilayers [Gd (0.36 nm)/Fe (0.36 nm)]×75 is deposited on the silica spheres with a diameter of 800 nm as described before. The total thickness of this sample is 54 nm, as compared to 36 nm of the sample studied in the previous section. Studies are performed with STXM by applying both an in-plane and a perpendicular magnetic field. In this section the as-grown state and the magnetization reversal mechanism of 800 nm spheres with 36 and 54 nm thick Fe/Gd multilayers are compared.

5.3.1 As-grown domain configuration

Figure. 5.8 (a) presents the as-grown domain configuration of 800 nm spheres with 36 nm thick Fe/Gd film. The XMCD contrast of every sphere is high at the center and decreases azimuthally towards the rim of the sphere, resulting in a dark center and a light ring at the rim. A line scan through the center of a sphere is shown in Fig. 5.9. The integrated XMCD contrast along the line is plotted as a function of the azimuthal angle θ. A symmetric profile with a peak at $\theta = 90°$ is observed for the 800 nm spheres with a 36 nm thick film. The contrast distribution in the STXM images and the line profile show the presence of a radial magnetization distribution on the spheres. A fit with such radial distribution is in good agreement with the experimental data, see Fig. 5.9. Simulations done with a radial anisotropy distribution are also in good agreement with the domain configuration seen in the STXM images, see Fig. 5.8 (c) and (d).

In the case of 54 nm thick film, a different domain state exists on the spherules, see Fig. 5.8 (b). The majority of the spheres possess a single domain state, only about 10 % of the spheres show a two domain state. A line scan through the center of a sphere that shows a single domain state is plotted in Fig. 5.9. In contrast to the 36 nm sample, a nearly constant signal with no prominent peak is seen. This indicates a uniaxial distribution of magnetic moments on the sphere.

However, due to the decrease in the magnetization vector with the thickness of the film, a reduction in the XMCD signal is seen at the rim. Simulations performed with an uniaxial anisotropy also show a single domain state, see Fig. 5.8 (e). Upon changing the initial condition from a uniformly aligned state to a random distribution of magnetic moments, a two domain state emerges, see Fig. 5.8 (f). Therefore, a transition in the magnetization from a radial into a uniaxial distribution is seen in the as-grown state upon increasing the thickness of the film.

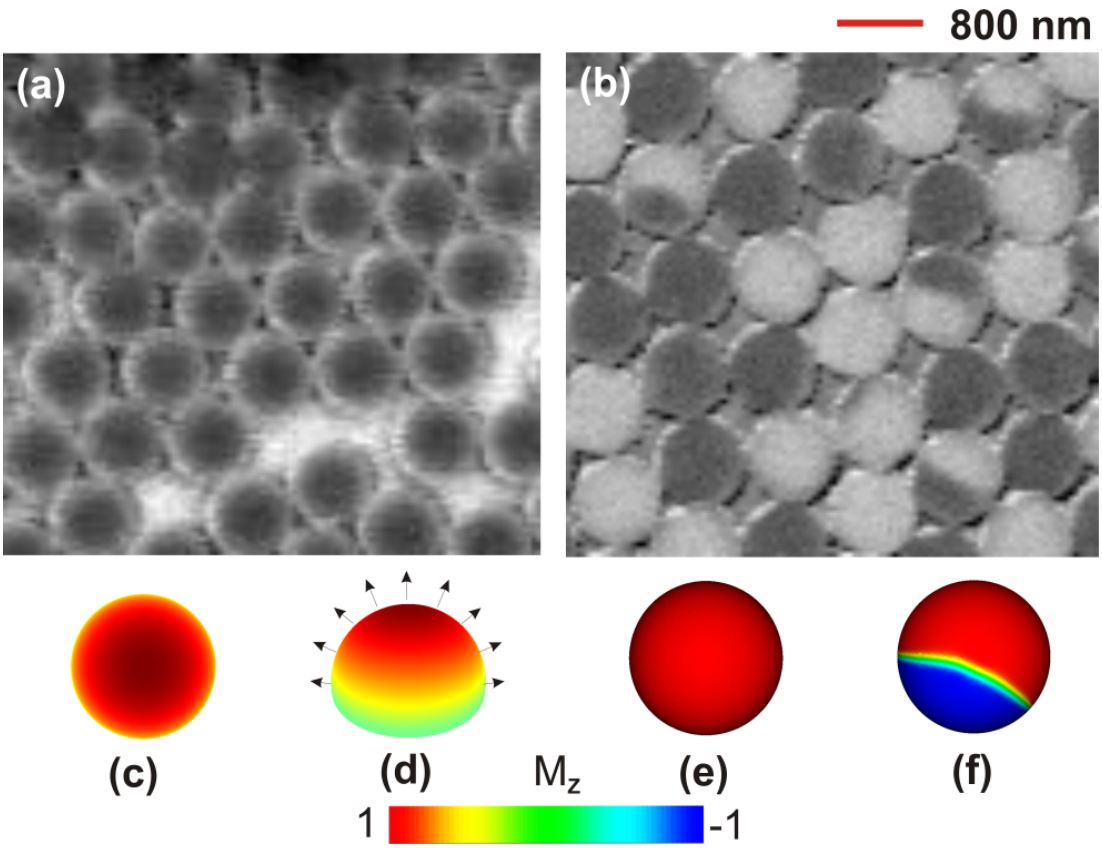

Figure 5.8: *(a) As-grown state of 800 nm spheres with, (a) 36 nm and, (b) 54 nm thick Fe/Gd system imaged by STXM. Simulation with radial anisotropy, (c) top view of a sphere, and (d) side view. Micromagnetic simulation with uniaxial anisotropy and with two different initial conditions namely, (e) a uniform magnetization in z direction and (f) a random magnetization.*

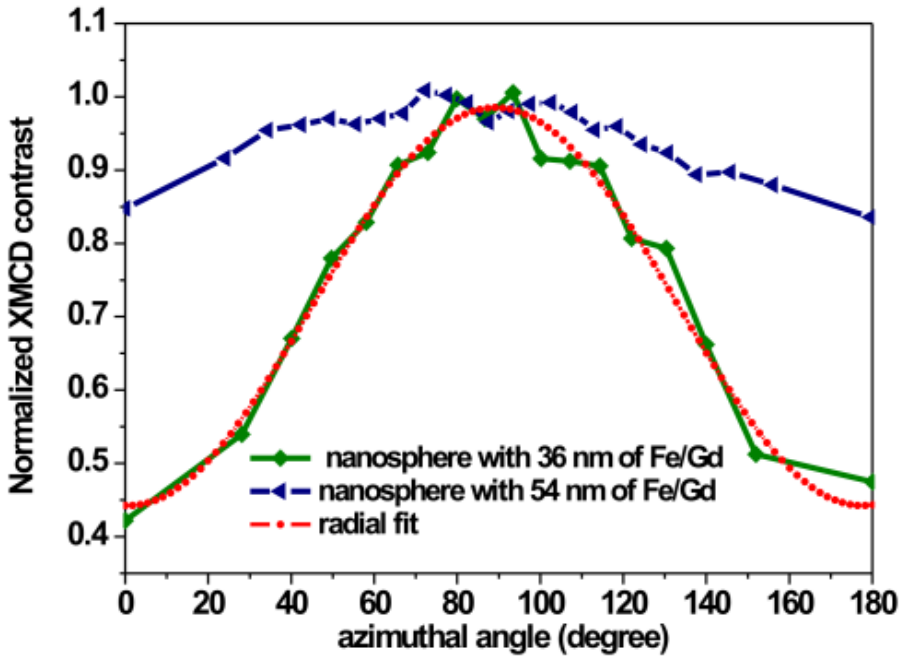

Figure 5.9: *Line scans of as-grown sample with 36 and 54 nm thick Fe/Gd multilayers plotted as a function of the azimuthal angle θ. A radial distribution of the anisotropy direction is used to fit the experimental data of the 36 nm sample. The signal of the 54 nm sample remains almost constant indicating an uniaxial spin distribution.*

5.3.2 Domain configurations while applying perpendicular magnetic fields

The sample with 54 nm Fe/Gd film is mounted with its plane perpendicular to the X-ray beam as shown in Fig. 5.2. Figure 5.10 shows a sequence of STXM images of nanospheres with 800 nm diameter. The energy of the X-ray was tuned to the Fe L_3 absorption edge (707 eV). In the following, the spheres are referred to the numbers shown in Fig. 5.10. At remanance [see Fig. 5.10 (a)] either dark or light spheres are visible and a slight change in the contrast level can also be noticed at the rim. After applying a maximum field of 658 Oe [Fig. 5.10 (d)] few spheres (1,3,4,6,7) have switched from a bright to a dark domain state, whereas the substrate is in a bright domain state due to the antiparallel coupling. Therefore, all the bright spheres in Fig. 5.10 (d) are those that have not switched in the applied field range. However, at the rim of all bright spheres a dark contrast is visible. Upon changing the direction of the magnetic field

similar switching process take place, see Fig. 5.10 (e)-(h). In general, only about 25% of the spheres reach a saturation state within the applied field range. The magnetization reversal at the rim of every sphere is different from the one in the center region. On every sphere the rim switches first and only at higher fields the center region undergoes a magnetization reversal by a sudden movement of a domain wall. Every sphere that switches with the field, exhibits a sequential

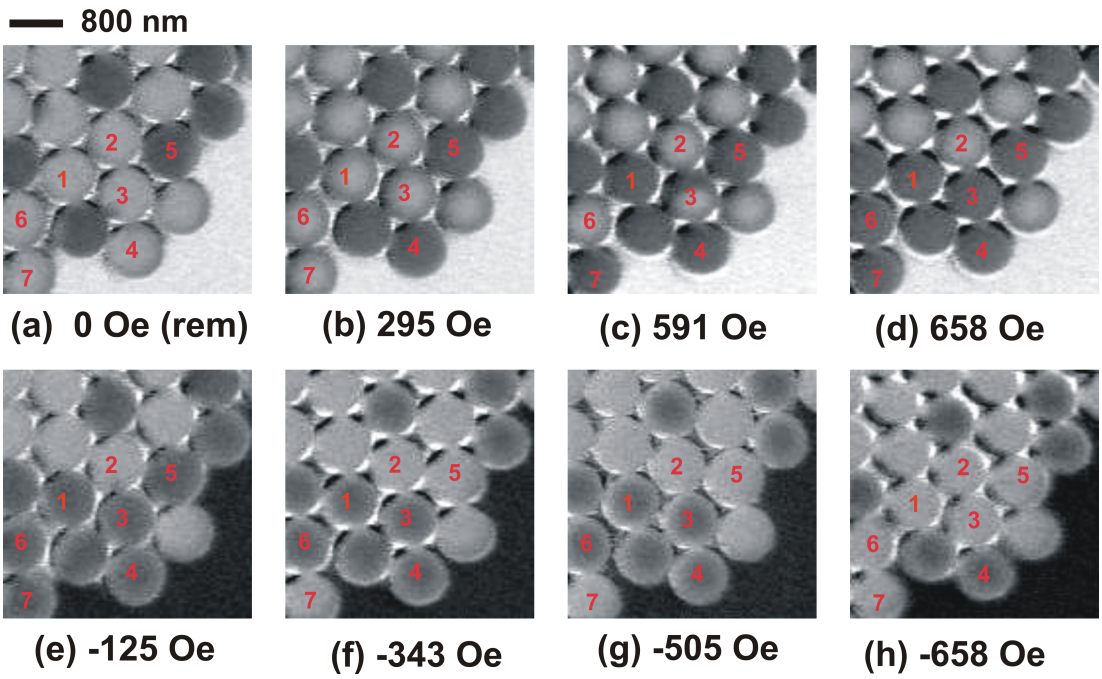

Figure 5.10: *STXM images taken at different magnetic fields applied perpendicularly to the sample plane. The spheres are referred to the numbers given in the images in the text.*

switching at a different magnetic field, i.e., they switch one after each other, and the switching field is not uniform for all spheres. Such a sequential switching mechanism has been reported to be a characteristic of strongly dipolar coupled nanostructures [141, 142]. Therefore, in this system, the dipolar interaction is believed to play a vital role in the reversal mechanism. It should be emphasized that the maximum field applied to this sample is twice as large as the maximum field applied to the sample with a thickness of 36 nm studied in the previous section. In the latter case a uniform saturation state is attained at 330 Oe [see Fig. 5.3 (d)].

5.3.3 Spin configuration and magnetization loops

In order to understand the reversal mechanism and the spin structure in more detail, a series of line scans, recorded at different fields, are deduced from the images. Fig. 5.11 (a) shows the line scans recorded from sphere 2 which doesn't switch within the applied field range whereas Fig. 5.11 (c) shows line scans of sphere 1, which shows switching. Apparent changes in the shape of the line scans can be seen. At 0 Oe, the line scans for both spheres show a very broad distribution. This reveals that the magnetic moments on the spheres are not

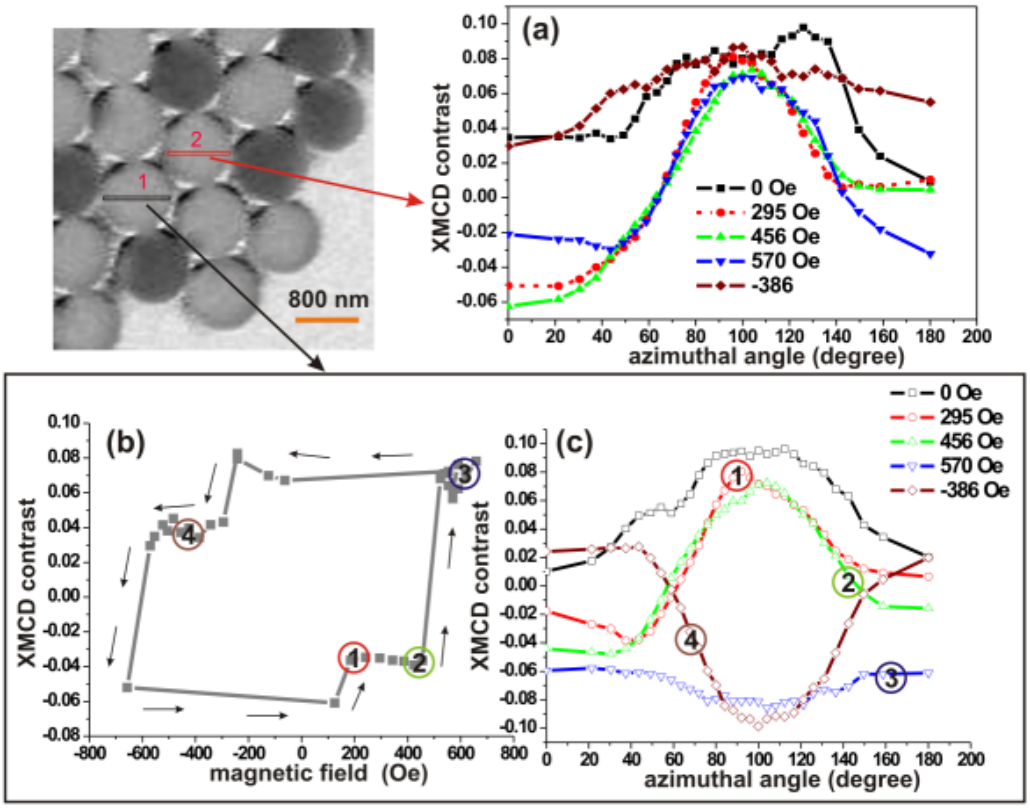

Figure 5.11: *(a) Line scans recorded from the sphere 2 that do not switch, (b) magnetization loop measured on sphere 1 that switches within the applied field range, and (c) line scans of sphere 1, measured at the field values indicated by number in (b).*

aligned radially to the surface of the spheres. In the case of a radial arrangement a peak in the center of the profile is expected. Upon increasing the field the line profile in Fig. 5.11 (a) gets narrower and, in addition, the sign of the XMCD contrast changes from positive to negative at about $\theta = 0°$ - $60°$. However, at

angles > 130° a different contrast level is seen. The presence of a neighboring sphere which undergoes switching is assumed to cause these small changes due to the strong dipolar coupling.

The hysteresis loop deduced from sphere 1, shown in Fig. 5.11 (b), turns out to be rather squared with prominent steps at 184 Oe and 455 Oe. Line scans recorded at the field values marked as 1, 2 and 4 in the hysteresis loops are also very narrow and show a negative XMCD contrast for $\theta < 60°$ and $\theta > 130°$, see Figs. 5.11 (b) and (c). Since the sphere switches its magnetization direction at 570 Oe, a negative and a flat profile is noticed, see line profile 3 in Figs. 5.11 (c). The line scans at saturation and remanent state are nearly flat, whereas a Gaussian type profile is observed at intermediate fields. In general, the line scans show contributions of both the magnitude and the anisotropic distribution of magnetic moments on the spherules. The profile of the saturated state reveals

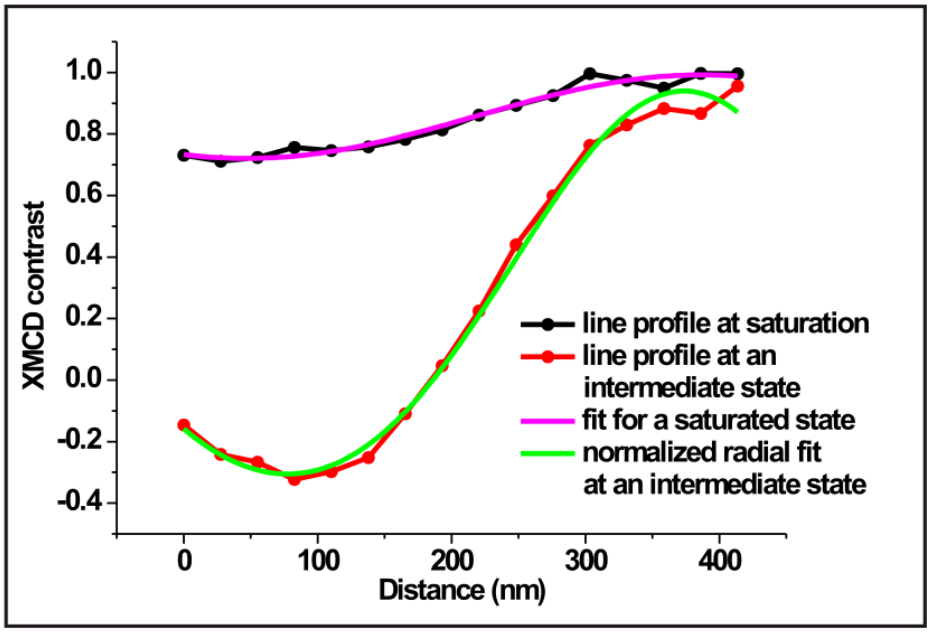

Figure 5.12: *A flower type reversal is seen from the analysis of the line scans taken at a saturated and an intermediate state. The profile at the intermediate field is fitted with a radial type profile normalized by the length of the magnetization vector deduced from the profile at a saturated state.*

the magnitude of the magnetization vector, considering that all the magnetic moments are aligned in the field direction. A cosine function can be used to fit the profile at saturation. Normalizing the profile taken at an intermediate field value with this function gives the actual distribution of the anisotropy on the sphere during the magnetization reversal.

Figure. 5.12 shows such an analysis done on sphere 2 where profile 4 of Fig. 5.11 has been normalized by profile 3. For simplicity, the sign of the XMCD signal is reversed and only the left half of the profile is considered. A radial profile, cos(90-φ), normalized with the fit function at saturation, i.e, the magnitude of the magnetization vector, is in good agreement with the the experimental data. This implies that a radial distribution of magnetic moments is present at intermediate field values, as indicated schematically in Fig. 5.13 (b).

Flower type magnetization reversal

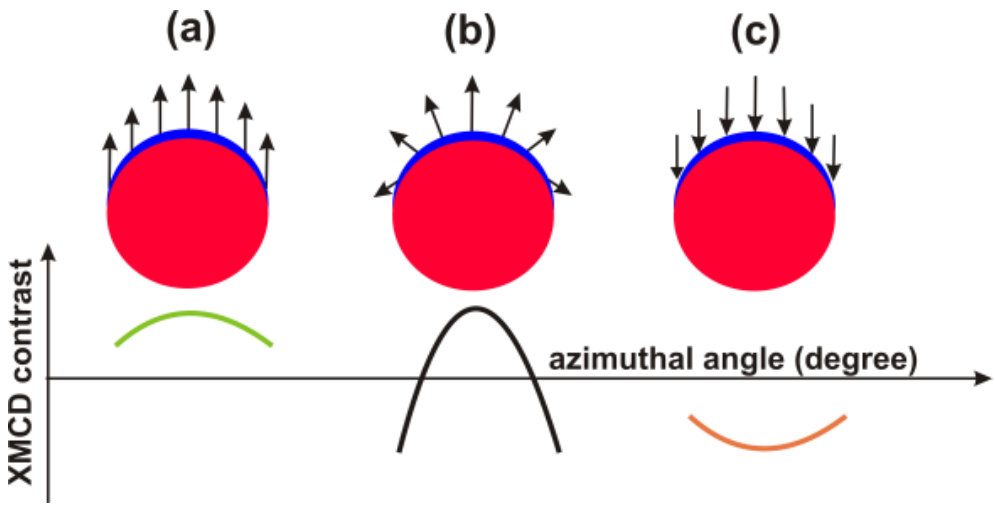

Figure 5.13: *A schematic representation of the spin structure during the magnetization reversal of sphere1 (top panel) and the corresponding line profile (bottom panel), (a) at 0 Oe, (b) at an intermediate field value at which the rim switches, and (c) at saturation.*

From these analysis and also by comparing the line profiles and the hysteresis loops a model for the magnetization reversal is deduced, which is schematically represented in the top panel of Fig. 5.13. The corresponding line profiles are shown in the down panel. At zero magnetic field, all the magnetic moments are parallel but have slightly reduced length towards the rim, resulting in a flat line profile as shown schematically in Fig. 5.13 (a). Upon increasing the field a flower type reversal in which the magnetic moments tilt radially towards the field direction takes place, see Fig. 5.13 (b). Consequently, a very narrow line profile is seen in Figs. 5.11 (c) (profile 1, 2 and 4) and Fig. 5.13 (b). The spheres maintain this metastable flower state until a sufficiently high field is reached to attain saturation. Therefore, the steps in the hysteresis loop of Fig. 5.11 (b) are due to intermediate metastable states with a radial distribution of magnetic moments.

5.3.4 Comparison of hysteresis loops

Compared to the 800 nm spherules with a 36 nm thick Fe/Gd film (see section 5.2), the reversal mechanism of this sample with a 54 nm thick Fe/Gd system is completely different. Figure 5.14 shows the hysteresis loops of 36 and 54 nm thick Fe/Gd systems on a flat substrate and on the 800 nm spherules. In former case a rectangular hysteresis loop is seen with no big changes in H_c upon increasing the thickness of the film. In contrast, thickness dependent changes can be observed for the system on the spheres. The caps with a 36 nm thick Fe/Gd system, show a S-shaped hysteresis loop with a switching field of 137 Oe. On the other hand, the spherules with a 54 nm thick cap of Fe/Gd display a squared loop with a higher H_c of 592 Oe. This shows that upon increasing the film thickness on spherules of the same diameter, H_c increases by a factor of four, whereas no prominent changes can be seen on the flat substrate.

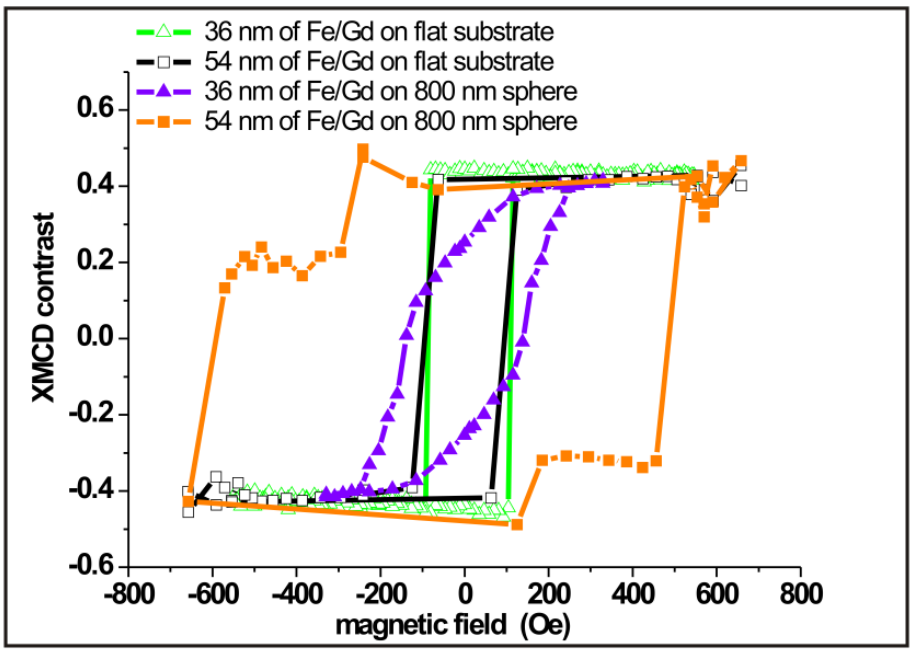

Figure 5.14: *A comparison of the magnetization loops of 36 and 54 nm thick Fe/Gd multilayers deposited on a flat substrate and 800 nm spherules show prominent changes in the reversal behavior. The loops are deduced from STXM images.*

To get more insight into these systems, local hysteresis loops are measured by integrating the XMCD contrast in concentric rings as shown in the inset of Fig. 5.15. As sketched, the angle θ corresponds to the elevation of the concentric rings on the sphere, measured from the equator.

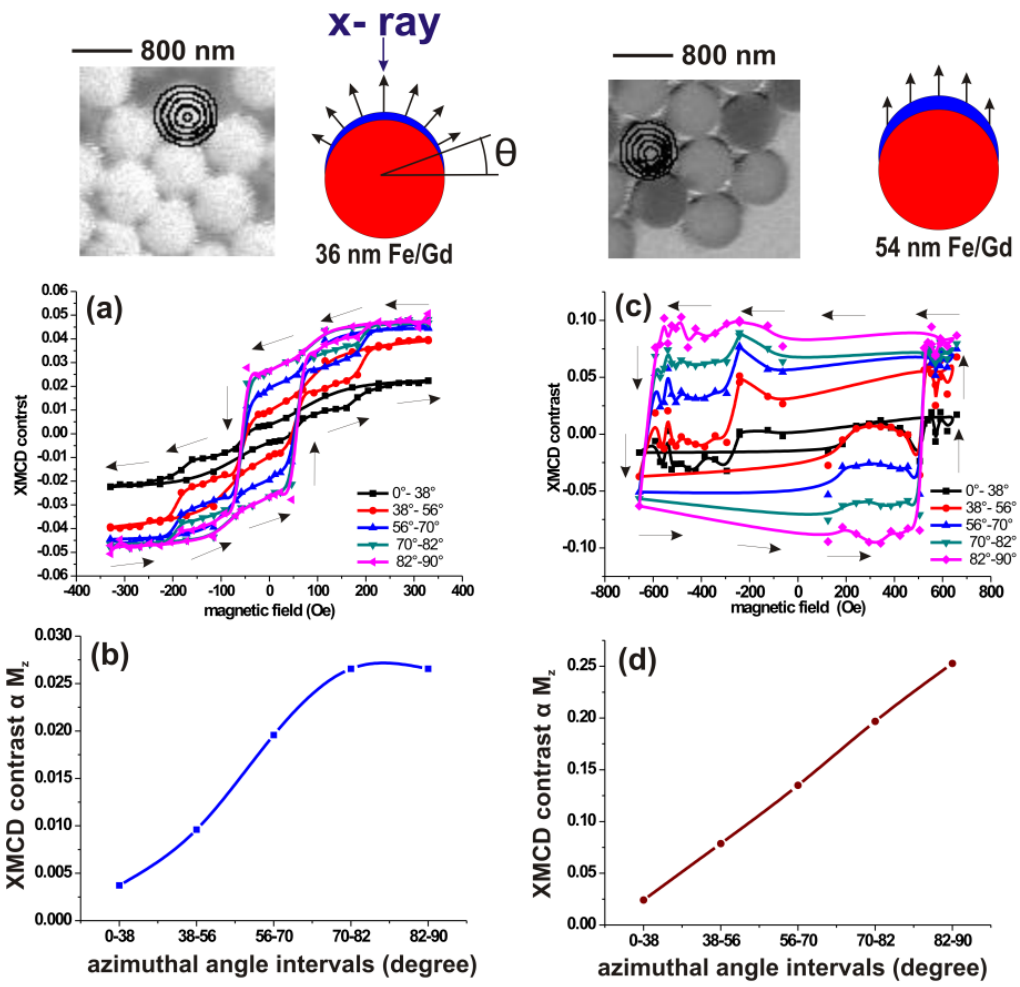

Figure 5.15: *Local hysteresis loops of a single sphere and the zero field XMCD profile at different azimuthal angles. A single nanocap is divided into concentric rings as shown in the insets (top). The XMCD signal, integrated in each of these concentric rings is plotted as a function of the external magnetic field. (a) Local hysteresis loops of a sphere with a 36 nm thick Fe/Gd film, (b) normalized XMCD contrast at zero field, (c) Local hysteresis loop of a sphere with a 54 nm thick Fe/Gd film, and (d) corresponding normalized XMCD contrast at zero field. The schematic diagram of the spin structure on both samples is shown on the top panel.*

Local hysteresis loops of a sphere with a 36 nm thick Fe/Gd film

Fig. 5.15 (a) shows the local hysteresis loops recorded on the caps with a 36 nm thick Fe/Gd film. Here, a hard axis loop is seen at the rim, $0° < \theta < 38°$, whereas the center region, $82° < \theta < 90°$, shows an easy axis loop. The features seen in

the magnetization loops are understood by looking at the STXM images taken at the corresponding field values, see Fig. 5.3.

Starting from a saturated state, the magnetization reversal at the rim ($0° < \theta < 38°$) takes place by a coherent rotation of magnetic moments between 226 Oe and 56 Oe, followed by nucleation and domain wall motion between -160 Oe and -204 Oe. As a result, prominent steps in the hysteresis loop are seen at the above mentioned field values in Fig. 5.15 (a). On the other hand, magnetization reversal at the center region, ($82° < \theta < 90°$), takes place by a coherent rotation of magnetic moments followed by a sudden switching of the magnetization. Consequently, a squared hysteresis loops is seen. Between $56° < \theta < 82°$ the reversal mechanism is similar, however, large steps in the hysteresis loops can be seen in the range $38° < \theta < 56°$. The field values at which the steps occur are the same as seen in the interval $0° < \theta < 38°$.

In Fig. 5.15 (a), the magnetization loop gradually transforms from a hard axis loop to an easy axis loop with increasing the elevation angle. In addition, the plot of the XMCD contrast at zero field as a function of the intervals of the azimuthal angle shows a smooth Gaussian like profile, see Fig. 5.15 (b). Both the results are a clear indication of a radial type of anisotropy.

Local hysteresis loops of a sphere with a 54 nm thick Fe/Gd film

Similar analysis done on the spherules covered with 54 nm of Fe/Gd multilayers show a completely different picture of the reversal mechanism, see Fig. 5.15 (c). For $0° < \theta < 38°$ a squared hysteresis loop with a sharp switching field of 246 Oe is observed. As explained before, the region along the rim switches abruptly and gives rise to this squared magnetization loop. For larger angles a similar square hysteresis loop with much larger H_c is seen. In consistence with the line scan analysis shown in Fig. 5.11 (c), the steps in the hysteresis loops at $38° < \theta < 32°$ are due to the intermediate flower state as explained before. The step height decreases gradually as θ increases. The concentric ring that lies closest to the rim exhibits the largest step in the hysteresis loops.

The XMCD contrast at zero field averaged over the intervals of θ, varies almost linearly with the azimuthal angle [Fig. 5.15 (d)]. The change in the length of the magnetization vector M with the thickness of the film [see Fig. 5.12] causes such linear behavior as sketched in the top panel of Fig. 5.15. Therefore, the reversal mechanism and the XMCD profile at zero magnetic field show an uniaxial type of anisotropy on the spheres with larger film thickness.

From the above studies it can be seen that the magnetic anisotropy on the spheres changes dramatically from a radial to an uniaxial type upon increasing the thickness of the film. This is anticipated because of the competition between the different anisotropy terms and the exchange energy of the Fe/Gd film on the spheres. It has been reported that the surface anisotropy, induced by the spherical nature of the particle plays a dominant role in the reversal mechanism

[143–146]. Bogdanov *et al.* have shown that in magnetic nanowires the surface anisotropies can lead to a continuous reorientation of magnetic moments from a homogeneous state to a vortex state [147, 148]. Kachkachi *et al.* [146] also found that in a spherical magnetic particle, the different ratios of the surface anisotropy and exchange energy term change the reversal mechanism and the shape of the hysteresis loop. Therefore, when a thin Fe/Gd film with perpendicular magnetic anisotropy is deposited on nanospheres, the surface and the bulk anisotropy terms dominate the exchange energy which results in a radial alignment of magnetic moments. Upon increasing the film thickness, the exchange energy overcomes the anisotropy energies which leads to a parallel alignment of the moments on the spheres. However, the crescent shaped magnetic structures studied in our experiments, also impose some additional parameters such as thickness dependence of the coercive field, H_c.

According to Uhlig *et al.* the coercive field, H_c, of a magnetic thin film scales linearly with the thickness [149]. Therefore, the H_c of Fe/Gd film at the rim of the spheres is lower as compared to the center. In case of uniaxial anisotropy, the magnetic moments are aligned parallel to the field direction and the torque exerted by the field is zero throughout the sphere. Due to the low coercive field at the thiner region, the rim switches before the center region of the sphere switches. In contrast, for radial anisotropy the magnetic moments at the rim are at oblique angles to the field direction and experience a large torque. In addition, H_c is also very low at the rim. Consequently, both the contributions favor a nucleation and coherent rotation of magnetic moments at the rim during the reversal process.

5.3.5 Magnetization reversal with in-plane magnetic field

To complete the magnetization reversal analysis the system is also studied by applying an in-plane magnetic field. In this case, the sample is mounted in 30° geometry as shown in Fig. 5.16. Figure 5.17 shows a series of STXM images taken at the Fe L_3 absorption edge (707 eV) while applying an external magnetic field parallel to the sample plane.

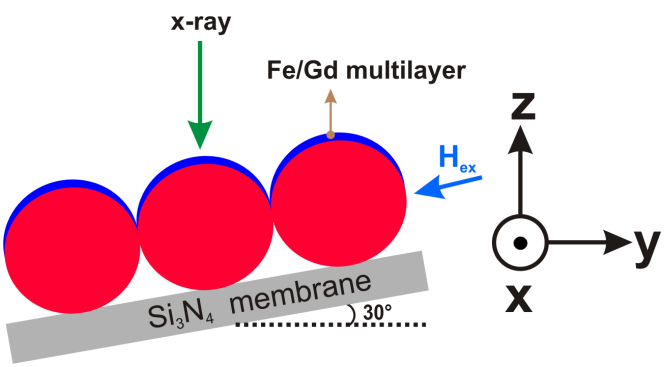

Figure 5.16: *Schematic diagram of the sample geometry studied by STXM while applying a in-plane magnetic field.*

Upon increasing the field from 0 to 1252 Oe, the Fe/Gd film on the flat Si_3N_4

substrate switches from a dark to a white domain state, whereas no switching could be observed on the spheres. Nevertheless, a slight change in the contrast is observed [see Figs. 5.17 (a)-(d)]. It should be noted that the maximum field applied to the sample is twice as high as that applied perpendicular to the sample [2]. Upon changing the field direction, similar behavior can be observed, see Figs. 5.17 (e)-(f). The Hysteresis loops deduced by integrating the XMCD signal on a flat region in the image sequence show a squared shape, see Fig. 5.18. The decrease in the XMCD contrast at higher field values is due to the 30° measuring geometry. Since the field is applied parallel to the substrate the magnetic moments rotate away from the x-ray direction towards the sample plane. Consequently the XMCD signal decreases due to the lower projection of the magnetic moments onto the beam direction. The integrated XMCD signal on a bright and a dark sphere remains almost constant while increasing the field, see Fig. 5.18. This indicates a strong uniaxial perpendicular magnetic anisotropy.

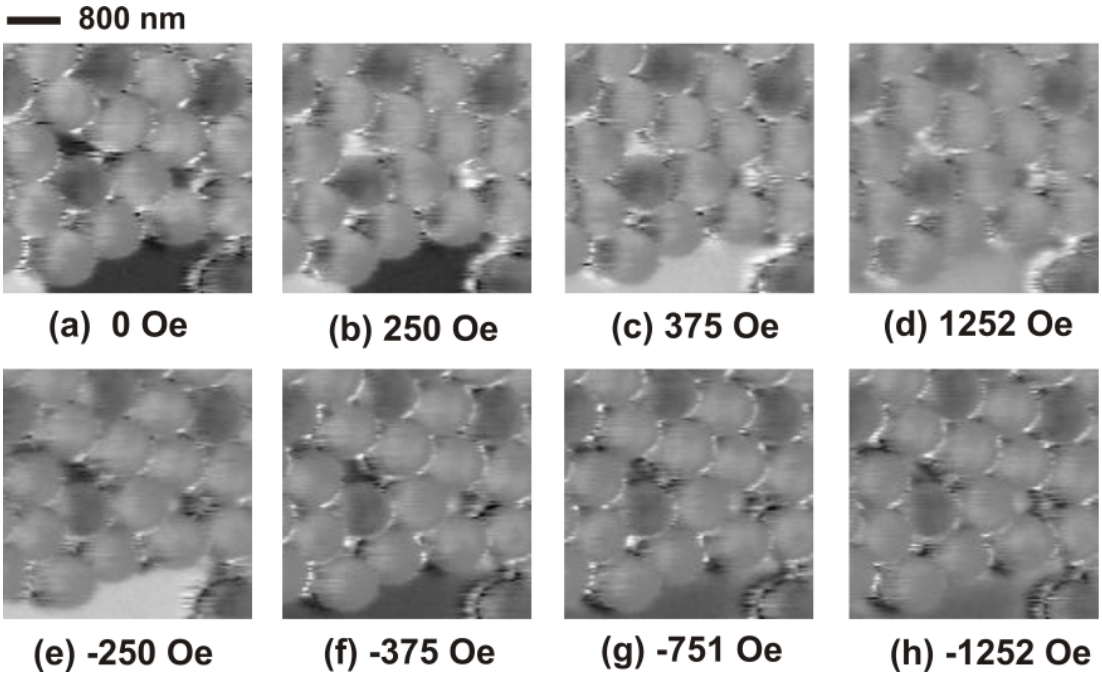

Figure 5.17: *STXM images at different magnetic fields applied parallel to the sample plane.*

[2]In the 30° geometry large electromagnets can be installed in the STXM setup whereas in case of perpendicular geometry only a small solenoid can be inserted.

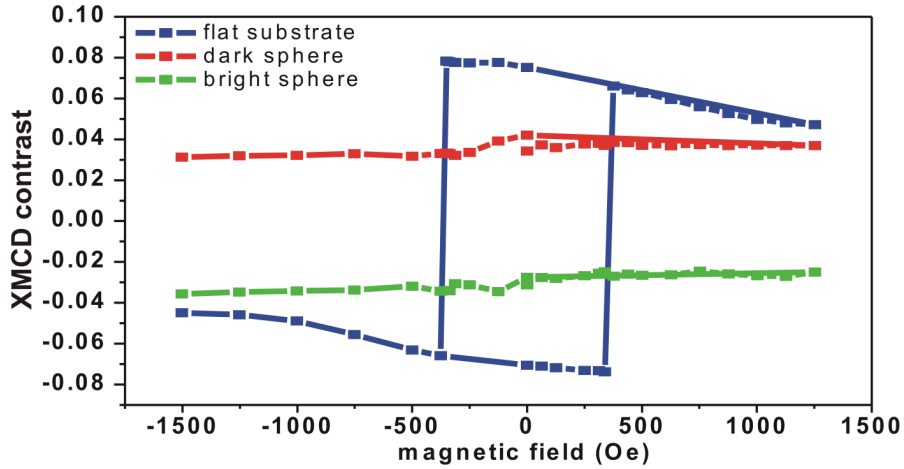

Figure 5.18: *Local hysteresis loops deduced from the image sequence recorded with an in-plane magnetic field. A squared hysteresis loop is seen for the film on the flat substrate, whereas an almost constant XMCD signal is seen on a dark and a bright sphere.*

5.4 Size dependent spin reorientation transition

In this section, properties of Fe/Gd samples with in-plane magnetization are studied on nanospheres. To facilitate a quantitative comparative study, one half of the Si substrate is coated with spheres and other is empty. A multilayered [Gd (0.36 nm)/Fe (0.36 nm)]×50 system has been deposited on the substrate.

5.4.1 Size dependent SRT probed by MOKE

Figure. 5.19 shows hysteresis loops recorded on spheres and on a flat substrate using the magneto-optical Kerr effect (MOKE) in polar geometry. The Fe/Gd system on a flat silicon substrate shows a hard-axis magnetization curve with a saturation field of 1250 Oe and with almost zero remanence. In contrast, a squared easy-axis loop with a much lower saturation field of 250 Oe and with a high remanence is observed for the Fe/Gd system deposited on spheres with diameters of 800, 330 and 160 nm. In order to see whether the material of the substrate influences the magnetic properties, a similar Fe/Gd system has been deposited onto polystyrene nanospheres of 810 nm diameter. The resulting magnetization loop, shown in Fig. 5.19 (b) is similar to the one obtained for silica nanospheres. This demonstrates that the change in the magnetic anisotropy is

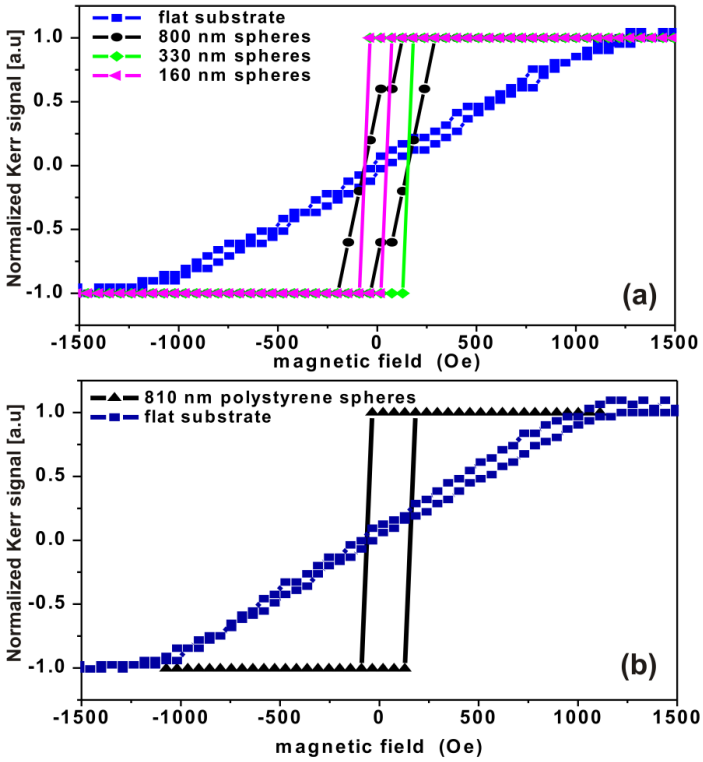

Figure 5.19: *The shape of the magnetization loop of a Fe/Gd multilayer, probed by polar MOKE, is different if the film is deposited on a flat substrate or on nanospheres. (a) A rectangular hysteresis loop is observed on silica nanospheres with diameters of 800, 300 and 160 nm, whereas the film on a flat substrate exhibits a hard axis hysteresis loop, and (b) similar effect seen on polystyrene nanospheres of 810 nm in diameter.*

independent of the material of the spheres. Consequently, the strong increase in the magnetic anisotropy is believed to be driven by the geometry of the spheres.

5.4.2 Size dependent SRT probed by STXM

To obtain insight into the microscopic processes underlying the macroscopic magnetization loops, the domain configuration has been studied by scanning transmission x-ray microscopy (STXM). For this investigation a multilayered [Gd (0.36 nm)/Fe (0.36 nm)]×50 system that shows an in-plane magnetization is studied on spheres with diameters of 800, 330 and 160 nm, self-assembled on an x-ray transparent silicon nitride membrane. The sample was mounted in perpendicular geometry as shown in Fig. 5.2. The magnetic field was applied perpendicular to

the sample plane. Figure 5.20 shows the as grown state of the sample. Spheres with a diameter of 160 and 330 nm exhibit a two domain state whereas 800 nm spheres show either a two domain or a vortex state. Fig. 5.21 (a)-(h) shows a

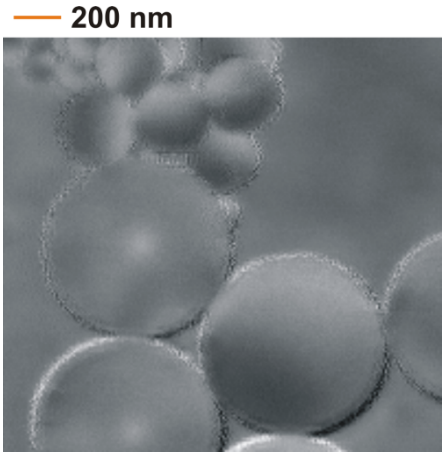

Figure 5.20: *As grown state of nanospheres with in-plane magnetization. Spheres with a diameter of 330 and 160 nm show a two domain state, whereas 800 nm spheres show a vortex or a two domain state.*

sequence of STXM images, taken at Fe L_3 edge, on decreasing a perpendicular magnetic field starting with a saturated state. At 100 Oe, domains of opposite magnetization nucleate at the rim. Upon further decreasing the field, the domains move around the rim. At -25 Oe the domains at the rim move over the center and reach a saturated state. Since the applied field in this sequence is less than the saturation field, some spheres are not completely saturated. Hysteresis loops are deduced from a line scan on a 800 nm sphere and on the flat substrate as explained in section 3.5.5 (Quantitative magnetic imaging with STXM). To increase the signal to noise ratio line scans of three individual spheres have been averaged. A hard axis loop, similar to that seen in MOKE, is observed on the flat substrate, see Fig. 5.21. The film on the flat substrate does not reach a saturation state within the applied field range. Whereas on 800 nm spheres a saturation state is reached at 300 Oe. However, the hysteresis loops deduced from STXM do not resemble the one seen in MOKE. In the latter case a more rectangular loop with a sharp switching field is seen. This can be due to the fact that in MOKE an ensemble of spheres is probed, whereas STXM images reveal a local average of three spheres. Nevertheless, the tendency of a reorientation from an in-plane to a perpendicular magnetization state is obvious for the system deposited on the spheres. This reorientation of the magnetization axis from in-plane to out-of-plane can be understood by the interplay between the shape anisotropy and the intrinsic anisotropy as explained below.

In a magnetic thin film the effective anisotropy is given by the sum of the intrinsic magnetic anisotropy of the film K_u and the shape anisotropy K_d:

$$K_{eff} = K_u + K_d \tag{5.1}$$

where

$$K_d = -\frac{1}{2}\mu_0 M^2 N \tag{5.2}$$

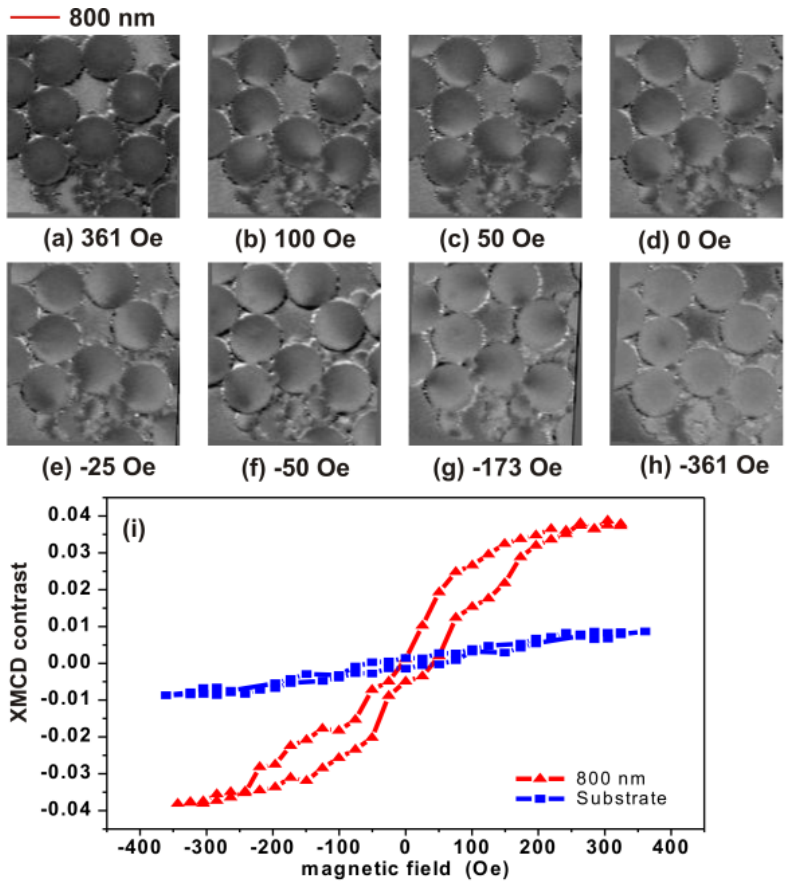

Figure 5.21: *STXM images at various perpendicular magnetic fields (a)-(h) and the hysteresis loops (i) measured on 800 nm spheres and on flat substrate show a strong increase in effective perpendicular magnetic anisotropy.*

N is the demagnetization factor. For crystalline material N is a tensor. For homogeneously magnetized isotropic materials it takes following values for three special cases: $N = 0$, for an infinite thin film magnetized in-plane, $N = 1$ for a thin film magnetized perpendicular to the surface, and $N = 1/3$ for a spherical particle. The competition between K_d and K_u determines the magnetization direction. Upon reducing the lateral size of the film, which resembles the situation on the spheres, the shape anisotropy decreases due the demagnetization factor N. As a result the effective anisotropy, K_{eff} increases. From the fact that for $K_{eff} > 0$, the film prefers to be magnetized perpendicular to its plane, an enhancement of the perpendicular magnetization is seen on the spheres.

The experimental observations are consistent with Monte Carlo [150] and OOMMF [151–153] simulations predicting a strong enhancement of the effective perpendicular magnetic anisotropy with shrinking lateral size of the sample.

5.5 Conclusion

1. Fe/Gd multilayers deposited on self-assembled nanopsheres are studied by scanning transmission x-ray microscopy. The magnetization reversal and the magnetic anisotropy show prominent changes with respect to the diameter of the spheres and the thickness of the films.

2. Nanospheres with a diameter of 800 nm exhibit a radial anisotropy whereas, 330 and 160 nm spheres show an uniaxial anisotropy. In case of radial anisotropy the magnetization reversal of each cap occurs in a broad magnetic field range. On the other hand, 330 and 160 nm spheres with uniaxial anisotropy show a sharp switching field and the shape of the hysteresis loop is more rectangular compared to the 800 nm spheres.

3. Micromagnetic finite element simulations reproduce the observed changes in the magnetization loops if the anisotropy is altered from a radial to an uniaxial type. Exchange energy, which favors the parallel alignment of the spins overcomes the radial anisotropy and leads to such parallel orientation of the moments upon decreasing the diameter of the sphere.

4. In addition to the change in the magnetic anisotropy, 330 and 160 nm spheres also exhibit a twisted magnetic state. Element selective hysteresis loops show that the Fe moments gradually tilt away from the field direction.

5. Nanospheres of the same diameter but with different thickness of Fe/Gd multilayers also show a dramatic change in the reversal mechanism. S-shaped hysteresis loop is seen on 800 nm spherules with 36 nm thick Fe/Gd film. Spherules of same diameter but with 54 nm thick Fe/Gd film exhibit a squared hysteresis loop with increased coercive field (H_c) by a factor of four. In contrast, only small variations can be seen on a flat substrate with respect to the increase in the thickness of the films. The interplay between the different anisotropy terms and the thickness dependent switching field on the spherules leads to such changes in the reversal mechanism. These results reveal the possibility of controlling the H_c of Fe/Gd system on the nanospheres, a capability that is promising for magneto-optical data storage.

6. Enhancement in the effective perpendicular magnetic anisotropy is seen by depositing in-plane magnetized Fe/Gd multilayers on nanospheres. A squared hysteresis is observed for the system deposited on silica nanospheres of 800, 330, and 160 nm in diameter, whereas the film on flat substrate manifests a hard axis hysteresis loop with higher saturation field. The change in the shape anisotropy of the magnetic film on the spherules is believed to be the source of the changes seen in the magnetization loops.

Chapter 6

Co/Pt multilayers on nanospheres

6.1 Properties

Co/Pt multilayer system is one of the promising candidates for perpendicular magnetic recording as explained in the chapter 1. Compared to Fe/Gd system Co/Pt exhibit very high perpendicular magnetic anisotropy (PMA), high remanent, and high coercivity. The perpendicular magnetic anisotropy (PMA) in Co/Pt multilayer system results from broken symmetries at the surface and interface of the film stack. The effective anisotropy, K_{eff}, is determined by the contributions of surface anisotropy , K_S, and a volume term, K_V, and can be approximated by $K_{eff} = K_V + 2K_S/t$. The volume term, K_V which depends on the shape anisotropy dominates with increasing Co layer thickness t, and favors an in-plane magnetization in the sample plane. As a consequence, at a critical Co layer thickness (t_{SRT}) a spin reorientation transition (SRT) where the direction of the magnetic easy axis rotates into the film plane occurs. Values of 0.3 - 1.7 nm have been reported for t_{SRT} [83, 154–157], depending on the Pt layer thickness [155], the crystal structure [83], the substrate [155], and the interfacial roughness [157]. Taking into account the gradient in the film thickness on the nanospheres, a SRT is expected locally on each sphere on depositing Co/Pt multilayers with $t > t_{SRT}$. The sample preparation and the micro magnetic simulations are done in colaboration with T. C. Ulbrich at the University of Konstanz. The results are published in references [158, 159].

6.2 Spin reorientation transition on nanospheres

A [Co(0.88 nm)/Pt(0.97 nm)]×8 multilayer stack is evaporated by molecular beam epitaxy (MBE) on an array of Polystyrene nanospheres of 720 nm diameter, self-assembled on a Si_3N_4 membrane. A base pressure of 2×10^{-10} mbar is used

and the growth of the system is assisted by a 2.9 nm thick Pt buffer. To prevent oxidation of the system, Pt of 0.97 nm thickness is used as a capping layer. A reference sample, deposited on a sapphire system exhibits an in-plane magnetic anisotropy as confirmed by SQUID measurements. The spin configuration and magnetization reversal is studied in a quantitative way with a lateral resolution of about 30 nm by scanning transmission x-ray microscopy (STXM) and compared with micromagnetic simulations.

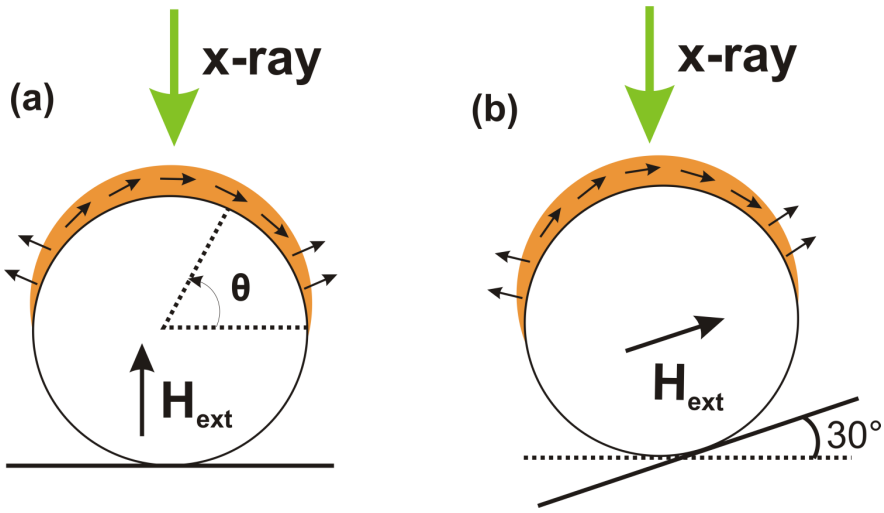

Figure 6.1: *Experimental configurations: (a) In the normal geometry, the illumination is perpendicular to the sample plane whereas (b) in the tilted configuration, the sample is rotated by 30°. Arrows on the caps sketch the orientation of the magnetic moments.*

Local magnetic properties of the sample were investigated by STXM. Magnetic contrast is obtained via x-ray magnetic circular dichroism (XMCD) as described in section 3.5.4. The x-ray energy was tuned to the Co L_3 absorption edge (778 eV), where XMCD gives a high magnetic contrast. Magnetization reversal of the sample is studied by applying both an in-plane and a perpendicular magnetic field. In the study of perpendicular field dependence, the sample is mounted at 90° to the x-ray direction as shown in Fig. 6.1 (a), whereas to probe the in-plane domains and the in-plane magnetic field dependence, the sample is mounted at an angle 30° as shown schematically in Fig. 6.1 (b).

6.2.1 Perpendicular magnetic field dependence

The STXM images in Fig. 6.2, obtained in normal geometry as sketched in Fig. 6.1 (a), show an array of the hexagonally packed spheres. At zero magnetic field, see Fig. 6.2 (a), all nanocaps are in a multi-domain state with dark and

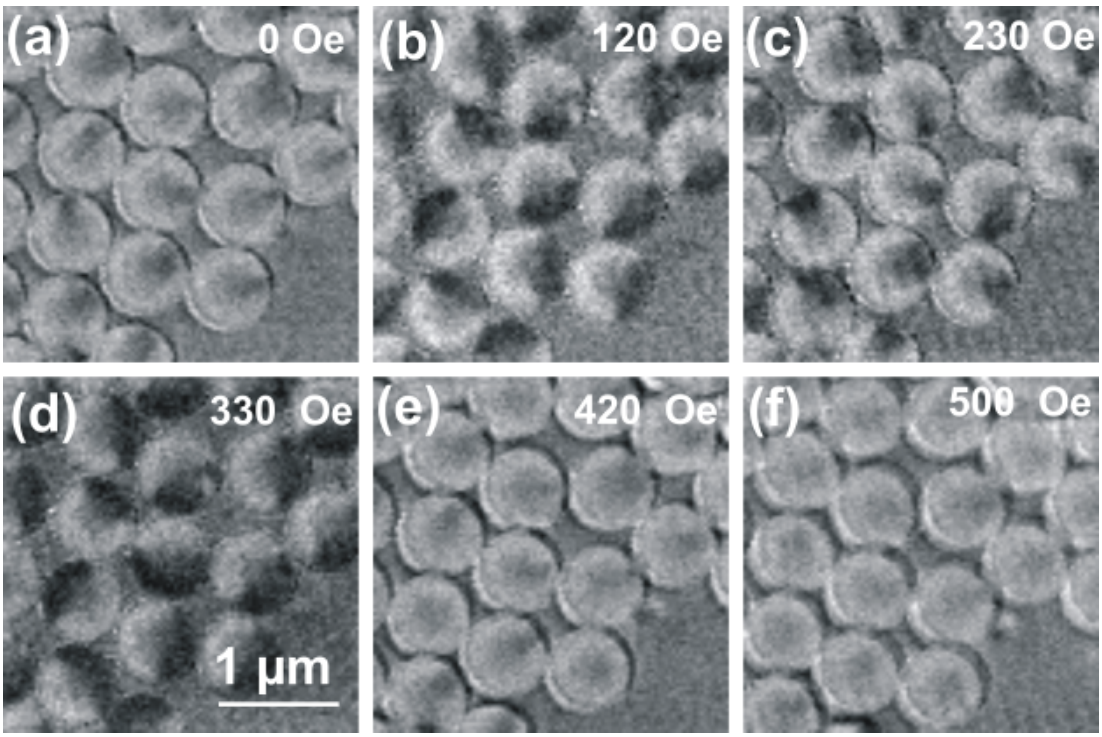

Figure 6.2: *STXM images recorded in normal geometry and at different perpendicular magnetic fields.*

light regions around the rim, whereas the center appears gray. These different contrast levels are consistent with the expected SRT behavior. The thinner film at the outer region of the cap ($\theta = 0°$ - $50°$) is anticipated to show an out-of-plane magnetization. Except for the very rim ($\theta = 0°$) these moments possess a non-vanishing projection onto the x-ray beam direction and thus provide XMCD contrast. Obviously, in all nanocaps both up and down magnetized domains exist, leading to the observed light and dark contrasts. In the center, where thickness t is high one expects an in-plane magnetization with a vanishing projection onto the x-ray beam and thus absence of XMCD contrast. Indeed, the gray circular area in the center of each cap confirms this expectation. In an applied perpendicular magnetic field H the light out-of-plane domains grow by domain wall motion azimuthally around the rim at the cost of the dark ones, as visible in Figs. 6.2 (b)-(e). At 500 Oe, see Fig. 6.2 (f), only light out-of-plane domains are visible. During this field scan, the contrast in the center area of the cap has not changed markedly. Even higher magnetic fields than available in our experiment are necessary to rotate these moments out of the film plane.

For a quantitative analysis the line scans of a single nanocap at different magnetic fields are recorded, see Fig. 6.3. At the rim of the sphere, i.e., for the angle ranges $\theta = 0°$ - $40°$ and $\theta = 140°$ - $180°$, the magnetization changes only

slightly with the azimuthal angle. This indicates a parallel orientation of magnetic moments, i.e., they point in the same direction instead of following the curvature of the sphere. With varying magnetic field distinct changes in the magnetic signal can be observed at the rim. As these magnetic moments are oriented under a large angle to the field, they experience a strong magnetic torque. Besides the domain wall motion, visible in the images of Fig. 6.2, a rotation of the moments out of the film plane is detectable as a continuous increase of contrast at higher magnetic fields. Moments in the center of the cap also show a change in the XMCD signal which is, however, lower than the one of the rim indicating a smaller angular excursion of the magnetization towards the field direction. By integrating the XMCD contrast in concentric rings within a single nanocap, as shown in the

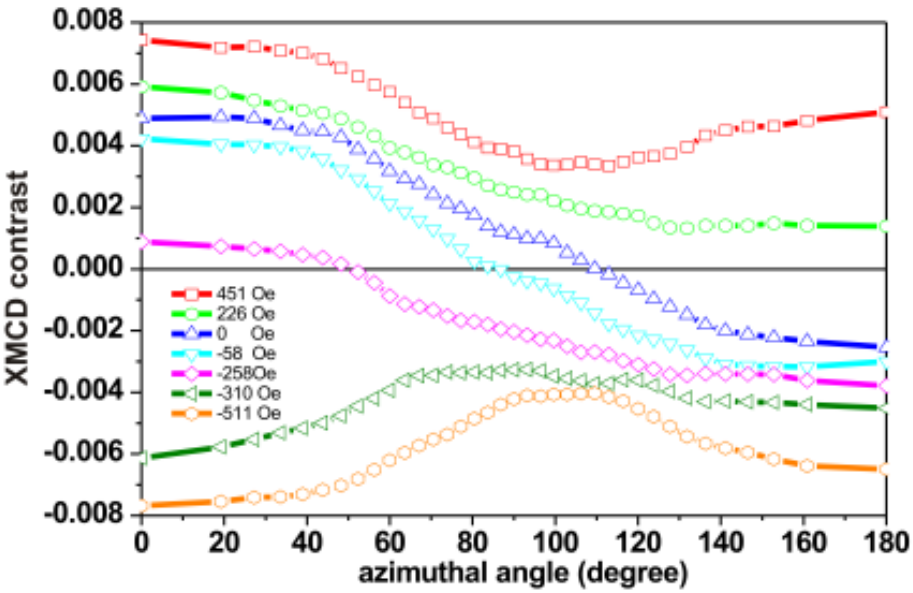

Figure 6.3: *Line scans through the center of a single nanocap recorded in different perpendicular magnetic fields. The signal at the rim changes strongly with the field indicating out-of-plane magnetization in contrast to the region in the center.*

inset of Fig. 6.4, local magnetization loops can be deduced as a function of the elevation. At low angles, $\theta = 0°$ - $56°$, sheered square magnetization loops are visible, indicating an easy-axis behavior. At high angles, $\theta = 70°$ - $90°$, the width of the loops and the magnitude of the signal at high magnetic fields decrease, which is typical for a hard-axis behavior. Thus, the easy axis changes from out-of-plane at the rim towards in-plane at the center of the nanocaps and the SRT can be located in the interval $56° < \theta < 70°$, i.e., within a spatial distance of less than 90 nm.

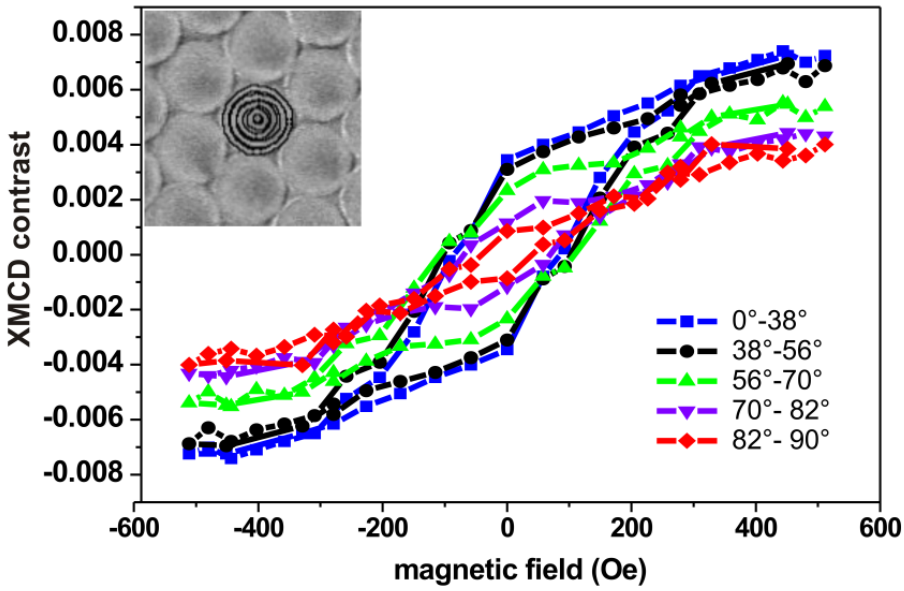

Figure 6.4: *Local magnetization loops. A single nanocap has been divided into concentric areas, as shown in the inset. The XMCD contrast, integrated in each of these intervals, is plotted as a function of the external magnetic field.*

6.2.2 In-plane magnetic field dependence

To complete the magnetization reversal analysis, an in-plane magnetic field using the geometry sketched in Fig. 6.1 (b) was applied. The STXM images of Fig. 6.5 show the domains of an individual cap and of the magnetic film on the surrounding flat substrate. To the left of the spherule in Fig. 6.5 (a) a circular region with a bright contrast is visible whereas the rest of the flat film shows a dark domain. Possibly, here the sphere caused a shadowing of the substrate during film deposition which results in a lower film thickness and thus altered the magnetic properties within the region marked as "AF area"in Fig. 6.5 (i). It should be emphasized that during the magnetization reversal the contrast of this circular region remains at nearly all magnetic fields opposite to the rest of the flat substrate, indicating an antiferromagnetic (AF) coupling due to dipolar interaction with the surrounding magnetic multilayer. The remanent states of the cap, see Figs. 6.5 (a) and (e), show again three different contrast levels that can be ascribed to the two out-of-plane domains at the rim and an in-plane region in the center. At 150 Oe, see Fig. 6.5 (b), switching of the magnetization occurs with a strong contrast in the inner, top region of the cap, indicating rotation of the moments out of the surface plane. In addition, a bright domain nucleates

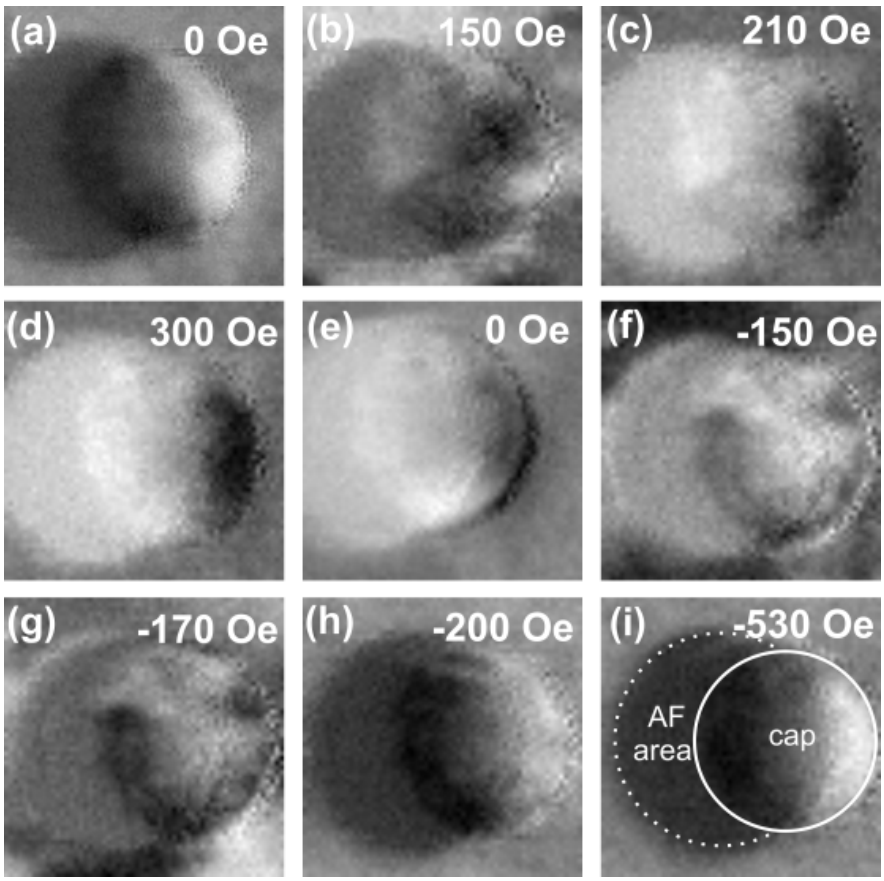

Figure 6.5: *Sequence of STXM images showing the magnetization reversal of an individual cap with 720 nm diameter and the surrounding magnetic film on the flat substrate at different magnetic fields applied in the sample plane.*

at the rim and moves around the rim on further increasing the field by domain wall motion. During the reversal cycle more than two out-of-plane domains can be observed, as presented in Figs. 6.5 (b)-(d). On changing the field direction, similar reversal mechanism with opposite magnetic contrast is seen (see Figs. 6.5 (f)-(i)).

Local hysteresis loop is deduced by integrating the XMCD contrast at the center of the sphere. A squared and well saturated hysteresis loop is seen in Fig. 6.6. Since the field is applied parallel to the sample plane, the in-plane region at the center of the cap undergoes magnetization reversal on applying an in-plane field resulting in a squared hysteresis. This behavior shows that at the center of the cap the magnetization lies in the plane of the film as compared to the region along the rim. In order to get more information about the reversal mechanism, a series of line scans are deduced from the images at different fields. At zero Oe a maximum XMCD signal (absolute value) is seen at $40° < \theta < 80°$ and $150° <$

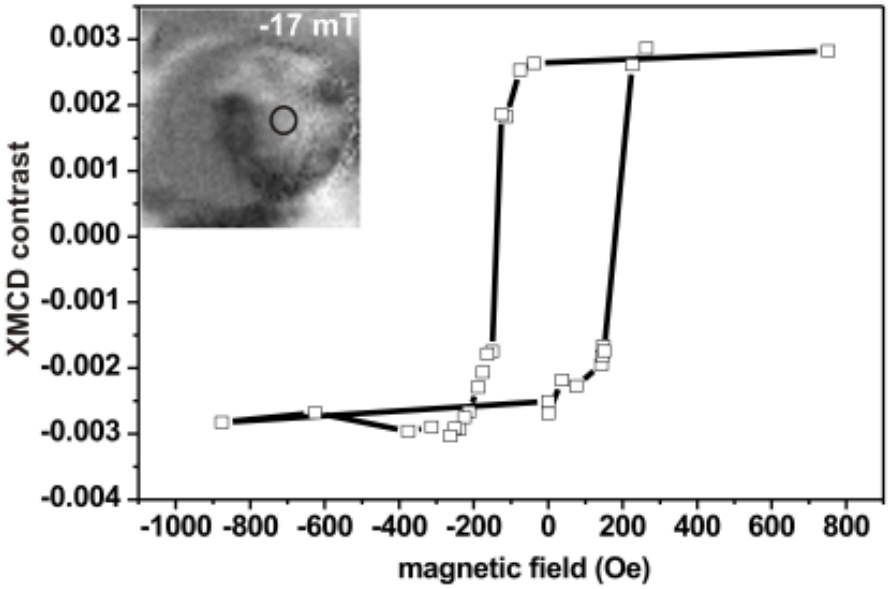

Figure 6.6: *Local magnetization loop. The XMCD contrast, integrated at the center of the cap, is plotted as a function of the external magnetic field applied parallel to the sample plane.*

$\theta < 180°$. This is due to the presence of two out-of-plane domains at the rim. At $80° < \theta < 150°$, the XMCD signal decreases with the increase of the azimuthal angle. The presence of vortex like in-plane domain at the center can lead to such continuous change in the magnetic contrast. Upon further increasing the field to 150 Oe, a decrease in the contrast level at the rim is observed. On the other hand the slope of the profile at the center ($80° < \theta < 150°$) becomes positive as compared to the one at zero Oe. At saturation the profile resembles the one at zero Oe with an opposite XMCD signal. These changes in the line profiles show that the magnetization reversal at the rim takes place by domain wall motion and at the center by a continuous rotation of magnetic moments.

6.2.3 Comparison with micro magnetic simulation

Micromagnetic simulations have been performed with software developed by T. Schrefl and D. Suess, using a mesh of finite elements with a maximum side length of 5 nm. The uniaxial out-of-plane anisotropy K_u of each cell is approximated by $K_u(t) = K_{uV} + 2K_{uS}/t$ = -0.13 MJm^{-3} + 1.5×10^{-10} MJm^{-2}/t for 0.3 nm $< t <$ 0.9 nm and $K_u(t)$ = const= 0.37 MJm^{-3} for $t <$ 0.3 nm with a local Co thickness of t = 0.9 nm sin(θ). The parameters K_{uV} and K_{uS} for the

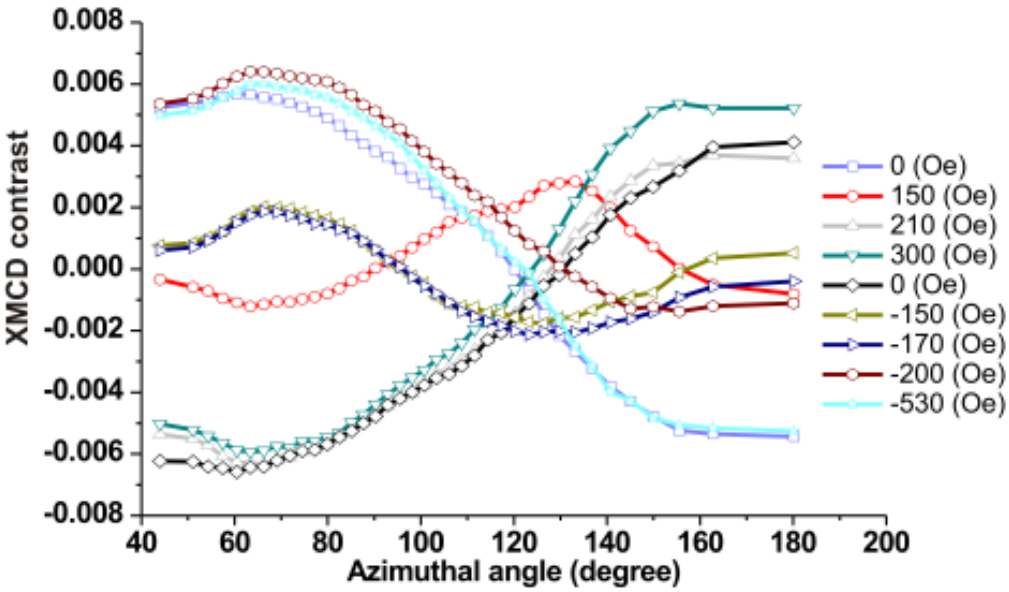

Figure 6.7: *Series of line scan through the center of a single sphere at different in-plane magnetic fields.*

volume and surface contributions of K_u, respectively, are deduced from SQUID measurements of flat films with a fixed Pt thickness of 0.8 nm and 0.2 nm $< t <$ 0.8 nm. For positive and negative values of the effective anisotropy including the shape anisotropy, its direction was set perpendicular or parallel, respectively, to the local surface of the sphere. The saturation magnetization M_s and the exchange stiffness A were assumed to be constant and set to $M_s = 0.5$ MA/m and A $= 1{\times}10^{-11}$ J/m, respectively.

Simulated spin configurations of an isolated cap at different in-plane magnetic fields are presented in Fig. 6.8. The color code scales with the projection of the magnetization onto a radial axis with 30° tilt, i.e., onto the direction of the x-ray beam in the experiment as sketched in Fig. 6.1 (b). Thus, the upper, top-view images can directly be compared to the STXM images of Fig. 6.5. The lower images present a side-view of the cap. Arrows indicate the direction of the magnetization. The remanent state, see Fig. 6.8 (a), consists of two out-of-plane domains at the rim and an in-plane magnetized domain in the center of the nanocap. A SRT at $\theta = 48°$ with a width of 70 nm is obtained in the simulation, which is in good agreement with Figs. 6.5 (a) and (e) of the experiment. During magnetization reversal, see Figs. 6.8 (b) and (c) more complicated domain structures are visible in accordance with Fig. 6.5 (b) and (f). While the central part reverses by a transition from a vortex to an onion state, the rim reverses by

domain wall motion. Despite the good overall agreement with the experimental results, some deviations are observed because thermal activation processes are neglected in the simulation, leading, e.g., to higher magnetic saturation fields.

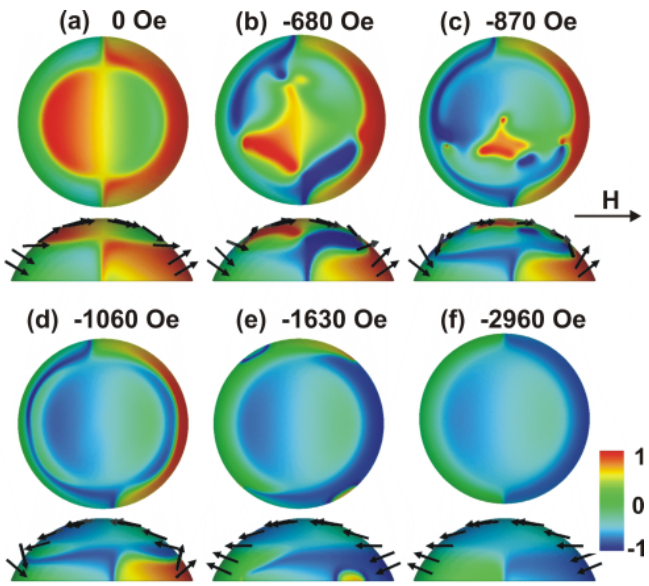

Figure 6.8: *Micromagnetic simulation of the spin configuration of a cap with 720 nm diameter in an in-plane magnetic field. The color code corresponds to the experimental XMCD contrast of Fig. 6.5. Magnetization vectors are shown in the lower side-view images.*

6.3 Conclusion

- The magnetic configuration of Co/ Pt multilayers deposited onto self-assembled arrays of spherical particles is studied by magnetic scanning transmission x-ray microscopy.
- Induced by the strong radial film thickness variation, a spin reorientation transition is detected within each single magnetic nanocap.
- Local hysteresis loops and magnetization profiles, providing quantitative insight into nanoscale magnetism, as well as micromagnetic simulations revealed that this SRT occurs within a distance of less than 90 nm.

Chapter 7

Summary and outlook

7.1 Summary

In this thesis, for the first time, Fe/Gd multilayers with monolayer and submonolayer thicknesses have been systematically studied on flat substrates and on self-assembled nanospheres with high spatial resolution. Magnetic transmission x-ray microscopy and photo emission electron microscopy in combination with SQUID, MOKE, TEM and XRD analysis have been used to characterize the sample. These systems are of special interest due to their adjustable low coercive fields (H_c) similar to that of Permalloy. The major difference which makes Fe/Gd systems very interesting for technical applications is the fact that they can be prepared with magnetization perpendicular to the film plane. In addition they generally show a low magnetization and external stray fields, but considerably high Kerr signal and spin density at the Fermi level, predominantly due to the Fe component. Furthermore, Fe/Gd systems also manifest thickness and temperature dependent spin reorientation transitions. All of these properties can be modified by the substrate structure produced by the self-assembled silica or polystyrene nanospheres. This provides a low-cost preparation technique capable of patterning large lateral areas. These systems have been studied in detail within this thesis.

Fe/Gd system on flat substrates

A series of Fe/Gd multilayers consisting of 75 bilayers have been prepared with sublayer thicknesses from 0.36 to 0.60 nm. A thickness dependent spin reorientation transition (SRT) from an in-plane to a perpendicularly magnetized state is observed by decreasing the sublayer thickness. These results are quantitatively explained by the contribution of the stray field and by the dipolar pair ordering model. From TEM analysis it has been seen that inhomogeneous interfaces cause an in-plane magnetization, whereas almost homogeneous interfaces lead to a perpendicular magnetic anisotropy (PMA). This is consistent with prior find-

ings where well mixed FeGd alloys manifest PMA. The layer thickness (total thickness), preparation techniques, and the choice of the substrate have a strong influence on magnetic properties of the system.

The domain configuration during a temperature driven SRT is studied in detail in case of a sample with the composition 75×[Fe (0.36 nm)/Gd (0.36 nm)]. It initially shows an in-plane magnetization at room temperature and upon heating the sample, the in-plane domains change to a maze like, perpendicular domains. Between these transformations, a coexistence of in-plane and out-of-plane domain configurations are seen in a broad temperature range of 57° - 81° C. Micromagnetic simulations reproduced a similar coexistence phase. The presence of two local minima in the total energy, due to the different temperature behaviors of the surface anisotropy (K_S) and the volume anisotropy (K_V) is believed to cause this coexistence phase. After several SRT cycles the perpendicular state of the sample became more prominent at room temperature. TEM images recorded before and after annealing show significant changes in the layered structure. This infers that the chemical and structural changes in the sample upon annealing are responsible for the appearance of PMA.

Fe/Gd system on nanospheres

By depositing Fe/Gd multilayers on self-assembled silica or polystyrene nanospheres a new class of magnetic nanostructures with a crescent shaped cross section are produced. The influence of the thickness gradient and the curved nature of the substrate on the properties of the magnetic multilayers are studied with respect to the diameter of the spheres and the thickness of the films.

A 36 nm Fe/Gd film with a composition of 50×[Fe (0.36 nm)/Gd (0.36 nm)] has been deposited on nanospheres with diameters of 800, 330, and 160 nm. Upon increasing the diameter of the spheres to 800 nm a dramatic change in the spin structure and the reversal mechanism is observed. Local hysteresis loops of the spherules, deduced from STXM images reveal an S-shaped loop for 800 nm spherules, while for the 330 and 160 nm spherules a squared loop with a sharp switching field accompanied by a change in the magnetic anisotropy from radial to uniaxial is observed. The exchange energy that favors the parallel alignment of the spins overcomes the radial anisotropy and leads to such parallel orientation of the moments upon decreasing the diameter of the sphere. The hysteresis loops and the reversal mechanism obtained by simulation are in good agreement with the experimental results. In addition, element selective hysteresis loops on 330 and 160 nm spherules show an asymmetric behavior at Fe and Gd edges. At the maximum field of about 400 Oe Gd moments align with the field direction, whereas Fe moments tilt away from the field direction. These changes suggest a twisted magnetic state due to the increase in the curvature and the magnetic field.

Furthermore, the thickness dependence of the magnetic properties is ad-

dressed. Spherules with a 36 nm thick Fe/Gd film, i.e. 50 bilayers, show an S-shaped loop. Spherules of same diameter of 800 nm but with 75 bilayers system show a squared loop with prominent steps and a strong increase in the coercive field by a factor of four. Magnetization reversal takes place through an intermediate flower state that shows up as a step in the hysteresis loop. This thickness dependent reversal mechanism is explained by the interplay between the different anisotropy terms and the thickness dependent switching field. Similar changes are not observed for the films deposited on a flat substrate.

A shape induced SRT is observed for an in-plane magnetized Fe/Gd film deposited on nanospheres. A hard axis loop is observed on a flat substrate, whereas the film on spherules with a diameter of 800 nm showed a rectangular easy axis loop. This is explained by the change in the shape anisotropy.

In addition, Co/Pt multilayer system is studied with high spatial resolution. This system is of great interest for high density magnetic recoding due to its high coercive field and saturation magnetization (M_s). The thickness gradient on the spheres is used to induce a thickness dependent SRT locally on every nanospheres. STXM images measured in an in-plane and an out-of-plane geometry reveal two different magnetic states at the rim and at the center of the spherules. Local hysteresis loops deduced on a ≈ 50 nm scale show a transformation of the magnetization curve from an easy axis loop to a hard axis loop with increasing the elevation angle on the spheres. The SRT from perpendicular to in-plane magnetization has been seen in the interval $56° < \theta < 70°$ within a distance of less than 90 nm. These results are in good agreement with micromagnetic simulations.

7.2 Outlook

Fe/Gd system on flat substrates

The prominent outstanding room-temperature properties of Fe/Gd multilayers with individual layer thicknesses close or even below the lattice constants of the corresponding bulk materials are adjustable perpendicular magnetic anisotropy, very small coercive fields, nearly vanishing magnetization and thus stray fields, and the occurrence of a spin reorientation transitions at room temperature. They make them excellent candidates for a variety of technical applications:

1. **Perpendicular GMR/TMR sensors**
   In recent years, the research activities on a perpendicular GMR or TMR elements with RE-TM systems as magnetic layers have gained momentum. In this context the Fe/Gd thin film system is one of the promising candidates for the soft magnetic layers in perpendicular GMR/TMR systems which show magnetoresisitive effects normally larger than conventional TMR elements that consist of a soft ferromagnetic film with in-plane magnetization like PY. When these materials are patterned into smaller elements a fluctuation of the switching field occurs due to inhomogeneous magnetization. In contrast, Fe/Gd thin films with very low saturation magnetization and coercive field but with a perpendicular magnetic anisotropy exhibit uniform magnetization even at smaller dimensions. Therefore these systems are very fascinating for GMR and TMR sensors.

2. **Heat assisted perpendicular magnetic recording (HAMR)**
   The high Kerr signal and the tunable thermal properties such as Curie temperature T_c or the compensation temperature T_{comp} makes Fe/Gd system also well suited for heat assisted perpendicular magnetic recording (HAMR). Systematic studies should be done to control the magnetic and transport properties precisely. The possibilities to tailor the magnetic properties by the composition, preparation condition and substrates are also very attractive aspects.

3. **Sensing layer for small perpendicular fields**
   Due to the possibility of very small perpendicular coercivity the studied Fe/Gd multilayers can effectively be used as sensor layers for small perpendicular fields. This is important for example in imaging the magnetic fields resulting from currents in high T_c superconductors, which these days are realized by hardly available, expensive garnet platelets [160]

In our department and world wide, the study of vortex core dynamics in the field of micromagnetism has recently gained strong interest. Applying a magnetic field pulse to a vortex structure causes gyrations of the core about its equilibrium

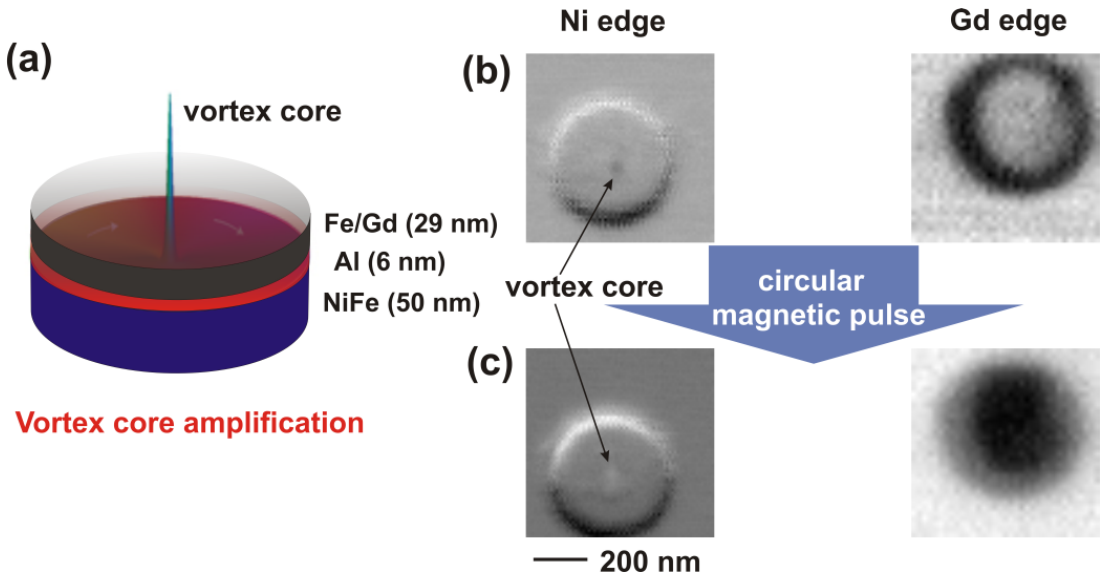

Figure 7.1: *(a) A schematic diagram of a Permalloy disc with vortex core and the amplifying perpendicular Fe/Gd multilayer imaged by STXM. STXM images taken at Ni and Gd edges before, (b), and after (c) applying a circular magnetic field. The switching of the Fe/Gd film due to the vortex core switching is clearly visible.*

position. The sense of gyration is determined by the vortex core polarization. Controlled switching of the vortex core have been reported [73, 161–163]. However, a remaining critical problem is the reading out of the magnetization direction of the vortex core. Because the core region has a width of only 10 - 20 nm, a very sensitive sensor is needed.

With the results and knowledge gained from the work of this thesis, we have chosen a Gd/Fe layer to image and amplify the perpendicular field of the vortex core [164]. Fig. 7.1 (a) shows a schematic diagram of a circular permalloy disk covered with an amplifying Fe/Gd system. Element selective STXM images of the stack are shown in Fig. 7.1 (b) and (c). Before applying a circular magnetic pulse a dark vortex core is seen at the Ni edge (Fig. 7.1 (b)) and a bright contrast is seen at Gd edge (Fig. 7.1 (b)). The polarization of the vortex core changes after applying a circular pulse (Fig. 7.1 (c) Ni edge) and consequently, the contrast at the Gd edges is also reversed (Fig. 7.1 (c) Gd edge). This infers that the magnetization direction of the Fe/Gd systems can be changed by switching the vortex core polarization. However, the coupling between the stacks and the switching dynamics have to be investigated in detail. Furthermore, we have shown that the magnification of the vortex core by the Fe/Gd sensor layer provides the possibility to study vortex core dynamics in a conventional Kerr microscope. Thus vortex core dynamics can be studied in a fast and effective manner in the laboratory in-house without the use of synchrotrons.

Fe/Gd system on nanospheres

Magnetic nanostructures produced by self-assembled nanospheres form an interesting playground for the fundamental studies of magnetism and open new doors for applications like patterned media and magnetic sensors. The bit size in the conventional magnetic storage media has already reached the dimension of about 25-30 nanometers. For a possible technological transfer from conventional magnetic recording techniques to a patterned media, regular arrays of magnetic nanostructures with dimension < 50 nm are necessary. In the self-assembly of nanospheres, long range ordering of smaller spheres has always been a hurdle. New innovative methods such as chemical surface modification [165], electrostatic potential and electrominuscous phenomena assisted self-assembly [166–168], self-assembly on pre-patterned substrates [169], and optical tweezers assisted self-assembly [170] may be carried out to improve the ordering. Since the reversal mechanism of magnetic spherules depends upon its diameter and the thickness of the film, a systematic study is necessary. The magnetic anisotropy and the coercive field of regular arrays of spherules with diameter < 50 nm have to be studied as a function of the film thickness of Fe/Gd system. As explained before, the vortex core polarization can be toggled by using a short burst of few ns [73]. By carefully tuning the H_c of the Fe/Gd system on the spherules, the field exerted from a vortex core polarization can be used to write bit information on an individual sphere. These studies may open new perspectives and insights for the application purposes.

Apart from magnetic recording, the investigated Fe/Gd multilayers on three dimensional substrates with individual dimensions in the micron and submicron range could be of interest for scanning microscopy techniques. Since the net magnetization of Fe/Gd system vanishes at the compensation temperature, by carefully tuning T_{comp} to ambient temperature, Fe/Gd systems can be used as a magnetic coating on a STM tip. Compared to conventional coatings, such unique system will provide a high spin density and a stray field free STM tip. Possible implementation can also have high impact on other scanning techniques like spin polarized scanning tunneling microscopy and spectroscopy (SP-STM/STS). A detailed study to tailor the T_{comp} has to be done.

Chapter 8

Zusammenfassung

In dieser Arbeit wurden zum ersten Mal Fe/Gd Multilagen mit Dicken im monoatomaren bis sub-monoatomaren Bereich systematisch auf flachen und selbstorganisierten Nanokugeln hochauflösend untersucht. Magnetische Transmissionsröntgenmikroskopie und Photoemissionselektronenmikroskopie in Kombination mit SQUID, MOKE, TEM und XRD Untersuchungen wurden für die Charakterisierung der Proben eingesetzt. Diese Systeme sind von besonderem Interesse durch ihr extrem kleines und regelbares Koerzitivfeld (H_c) (ähnlich wie Permalloy). Was das Fe/Gd System sehr interessant für technische Anwendungen macht ist jedoch die Tatsache, dass die Magnetisierung auch senkrecht zur Filmoberfläche stehen kann. Zusätzlich zeigen die Filme eine sehr kleine Magnetisierung und ein sehr kleines Feld, aber ein deutliches Kerrsignal und eine hohe Spindichte an der Fermikante, welche überwiegend durch das Eisen zustande kommt. Weiterhin zeigt das System einen dicken- und temperaturabhängigen Spinreorientierungsübergang. Diese Eigenschaften können zusätzlich durch die Struktur der Substrate modifiziert werden, welche aus selbstorganisierten Silica oder Polystyrolnanokugeln hergestellt wurden, die eine kostengünstige Präparationstechnik für die Stukturierung großer Flächen darstellen. Diese Systeme wurden in dieser Arbeit im Detail untersucht.

Fe/Gd auf flachen Substraten

In einer Serie von Fe/Gd Multilagen bestehend aus 75 Doppelschichten wurde die Teilschichtdicke zwischen 0.36 und 0.60 nm variiert. Ein dickenabhängiger Spinreorientierungsübergang (SRT) von einer in der Ebene liegenden Magnetisierung zu senkrechter Magnetisierung wurde bei einer Verkleinerung der Schichtdicke beobachtet. Diese Ergebnisse können quantitativ durch den Anteil des Streufeldes und durch das dipolare Paarordnungsmodell erklärt werden. In den TEM-Analysen konnte beobachtet werden, dass eine inhomogene Grenzfläche eine in der Ebene liegende Magnetisierung verursacht, wohingegen eine fast homogene Grenzschicht zu einer senkrechten magnetischen Anisotropie (PMA) führt. Dies stimmt mit

früheren Beobachtungen überein, in denen gut durchmischte FeGd Legierungen PMA Eigenschaften zeigen. Die Gesamtschichtdicke, Präparationstechnik und die Wahl des Substrats haben einen starken und justierbaren Einfluss auf die magnetischen Eigenschaften.

Im Falle einer Probe mit einem Aufbau von 75×[Fe (0.36 nm)/Gd (0.36 nm)] wurde die Domänenkonfiguration während eines temperaturgetriebenen SRT im Detail untersucht. Die Probe zeigte anfangs eine in-plane Magnetisierung bei Raumtemperatur. Während des Erhitzens der Probe veränderten sich die in-plane Domänen zu labyrinthähnlichen, senkrecht magnetisierten Streifendomänen.
In einem breiten Temperaturbereich von 57° - 81°C konnte eine Koexistenz der in-plane und senkrechten Domänenkonfiguration beobachtet werden. Mikromagnetische Simulationen reproduzieren dieses Ergebnis koexistierender Phasen. Eine Erklärung für diese Koexistenz beider Phasen könnte das Vorhandensein zweier lokaler Minima der totalen Energie aufgrund des unterschiedlichen Temperaturverhaltens der Oberflächenanisotropie (K_S) und der Volumenanisotropie (K_V) sein. Nach mehreren SRT-Zyklen dominierte bei Raumtemperatur der senkrechte Magnetisierungszustand. Aufgenommene TEM-Bilder vor und nach dem Anlassen zeigen eine deutliche Veränderung in der Schichtstruktur. Daraus folgt, dass die chemischen und strukturellen Änderungen in der Probe durch das Anlassen verantwortlich für den PMA-Effekt sind.

Fe/Gd auf Nanokugeln

Durch Auftragen der Fe/Gd Multilagen auf selbstorganisierte Silica- oder Polystyrolnanokugeln konnte eine neue Klasse von magnetischen Nanostrukturen mit einem sichelförmigen Querschnitt hergestellt werden.

Ein 36 nm dicker Fe/Gd Film mit einer Schichtstruktur von 50×[Fe (0.36 nm)/Gd (0.36 nm)] wurde auf Nanokugeln mit einem Durchmesser von 800, 330 und 160 nm aufgetragen. Bei einer Erhöhung des Kugeldurchmessers auf 800 nm wurde eine dramatische Änderung der Spinstruktur und des Ummagnetisierungsmechanismus beobachtet. Während die Hysteresekurven, die mittels STXM Messungen gewonnen wurden, im Falle der 800 nm Kugeln eine S-Form zeigen, ergeben sich für die Kugeln mit einem Durchmesser von 330 bzw. 160 nm rechteckige Hysteresekurven, was mit einer Änderung der Anisotropie von radial zu uniaxial einhergeht. Die Austauschenergie, welche minimal wird für eine parallele Ausrichtung der Spins, dominiert über die radiale Anisotropie und führt zu der parallelen Ausrichtung der Momente bei einer Reduktion der Kugeldurchmessers. Die mit Hilfe der Simulation gewonnenen Ergebnisse bezüglich der Hysteresekurve und des Ummagnetisierungsmechanismus zeigen eine gute Übereinstimmung mit dem Experiment. Darüber hinaus zeigen elementselektive Hystereskurven der 330 und 160 nm Kugeln ein asymmetrisches Verhalten an den Fe und Gd Kanten. Bei dem maximalen Feld von 400 Oe richten sich die Gd Momente in Feldrichtung aus, wohingegen die Fe Momente gegen die Feldrichtung verkippt

sind. Ursache hierfür ist der verkippte ("twisted") Magnetisierungzustand, der durch die Zunahme der Krümmung und bei hohem magnetischen Feld zustande kommt.

Auch hier wurde die Dickenabhängigkeit der magnetischen Eigenschaften untersucht. Kugeln, die mit einem 36 nm dicken Fe/Gd-Film (z. B. 50 Doppellagen) bedeckt sind, zeigten eine S-förmige Hysteresekurve. Kugeln mit demselben Durchmesser von 800 nm aber 75 Doppellagen zeigten dagegen eine rechteckige Hysteresekurve mit einem um einen Faktor vier größeren Koerzitivfeld. Das Schalten findet statt über einen Zwischenzustand (Flower-Zustand), welcher zu einer deutlichen Stufe in der Hysterese führt. Erklärt werden kann dies durch das Wechselspiel zwischen den verschiedenen Anisotropietermen und dem dickenabhängigen Schaltfeld. In den Filmen auf flachen Substraten konnten derartige Änderungen nicht beobachtet werden.

Eine forminduzierte SRT wurde für einen in-plane magnetisierten Fe/Gd Film auf Nanokugeln beobachtet. Während die Hysteresekurve beim flachen Substrat der magnetischen schweren Richtung zugeodnet werden kann, wurde für die Kugeln mit einem Durchmesser von 800 nm eine Hystereseschleife der magnetisch leichten Richtung beobachtet. Die Ergebnisse konnten mit Hilfe der Änderung der Formanisotropie erklärt werden.

Zusätzlich zu den Fe/Gd Proben wurden Co/Pt Multilagen mit hoher räumlicher Auflösung untersucht. Dieses System ist für die magnetische Speichertechnologie durch ihr hohes Koerzitivfeld und ihre hohe Sättigungsmagnetisierung (M_s) von großem Interesse. Der Dickengradient der Schicht auf der Kugel wurde dazu benutzt, lokal eine dickenabhängige SRT zu induzieren. Die STXM Aufnahmen in-plane- und out-of-plane-Geometrie zeigen zwei unterschiedliche magnetische Grundzustände am Rand und in der Kugelmitte. Mit zunehmendem Steigungswinkel ändern sich die Eigenschaften der Hysteresen kontinuierlich von einem Verhalten, welches der magnetisch schweren Richtung zugeordnet werden kann, zu einem der leichten Richtung entsprechenden Verhalten. Der Spinreorientierungsübergang von der senkrechten zur in-plane Magnetisierung wurde im Intervall von $56° < \theta < 70°$ mit einem Abstand von weniger als 90 nm beobachtet.

Appendix A

The Advanced Light Source

The Advanced Light Source (ALS), a division of Lawrence Berkeley national laboratory (LBNL), is a national user facility that generates intense light for scientific and technological research. It is one of the worlds brightest sources of ultraviolet and soft x-ray beams and the worlds first third-generation synchrotron light source in its energy range. The facility is funded by office of Basic Energy Sciences of the U.S. Department of Energy. Table A.1 lists the different storage ring parameters and the schematic diagram of the beam lines is shown in Fig. A.1.

Beam particle	electron
Beam energy	1.0-1.9 GeV
Injection energy	1.0-1.5 GeV
Beam current	400 mA in multibunch mode
	2 x 25 mA in two-bunch mode
Filling pattern (multibunch mode)	276-320 bunches
Bunch spacing: multibunch mode	2 ns
Bunch spacing: two-bunch mode	328 ns
Circumference	196.8 m
Number of straight sections	12
Radio frequency	499.642 MHz
Beam size in straight sections,	
rms (1.9 GeV multibunch mode)	310 microns horiz. x 16 microns vert.
Beam lifetime: multi bunch mode	8 hours 400 mA
Beam lifetime: two bunch mode	60 minutes 40 mA
Horizontal emittance	6.3 nm-rad
Vertical emittance	0.13 nm-rad
Energy spread (ΔE/E, rms)	1×10^{-3}

Table A.1: ALS storage ring parameters.

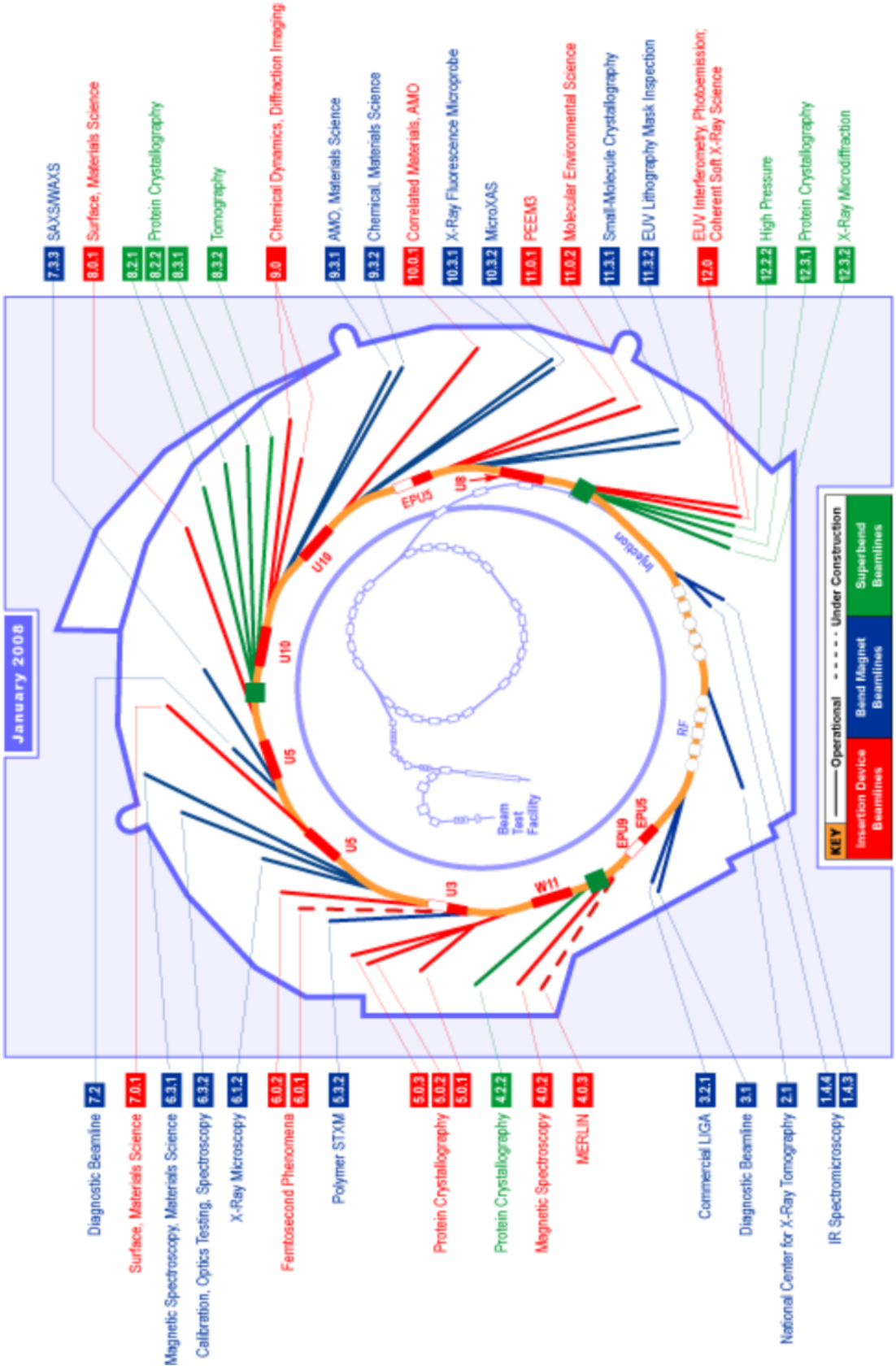

Figure A.1: *A schematic diagram of beamlines at ALS.*

A.1 Scanning transmission x-ray microscope at ALS

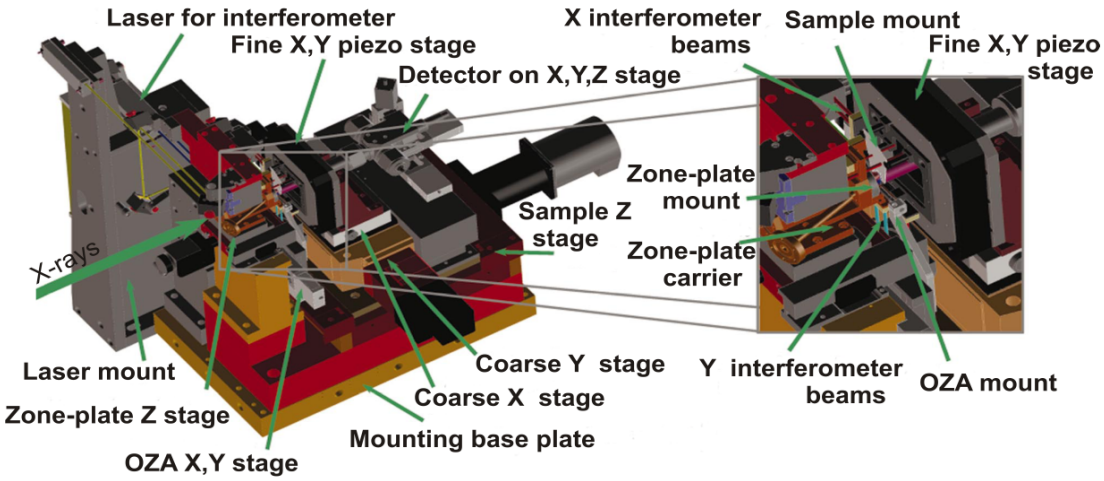

Figure A.2: *CAD diagram of STXM at ALS. X-rays from a elliptical undulator are focused by a zone plane lens onto the sample [70]. The sample is raster scanned by a piezo stage with a precession of a few nanometers. For course translation of the sample, another x, y, z stage controlled by stepper motors is used. The relative position of the sample stage and the zone plate lens is controlled by a laser interferometer. In order to increase the signal to noise ratio by suppressing unwanted diffraction, the zone plate is fabricated with a beam stop. In addition, a small pinhole, the order selection aperture (OSA) is placed between the sample and the zone plate to allow only the first diffraction order to pass. The spatial resolution depends on the numerical aperture (NA) of the zone plate. The transmitted photon intensity is detected by a photomultiplier or by an avalanche photo diode (APD) [70].*

A.2 X-ray photoemission electron microscope at ALS

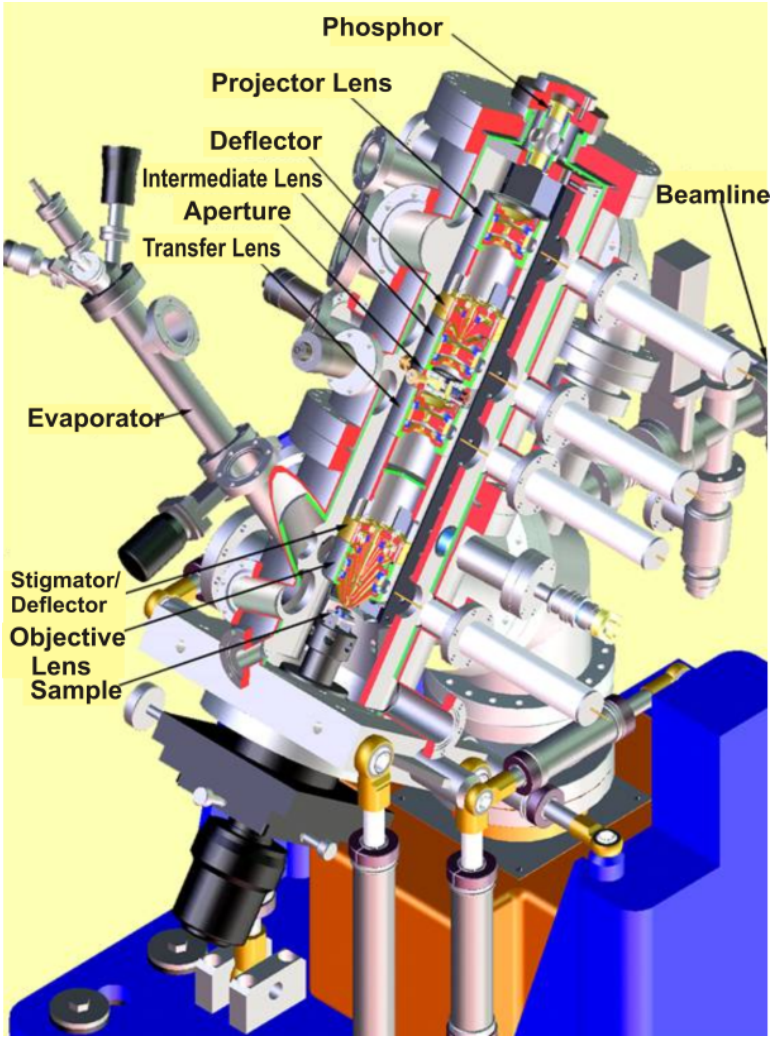

Figure A.3: *CAD diagram of X-PEEM at ALS. The microscope spatially resolves and images the secondary electrons emitted from a sample upon illumination with X-rays. Four electrostatic lenses are used for focusing and projection of the electrons. The electrons are accelerated by a strong electric field (≈20 kV) between sample and the objective lens of the microscope. After a magnification by a factor of 1000-2000, the electrons hit a phosphor screen which is detected by a CCD (charge coupled device) camera. An aperture in the back focal plane of the second lens (transfer lens) is used to reduce the spherical and chromatic aberrations of the electron optics. The typical spatial resolution for magnetic imaging is about 50 to 100 nm. In addition, deflector and stigmator elements located in the back focal plane of the objective lens and the first projection lens are used to correct for small mechanical misalignments of the microscope [77].*

Appendix B

Curriculum vitae

20.07.1980	Born in Thachambady, Tamil Nadu, India
1984-1994	Primary and middle school, Cluny convent, Devikapuram
1994-1996	High school, St.Joseph's School, Susainagar
1996-1998	Higher secondary school, St.Joseph's School, Susainagar
1999-2002	Bachelor degree in Physics (B.Sc), Loyola College, Chennai
2002-2004	Master degree in Physics (M.Sc), University of Stuttgart, Germany
December 2004	Master thesis under the guidance of Prof. Dr. H. D. Carstanjen: *Investigation of oxide layers in tunnel junctions* Max-Planck-Institute for Metals Research, Stuttgart
Since January 2005	PhD student in Department Prof. Dr. G. Schütz at Max-Planck-Institute for Metals Research, Stuttgart

Appendix C

List of publications

1. S. Bedanta, T. Eimüller, W. Kleemann, J. Rhensius, F. Stromberg, **E. Amaladass**, S. Cardoso, and P. P. Freitas : *Overcoming the dipolar disorder in dense CoFe nanoparticle ensembles: Superferromagnetism*, Phys. Rev. Lett. **98**, 176601 (2007)

2. **E. Amaladass**, B. Ludescher, G. Schütz, T. Tyliszczak, and T. Eimüller : *Size dependence in the magnetization reversal of Fe/Gd multilayers on self-assembled arrays of nanospheres*, Appl. Phys. Lett **91**, 172514 (2007)

3. T. Eimüller, T. C. Ulbrich, **E. Amaladass**, I. L. Guhr, T. Tyliszczak, and M. Albrecht : *Spin-reorientation transition in Co/Pt multilayers on nanospheres*, Phys. Rev. B. **77**, 134415 (2008)

Contributions to non-refereed journals

1. **E. Amaladass**, B. Ludescher, G. Schütz, T. Tyliszczak, and T. Eimüller: *"Nano-balls" for magnetic data memories: Accurate and in expensive*, Focus on materials, Max Planck institute for metals research stuttgart, issue 4 February 2007

To be published

1. T. Eimüller, **E. Amaladass**, B. Ludescher : *Coexistence of in-plane and out-of-plane domains during continuous reverse spin reorientation in an Fe/Gd multilayer*

2. **E. Amaladass**, B. Ludescher, G. Schütz, T. Tyliszczak, and T. Eimüller: *Thickness dependence in the magnetization reversal of Fe/Gd multilayers on self-assembled arrays of nanospheres*

3. **E. Amaladass**, B. Ludescher, G. Schütz, T. Tyliszczak, and T. Eimüller: *Strong increase in the effective perpendicular magnetic anisotropy by depositing thin films on nanospheres*

4. T. Eimüller, M. S. Lee, **E. Amaladass**, L. Feng, and T. Tyliszczak: *Element selective measurement of magnetization loops on a 20 nm scale*

List of Figures

List of Tables

Bibliography

[1] J. F. Bobo, L. Gabillet, and M. Bibes: *Recent advances in nanomagnetism and spin electronics*, J. Phys. Condens. Matter. **16**, 471 (2004)

[2] G. Sarjer, L. H. Lewis, S. D. Bader, A. J. Epstein, C. S. Fadley, E. E. Fullerton, A. Hoffmann, J. B. Kortright, Kannan M. Krishnan, S. A. Majetich, T. S. Rahman, C. A. Ross, M. B. Salamon, I. K. Schuller, T. C. Schulthess, and J. Z. Sun: *Advances in nanomagnetism via X-ray techniques*, J. Magn. Magn. Mater. **307**, 1 (2006)

[3] G. Binasch, P. Grünberg, F. Saurenbach, and W. Zinn: *Enhanced magnetoresistance in layered magnetic structures with antiferromagnetic interlayer exchange*, Phys. Rev. B. **39**, 4828 (1989)

[4] M. N. Baibich, J. M. Broto, A. Fert, F. Nguyen van Dau, F. Petroff, P. Eitenne, G. Creuzet, A. Friederich, and J. Chazelas: *Giant magnetoresistance of (001)Fe/(001)Cr magnetic superlattices*, Phys. Rev. Lett. **61**, 2472 (1988)

[5] S. S. P. Parkin: *Systematic variation of the strength and oscillation period of indirect magnetic exchange coupling through the 3d, 4d, and 5d transition metals*, Phys. Rev. Lett. **67**, 3598 (1991)

[6] B. Dieny, V. S. Speriosu, S. S. P. Parkin, and B. A. Gurney: *Giant magnetoresistance in soft ferromagnetic multilayers*, Phys. Rev. B. **43**, 1297 (1991)

[7] D. E. Heim, R. E. Fontana, C. Tsang, and V. S. Speriosu: *Design and operation of spin-valve sensors*, IEEE Trans. on Magn. **30**, 316 (1994)

[8] M. Julliere: *Tunneling between ferromagnetic films*, Phys. Lett. A. **54**, 225 (1975)

[9] W. J. Gallagher, and S. S. P. Parkin: *Development of the magnetic tunnel junction MRAM at IBM: From first junctions to a 16-Mb MRAM demonstrator chip*, IBM J. RES. and DEV. **50**, 5 (2006)

[10] D. A. Thompson, and J. S. Best: *The future of magnetic data storage technology*, IBM J. Res. Develop. **44**, 3 (2000)

[11] C. Chappert, A. Fert, and F. Nguyen Van Dau: *The emergence of spin electronics in data storage*, Nat. Mater. **6**, 813 (2007)

[12] www.nobelprize.org, *The Royal Swedish Academy of Sciences*, Press Release (9 October 2007)

[13] G. A. Prinz: *Magnetoelectronics*, Science **282** 1660 (1998)

[14] W. Kohn, and L. J. Sham: *Self-consistent equations including exchange and correlation effects*, Phys. Rev. **140**, A1133 (1965)

[15] A. Zunger: *Spin-dependent correlated atomic pseudopotentials*, Phys. Rev. B. **22**, 649 (1980)

[16] J. B. Kortright, D. D. Awschalom, J. Stöhr, S. D. Bader, Y. U. Idzerda, S. S. P. Parkin, Ivan K. Schuller, and H. C. Siegmann: *Research frontiers in magnetic materials at soft X-ray synchrotron radiation facilities*, J. Magn. Magn. Mater. **207**, 7 (1999)

[17] O. Pietzsch, A. Kubetzka, M. Bode, and R. Wiesendanger: *Observation of magnetic hysteresis at the nano-scale by spin polarized scanning tunneling spectroscopy*, Science **292**, 2053 (2001)

[18] F. Meier, L. Zhou, J. Wiebe, and R. Wiesendanger: *Revealing magnetic tnteractions from single-atom magnetization curves*, Science **320**, 82 (2008)

[19] B. D. Terris, H. J. Mamin, D. Rugar, W. R. Studenmund, and G. S. Kino: *Near-field optical data storage using a solid immersion lens* Appl. Phys. Lett. **65**, 388 (1994)

[20] X. Zhang, and Z. Liu: *Superlenses to overcome the diffraction limit*, Nat. Mater. **7**, 435 (2008)

[21] D. Weller, and A. Moser: *Thermal effect limits in ultrahigh-density magnetic recording*, IEEE Trans. Magn. **35**, 4423 (1999)

[22] S. Iwasaki, and K. Takemura: *An analysis for the magnetization mode for high density magnetic recording*, IEEE Trans. Magn. **11**, 1173 (1975)

[23] S. Iwasaki, and Y. Nakamura: *The magnetic field distribution of a perpendicular recording head* IEEE Trans. Magn. **14**, 436 (1978)

[24] S. N. Piramanayagam: *Perpendicular recording media for hard disk drives*, J. Appl. Phy. **102**, 011301 (2007)

[25] D. Jeanniot, and J. Desserre: *A transition-metal-rare-earth alloy for perpendicular magnetic recording*, J. Appl. Phys. **54**, 2820 (1983)

[26] P. Berstein, and F. Rio: *Properties of amorphous TbFe thin films for perpendicular recording*, IEEE Trans. Magn. Mag. **23**, 143 (1987)

[27] K. Matsumoto: *Perpendicular magnetic recording using magneto-optical media*, FUJITSU Sci.Tech. J. **37**, 155 (2001)

[28] D. Litvinov, and S. Khizroev: *Perpendicular magnetic recording: Playback*, J. Appl. Phys. **97**, 071101 (2005)

[29] S. Khizroev, and D. Litvinov: *Perpendicular magnetic recording: Writing process*, J. Appl. Phys. **95**, 4521 (2004)

[30] C. A. Ross: *Patterned recording magnetic media*, Annu. Rev. Mater. Res. **31**, 203 (2001)

[31] J. U. Thiele, S. Maat, and E. Fullerton: *FeRh/FePt exchange spring films for thermally assisted magnetic recording media*, Appl. Phys. Lett. **82**, 2859 (2003)

[32] Y. C. Wu, and C. H. Lai: *Reducing the writing temperature of thermal assisted media by controlling the composition of FePt*, IEEE Trans. Magn. **43**, 2 (2007)

[33] J. I. Martin, J. Nogues, K. Liu, J. L. Vicent, and I. K. Schuller: *Ordered magnetic nanostructures:fabrication and properties*, J. Magn. Magn. Mater. **256**, 449 (2003)

[34] P. B. Fischer, and S. Y. Chou: *10 nm electron beam lithography and sub-50 nm overlay using a modified scanning electron microscope*, Appl. Phys. Lett. **62**, 2989 (1993)

[35] M. Schneider, H. Hoffmann, and J. Zweck: *Lorentz microscopy of circular ferromagnetic permalloy nanodisks*, Appl.Phys. Lett. **77**, 2909 (2000)

[36] J. P. Silverman: *X-ray lithography: Status, challenges, and outlook for 0.13 μm*, J. Vac. Sci. Technol. B. **15**, 2117 (1997)

[37] M. Farhoud, H. I. Smith, M. Hwang, and C. A. Ross: *The effect of aspect ratio on the magnetic anisotropy of particle arrays*, J. Appl.Phys. **87**, 5120 (2000)

[38] S. Sun, C. B. Murray, D. Weller, L. Folks, and A. Moser: *Monodisperse FePt nanoparticles and ferromagnetic FePt nanocrystal superlattices*, Science **287**, 1989 (2000)

[39] A. Ethirajan, U. Wiedwald, H. G. Boyen, B. Kern, L. Han, A. Klimmer, F. Weigl, G. Kästle, P. Ziemann, K. Fauth, G. Schütz, C. Jun, R. J. Behm, M. Büttner, A. Romanyuk, P. Oelhafen, P. Walther, J. Biskupek, and U. Kaiser: *A micellar approach to magnetic ultrahigh-density data-storage media: Extending the limits of current colloidal methods*, Adv. Mater. **19**, 406 (2007)

[40] M. Saito, M. Kirihara, T. Taniguchi, and M. Miyagi: *Micropolarizer made of the anodized alumina film*, Appl. Phys. Lett. **55**, 607 (1989)

[41] J. C. Hulteen, P. Van Duyne: *Nanosphere lithography: A materials general fabrication process for periodic particle array surfaces*, J. Vac. Sci. Technol. A. **13**, 1553 (1995)

[42] M. Albrecht, G. Hu, I. L. Guhr, T. C. Ulbrich, J. Boneberg, P. Leiderer, and G. Schatz: *Magnetic multilayers on nanospheres* Nat. Mater. **4**, 203 (2005)

[43] P. Fischer, T. Eimüller, G. Schütz, P. Guttmann, G. Schmahl, K. Prügl, and G. Bayreuther: *Imaging of magnetic domains by transmission X-ray microscopy*, J. Phys. D: Appl. Physics **31**, 649 (1998)

[44] T. Eimüller, R. Kalchgruber, P. Fischer, G. Schütz, P. Guttmann, G. Schmahl, M. Köhler, K. Prügl, M. Scholz, F. Bammes, and G. Bayreuther: *Quantitative imaging of magnetization reversal in Fe/Gd multilayers by magnetic transmission x-ray microscopy*, J. Appl. Phys. **87**, 6478 (2000)

[45] T. Eimüller, M. Scholz, P. Guttmann, P. Fischer, M. Köhler, G. Bayreuther, G. Schmahl, and G. Schütz: *Magnetization reversal of a multilayered FeGd dot array imaged by transmission x-ray microscopy*, J. Appl. Phys. **89**, 7162 (2001)

[46] T. Eimüller, M. Scholz, P. Guttmann, P. Fischer, M. Köhler, G. Bayreuther, G. Schmahl, and G. Schütz: *Undulation instabilities in laterally structured magnetic multilayers*, J. Appl. Phys. **91**, 7334 (2002)

[47] T. Eimüller: *Magnetic imaging of nanostructured systems with transmission x-ray microscopy*, Ph.D. thesis, University of Würzburg, (2002)

[48] L. D. Landau, and E. M. Lifshitz: *On the theory of the dispersion of magnetic permeability in ferromagnetic bodies*, Phys.Z. Sowjetunion **8**, 153 (1935)

[49] A. Hubert, and R. Schäfer: *Magnetic Domain: The Analysis of Magnetic Microstructures*, (Springer, Heidelberg 1998)

[50] J. Stöhr, H. C. Siegmann: *Magnetism from fundamentals to nanoscale dynamics*, (Springer, Heidelberg 2006)

[51] P. Bruno: *Tight-binding approach to the orbital magnetic moment and magnetocrystalline anisotropy of transition-metal monolayers*, Phys. Rev. B. **39**, 865 (1989)

[52] G. Bertotti: *Hysteresis in Magnetism: For physicists, Materials scientists, and Engineers*, (Acadamic press, CA USA, 1998)

[53] B. A. Lilley: *Energies and widths of domain boundaries in ferromagnetics*, Phi. Mag. (7)**41**, 792 (1950)

[54] W. Scholz, J. Fidler, T. Schrefl, D. Suess, R. Dittrich, H. Foster, and V. Tsiantos: *Scalable parallel micromagnetic solvers for magnetic nanostructures*, Comp. Mat. Sci. **28**, 366 (2003)

[55] http://gid.cimne.upc.es/

[56] http://www.hpfem.jku.at/netgen/

[57] http://www.paraview.org/New/index.html

[58] http://www.kgt.co.jp/english/product/avs/mavs/index.html

[59] J. Als-Nielsen, and D. McMorrow; *Elements of Modern X-Ray Physics* (Wiley, Chichester, 2001)

[60] D. B. Williams, and C. B. Carter: *Transmission electron microscopy; A textbook for material science*,(Plenum press, New York)

[61] http://www.microscopy.ethz.ch/TEM.htm

[62] D. A. Allwood, Gang Xiong, M. D. Cooke, and E. P. Cowborn: *Magneto-optical Kerr effect analysis of magnetic nanostructures*, J. Phys. D: Appl. Phys. **36**, 2175 (2003)

[63] S. G. Glück, Dilomarbeit, Julius-Maximilians-Universität Würzburg, (1999)

[64] M. P. Augustine, D. M. TonThat, and J. Clarke: *SQUID detected NMR and NQR*, Solid. State. Nucl. Mag. **11**, 139 (1998)

[65] H. Ebert: *Magneto-optical effects in transition metal systems*, Rep. Prog. Phys. **59**, 1665 (1996)

[66] D. Attwood: *Soft x-rays and extreme ultraviolet radiation: principles and application*, (Cambridge university press)

[67] G. Schütz, W. Wagner, W. Wilhelm, P. Kienle, R. Zeller, R. Frahm, and G. Materlik: *Absorption of circularly polarized x rays in iron*, Phys. Rev. Lett. **58**, 737 (1987)

[68] C. T. Chen, F. Sette, Y. Ma, and S. Modesti: *Soft x-ray magnetic circular dichroism at the $L_{2,3}$ edges of nickel*, Phys.Rev. B, **43**, 7262 (1990)

[69] C. T. Chen, N. V. Smith, and F. Sette: *Exchange, spin-orbit, and correlation effects in the soft-x-ray magnetic-circular-dichroism spectrum of nickel*, Phys.Rev. B. **43**, 6785 (1991)

[70] A. L. D. Kilcoyne, T. Tyliszczakc, W. F. Steele, S. Fakra, P. Hitchcock, K. Franck, E. Anderson, B. Harteneck, E. G. Rightor, G. E. Mitchell, A. P. Hitchcock, L. Yang, T. Warwickc, and H. Adea: *Interferometer-controlled scanning transmission X-ray microscopes at the Advanced Light Source*, J. Synchrotron Rad. **10**, 125 (2003)

[71] W. Chao, B. D. Harteneck, J. A. Liddle, E. H. Anderson, and D. T. Attwood: *Soft X-ray microscopy at a spatial resolution better than 15 nm*, Nature **435**, 1210 (2005)

[72] Y. Acremann, J. P. Strachan, V. Chembrolu, S. D. Andrews, T. Tyliszczak, J. A. Katine, M. J. Carey, B. M. Clemens, H. C. Siegmann, and J. Stöhr: *Time-resolved imaging of spin transfer switching: Beyond the macrospin concept*, Phys. Rev. Lett. **96**, 2172021 (2006)

[73] B. Van Waeyenberge, A. Puzic, H. Stoll, K. W. Chou, T. Tyliszczak, R. Hertel, M. Fähnle, H. Brückl, K. Rott, G. Reiss, I. Neudecker, D. Weiss, C. H. Back, and G. Schütz : *Magnetic vortex core reversal by excitation with short bursts of an alternating field*, Nature **444**, 461(2006)

[74] http://rsb.info.nih.gov/ij/

[75] http://xraysweb.lbl.gov/peem2/webpage/Tools.shtml

[76] http://unicorn.mcmaster.ca/aXis2000.html

[77] S. Anders, H. A. Padmore, R. M. Duarte, T. Renner, T. Stammler, A. Scholl, M. R. Scheinfein, and J. Stöhr: *Photoemission electron microscope for the study of magnetic materials*, Rev. Sci. Instrum. **70**, 3973 (1999)

[78] A. Scholl, H. Ohldag, F. Nolting, and J. Stöhr: *X-ray photoemission electron microscopy, a tool for the investigation of complex magnetic structures*, Rev. Sci. Instrum. **73**, 1362 (2002)

[79] Z. S. Shan, D. J. Sellmyer, S. S. Jaswal, Y. J. Wang, and J. X. Shen: *Magnetism of rare-earthtransition-metal nanoscale multilayers. II. Theoretical analysis of magnetization and perpendicular magnetic anisotropy*, Phys. Rev. B. **42**, 10446 (1990)

[80] S. Honda, M. Nawate, and I. Sakamoto: *Magnetic structure and perpendicular magnetic anisotropy of rare-earth (Nd,Pr,Gd)/Fe multilayers*, J. Appl. Phys. **79**, 365 (1996)

[81] T. Schmidt, and H. Hoffmann: *Magnetic properties of Ni/Tb multilayers*, J. Magn. Magn. Mater. **257**, 22 (2003)

[82] F. J. A. den Broeder, W. Hoving, and P. J. H. Bloemen: *Magnetic anisotropy of multilayers*, J. Magn. Magn. Mater. **93**, 562 (1991)

[83] B. N. Engel, C. D. England, R. A. Van Leeuwen, M. H. Wiedmann, and C. M. Falco: *Interface magnetic anisotropy in epitaxial superlattices*, Phys. Rev. Lett. **67**, 1910 (1991)

[84] J. I. Hong, S. Sankar, A. E. Berkowitz, and W. F. Egelhoff: *On the perpendicular anisotropy of Co/Pd multilayers*, J. Magn. Magn. Mater. **285**, 359 (2005)

[85] S. T. Purcell, M. T. Johnson, N. W. E. McGee, W. B. Zeper, and W. Hoving: *Spatially resolved magneto-optical investigation of the perpendicular anisotropy in a wedge-shaped ultrathin epitaxial Co layer on Pd(111)* J. Magn. Magn. Mater. **113**, 257 (1992)

[86] M. T. Johnson, P. J. H. Bloemen, F. J. A. den Broeder, and J. J. de Vries: *Magnetic anisotropy in metallic multilayers*, Rep. Prog. Phys. **59**, 1409 (1996)

[87] C. H. Lee, R. F. C. Farrow, C. J. Lin, E. E. Marinero, and C. J. Chien: *Molecular-beam-eptaxial growth and magnetic properties of Co-Pt superlattices oriented on the [001],[110] and [111] axes of Pt*, Phys. Rev. B. **42**, 11384 (1990)

[88] W. B. Zeper, J. A. M Greidanus, P. F. Carcia, and C. R. Fincher: *Perpendicular magnetic anisotropy and magnet-optical Kerr effect of vapor-deposited Co/Pt layered structures*, J. Appl. Phys. **65**, 4871 (1989)

[89] J. Velev, and Y. C. Chang: *Perpendicular giant magnetoresistance in Fe/Cr nanowires*, J. Magn. Magn. Mater. **250**, 219 (2002)

[90] U. K. Roessler, and A. N. Bogdanov: *Reorientation in Antiferromagnetic Multilayers: Spin-Flop Transition and Surface Effects* , arXiv:cond-mat/0406412v1 [cond-mat.mtrl-sci]

[91] G. Garreau, S. Hajjar, J. L. Bubendorff, C. Pirri, D. Berling, A. Mehdaoui, R. Stephan, P. Wetzel, S. Zabrocki, G. Gewinner, S. Boukari, and E. Beaurepaire: *Growth and magnetic anisotropy of Fe films deposited on Si(111) using an ultrathin iron silicide template*, Phys. Rev. B. **71**, 094430 (2005)

[92] T. Sato, T. Goto, H. Ogata, K. Yamaguchi, and H. Yoshida, H: *Perpendicular magnetic anisotropy of (Co, Fe)/Pt multilayers*, J. Magn. Magn. Mater. **272**, E951 (2004)

[93] J. Sticht and J. Kübler: *Electronic structure of ferromagnetic Gd*, Sol. Stat. Comm. **53**, 529 (1985)

[94] R. E. Camley: *Surface spin reorientation in thin Gd films on Fe in an applied magnetic field*, Phys. Rev. B, **35**, 3608 (1987)

[95] R. E. Camley, and D. R. Tilley: *Phase transitions in magnetic superlattices*, Phys. Rev. B. **37**, 3413 (1988)

[96] K. Cherifi, C. Dufour, Ph. Bauer, G. Marchal, and Ph. Mangin: *Experimental magnetic phase diagram of a Gd/Fe multilayered ferrimagnet*, Phys. Rev. B. **44**, 7733 (1991)

[97] W. Hahn, M. Loewenhaupt, Y. Y. Huang, G. P. Felcher, and S. S. P. Parkin: *Experimental determination of the magnetic phase diagram of Gd/Fe multilayers*, Phys. Rev. B. **52**, 16041 (1995)

[98] K. H. J. Buschow: *Handbook of magnetic materials* (Elsevier science publishers, Amsterdam, The Netherlands, 1991), Chap. 4, p. 362

[99] M. Taborelli, R. Allenspach, G. Boffa, and M. Landolt: *Magnetic coupling of surface adlayers: Gd on Fe(100)*, Phys. Rev. Lett. **56**, 2869 (1986)

[100] R. E. Camley: *Properties of magnetic superlattices with antiferromagnetic interfacial coupling: Magnetization, susceptibility, and compensation points*, Phys. Rev. B. **39**, 12316 (1989)

[101] R. J Gambino, and J. J. Cuomo: *Selective resputtering-induced anisotropy in amorphous films*, J. Vac. Sci. Technol. **15**, 296 (1978)

[102] T. Mizoguchi, and G. S. Cargill: *Magnetic anisotropy from dipolar interactions in amorphous ferrimagnetic alloys*, J. Appl. Phys. **50**, 3570 (1979)

[103] W. H. Meiklejohn: *Magnetooptics: A thermomagnetic recording technology*, Proc. IEEE. **74**, 1570 (1986)

[104] P. Hansen, C. Clausen, G. Much, M. Rosenkranz, and K. Witter: *Magnetic and magneto-optical properties of rare-earth transition-metal alloys containing Gd, Tb, Fe, Co*, J. Appl. Phys. **66**, 756 (1989)

[105] M. Nawate, K. Doi, and S. Honda: *Structure and perpendicular anisotropy in Gd/Fe multilayers sputter-deposited with substrate bias*, J. Magn. Magn. Mater. **126**, 279 (1993)

[106] J. Landes, Ch. Sauer, B. Kabius, and W. Zinn: *Critical thickness of the amorphous-nanocrystalline transition in Gd/Fe film structures*, Phys. Rev. B. **44**, 8342 (1991)

[107] H. Kiriake, F. Kato, M. Nawate, and S. Honda: *Magnetic property of Gd/Fe multilayers*, IEEE Trans. J. Magn.Jpn. **8**, 537 (1993)

[108] H. Fu, M. Mansuripur, and P. Meystre: *Generic source of perpendicular anisotropy in amorphous rare-earthtransition-metal films*, Phys. Rev. Lett. **66**, 1086 (1991)

[109] P. J. Jensen, and K. H. Bennemann: *Magnetic structure of films:Dependence on anisotropy and atomic morphology*, Surf. Sci. Rep. **61**, 129 (2006)

[110] N. C. Koon, B. T. Jonker, F. A. Volkening, J. J. Krebs, and G. A. Prinz: *Direct evidence for perpendicular spin orientations and enhanced hyperfine fields in ultrathin Fe(100) films on Ag(100)*, Phys. Rev. Lett. **59**, 2463 (1987)

[111] Z. Qiu, J. Pearson, and S. Bader: *Asymmetry of the spin reorientation transition in ultrathin Fe films and wedges grown on Ag(100)* , Phys. Rev. Lett. **70**, 1006 (1993)

[112] A. Berger, and H. Hopster: *Nonequilibrium Magnetization near the Reorientation Phase Transition of Fe/Ag(100) Films*, Phys. Rev. Lett. **76**, 519 (1996)

[113] M. A. Torija, J. P. Pierce, and J. Shen: *Magnetic capping layer induced spin reorientation: Co on Fe/Cu(100)*, Phys. Rev. B **63**, 092404 (2001)

[114] D. Peterka, A. Enders, G. Haas, and K. Kern: *Adsorbate and thermally induced spin reorientation transition in low-temperature-grown Fe/Cu(001)*, Phys. Rev. B. **66**, 104411 (2002)

[115] A. Enders, D. Peterka, D. Repetto, N. Lin, A. Dmitriev, and K. Kern: *Temperature Dependence of the Surface Anisotropy of Fe Ultrathin Films on Cu(001)*, Phys. Rev. Lett. **90**, 217203 (2003)

[116] R. Allenspach, M. Stampanoni, and A. Bischof: *Magnetic domains in thin epitaxial Co/Au(111) films* , Phys. Rev. Lett. **65**, 3344 (1990)

[117] L. Cagnon, T. Devolder, R. Cortes, A. Morrone, J. E. Schmidt, and C. Chappert: *Enhanced interface perpendicular magnetic anisotropy in electrodeposited Co/Au(111) layers*, Phys. Rev. B. **63**, 104419 (2001)

[118] R. Sellmann, H. Fritzsche, H. Maletta, V. Leiner, and R. Siebrecht: *Spin-reorientation transition and magnetic phase diagrams of thin epitaxial Au(111)/Co films with W and Au overlayers*, Phys. Rev. B. **64**, 054418 (2001)

[119] C. S. Arnold, D. P. Pappas, and A. P. Popov: *Second and first-order phase transitions in the magnetic reorientation of ultrathin Fe on Gd* , Phys. Rev. Lett. **83**, 3305 (1999)

[120] J. W. Lee, J. R. Jeong, S. C. Shin, J. Kim, and S. K. Kim: *Spin-reorientation transitions in ultrathin Co films on Pt(111) and Pd(111) single-crystal substrates*, Phys. Rev. B. **66**, 172409 (2002)

[121] D. Matsumura, T. Yokoyama, K. Amemiya, S. Kitagawa, and T. Ohta: *X-ray magnetic circular dichroism study of spin reorientation transitions of magnetic thin films induced by surface chemisorption* , Phys. Rev. B. **66**, 024402 (2002)

[122] J. W. Lee, J. Kim, S. K. Kim, J. R. Jeong, S. C. Shin: *Full vectorial spin-reorientation transition and magnetization reversal study in ultrathin ferromagnetic films using magneto-optical Kerr effects*, Phys. Rev. B. **65**, 144437 (2002)

[123] M. Kisielewski, A. Maziewski, M. Tekielak, J. Ferre, S. Lemerle, V. Mathet, and C. Chappert: *Magnetic anisotropy and magnetization reversal processes in Pt/Co/Pt films*, J. Magn. Magn. Mater. **260**, 231 (2003)

[124] E. Stavrou, H. Rohrmann, and K. Röll: *Gd/Fe multilayers with an anisotropy changing from in-plane to perpendicular for MSR application*, IEEE Trans. Magn. **34**, (1998)

[125] E. Stavrou, and K. Röll: *Magnetic anisotropy in Gd/(FeCo) and Gd/Fe multilayers for high density magneto-optical recording*, J. Appl. Phys. **85**, 5971 (1999)

[126] E. Stavrou, R. Sbiaa, T. Suzuki, and K. Röll: *Different mechanisms of spin reorientation in exchange coupled double rare earth-transition metal layers with in-plane and perpendicular magnetic anisotropy*, J. Appl. Phys. **87**, 6893 (2000)

[127] E. Stavrou, R. Sbiaa, T. Suzuki, S. Knappmann, and K. Röll: *Magnetic anisotropy and spin reorientation effects in Gd/Fe and Gd/(FeCo) mutilayers for high density magneto-optical recording*, J. Appl. Phys. **87**, 6899 (2000)

[128] G. S. Cargill, and T. Mizoguchi: *Dipolar mechanisms for magnetic anisotropy in amorphous ferrimagnetic alloys*, J. Appl. Phys. **49**, 1753 (1978)

[129] T. Mizoguchi, and G. S. Cargill: *Magnetic anisotropy from dipolar interactions in amorphous ferrimagnetic alloys*, J. Appl. Phys. **50**, 3570 (1979)

[130] Raasch: *Magnetische wandenergien und austauschkonstanten in amorphen seltenerd übergangsmetalldünnfilmschiten*, (Verlag der Augustinus Buchhandlung, Aachen, 1995)

[131] E. Y. Vedmedenko, H. P. Oepen, and J. Kirschner: *Microstructure of the spin reorientation transition in second-order approximation of magnetic anisotropy* , Phys. Rev. B **66**, 214401 (2002)

[132] T. Miyazaki, K. Hayashi, S. Yamaguchi, Migaku Takahashi, A. Yoshihara, T. Shimamori, and T. Wakiyama: *Magnetization, Curie temperature and perpendicular magnetic anisotropy of evaporated Fe-rare earth amorphous alloy films*, J. Magn. Magn. Mater. **75**, 243 (1988)

[133] T. C. Ulbrich, D. Makarov, G. Hu, I. L. Guhr, D. Suess, T. Schrefl, and M. Albrecht: *Magnetization Reversal in a Novel Gradient Nanomaterial*, Phys. Rev. Lett. **96**, 077202 (2006)

[134] www.bangslabs.com Bangs Laboratories, Inc. 9025 Technology Drive Fishers, IN 46038-2886

[135] R. Micheletto, H. Fukuda, and M. Ohtsu: *A simple method for the production of a two-dimensional, ordered array of small latex particles*, Langmuir. **11**, 3333 (1995)

[136] W. Kern: *Handbook of Semiconductor Cleaning Technology* (Noyes Publishing, Park Ridge, NJ, 1993), Chap. 1, p. 20

[137] S. Landis, B. Rodmacq, and B. Dieny: *Magnetic properties of Co/Pt multilayers deposited on silicon dot arrays*, Phys. Rev. B. **62**, 12271 (2000)

[138] M. Takagaki, A. Koizumi, N. Kawamura, M. Suzuki, and N. Sakai: *Element-specified observation of surface-influenced magnetization process in Gd/Fe multilayer*, J. Phys. Soc. Jpn. **72**, 245 (2003)

[139] A. Koizumi, M. Takagaki, M. Suzuki, N. Kawamura, and N. Sakai: *Anomalous magnetic hysteresis of Gd and Fe moments in a Gd/Fe multilayer measured by hard x-ray magnetic circular dichroism* , Phys. Rev. B. **61**, R14909 (2000)

[140] M. S. S. Brooks, T. Gasche, S. Auluck, L. Nordström, L. Severin, J. Trygg, and B. Johansson: *Ab initio calculation of molecular field interactions in rare-earth transition-metal intermetallics* , J. Appl. Phys. **70**, 5972 (1991)

[141] P. Wadhwa, and M. B. A. Jalil: *Micromagnetic modeling and analysis of linear array of square nanomagnets*, J. Magn. Magn. Mater. **294**, 83 (2005)

[142] T. Aign, P. Meyer, S. Lemerle, J. P. Jamet, J. Ferre, V. Mathet, C. Chappert, J. Gierak, C. Vieu, F. Rousseaus, H. Launois, and H. Bernas: *Magnetization reversal in arrays of perpendicularly magnetized ultra thin dots couples by dipolar interaction*, Phys. Rev. Lett. **81**, 5656 (1998)

[143] O. Iglesias, and A. Labarta: *Influence of surface anisotropy on the hysteresis of magnetic nanoparticles*, Phys. Stat. Sol. **12**, 3481 (2004)

[144] J. M. Wesselinowa, and I. Apostoliva: *Size, anisotropy and doping effects on the coercive field of ferromagnetic nanoparticle*, J. Phys. Condens. Matter **19**, 406235 (2007)

[145] X. Zianni, K. N. Trohidou, and J. A. Blackman: *Effect of surface anisotropy on the Coercive field of small magnetic particle*, J. Appl. Phys. **81**, 4739 (1997)

[146] H. Kachkachi, and M. Dimian: *Hysteresis properties of a magnetic particle with strong surface anisotropy*, Phys. Rev. B. **66**, 174419 (2002)

[147] A. N. Bogdanov, U. K. Rössler, and K. H. Müller: *Theory of induced uniaxial anisotropy in magnetic nanostructures*, J. Magn. Magn. Mater. **242-245**, 594 (2002)

[148] A. N. Bogdanov, and U. K. Rössler : *Chiral symmetry breaking in magnetic thin films and multilayers*, Phys. Rev. Lett. **87**, 037203 (2001)

[149] W. C. Uhlig, and J. Shi: *Systematic study of the magnetization reversal in patterned Co and NiFe nanolines*, Appl. Phys. Lett. **84**, 759 (2004)

[150] E. Y. Vedmedenko, H. P. Oepen, and J. Kirschner: *Size-dependent spin reorientaion transition in nanoplatelets*, Phys. Rev. B. **67**, 012409 (2003)

[151] A. Maziewski, V. Zablotskii, and M. Kisielewski: *Geometry-driven out-of-plane magnetization states in nanostructures*, Phys. Rev. B. **73**, 134415 (2006)

[152] M. Kisielewski, A. Maziewski, and V. Zablotskii: *Magnetization distributions in nano-sized ultrathin cobalt*, J. Magn. Magn. Mater. **290-291**, 776 (2005)

[153] M. Kisielewski, A. Maziewski, V. Zablotskii, and W. Stefanowicz: *Micromagnetic simulations and analytical description of magnetic configurations in nanosized magnets*, Physica B. **372**, 316 (2006)

[154] S. Hashimoto, Y. Ochiai, and K. Aso: *Perpendicular magnetic anisotropy and magnetostriction of sputtered Co/Pd and Co/Pt multilayered films*, J. Appl. Phys. **66**, 4909 (1989)

[155] C. J. Lin, G. L. Gorman, C. H. Lee, R. F. C. Farrow, E. E. Marinero, H. V. Do, and H. Notarys: *Magnetic and structural properties of Co/Pt multilayers*, J. Magn. Magn. Mat. **93**, 194 (1991)

[156] J. H. Kim, and S. C. Shin: *Interface roughness effects on the surface anisotropy in Co/Pt multilayer films*, J. Appl. Phys. **80**, 3121 (1996)

[157] V. W. Guo, B. Lu, X. Wu, G. Ju, B. Valcu, and D. Weller: *A survey of anisotropy measurement techniques and study of thickness effect on interfacial and volume anisotropies in Co/Pt multilayer media*, J. Appl. Phys. **99**, 08E918 (2006)

[158] T. C. Ulbrich: *Co/Pd und Co/Pt Schichtsysteme auf Partikelmonolagen*, Ph.D. thesis, University of Konstanz, (2007)

[159] T. Eimüller, T. C. Ulbrich, E. Amaladass, I. L. Guhr, T. Tyliszczak, and M. Albrecht: *Spin-reorientation transition of Co/Pt multilayers on nanospheres*, Phys. Rev. B. **77**, 134415 (2008)

[160] Ch. Jooss, J. Albrecht, H. Kuhn, S. Leonhardt, and H. Krönmüller: *Magneto-optical studies of current distributions in high-T_c superconductors*, Rep. Prog. Phys. **65** 651 (2002)

[161] K. Yamada, S. Kasai, Y. Nakatani, K. Kobayashi, H. Kohno, A. Thiaville, and T. Ono:*Electrical switching of the vortex core in a magnetic disk*, Nat. Mater **6**, 270 (2007)

[162] V. P. Kravchuk, D. D. Sheka, Y. Gaididei, F. G. Mertens: *Controlled vortex core switching in a magnetic nanodisk by a rotating field*, J. Appl. Phys. **102** 043908 (2007)

[163] J. G. Caputo, Y. Gaididei, F. G. Mertens, D. D. Sheka: *Vortex polarity switching by a spin-polarized current*, Phy. Rev. Lett. **98** 056604 (2007)

[164] V. Sackmann: *Spindynamics in microstructured ferromagnetic elements*, Diploma thesis, University of Stuttgart, (2008)

[165] C. Huwiler, D. Falconnet, M. Halter, K. Rezwan, J. Vörös, and M. Textor: *Nanocolloidal Microarrays on Chemically Patterned Substrates*, Proceedings of 5th IEEE Conference on Nanotechnology Nagoya, Japan, (2005)

[166] K. Schmidt, H. G. Schoberth, M. Ruppel, H. Zettl, H. Hänsel, T. M. Weiss, V. Urban, G. Krausch, and A. Böker: *Reversible tuning of a block-copolymer nanostructure via electric fields*, Nat. Mater. **7** 142 (2008)

[167] M. Sastry: *Assembling nanoparticles and biomacromolecules using electrostatic interactions*, Pure Appl. Chem. **74**, 1621 (2002)

[168] H. Matsuura, M. Miyazaki, M. Komatsu, and M. Ogawa: *Self-alignment of glass spheres using the electromeniscus phenomenon*, Appl. Phys. Lett. **87**, 134106 (2005)

[169] M. E. Abdelsalam, P. N. Bartlett, J. J. Baumberg, and S. Coyle: *Preparation of arrays of isolated spherical cavities by self-assembly of polystyrene spheres on self-assembled pre-patterned macroporous films*, Adv. Mater. **16**, 90 (2004)

[170] D. G. Grier: *A revolution in optical manipulation*, Nat. **424**, 21 (2003)

Acknowledgement

I would like to thank all who have helped me in my PhD thesis, because without their help this work would not have been possible.

At first, I thank **God almighty** for his Grace and blessings. I thank **Prof. Dr. G. Schütz** for offering me this interesting topic and also for her guidance and motivation throughout my thesis.

I express my deep gratitude to my supervisor **Prof. Dr. Thomas Eimüller** for his kind support, valuable discussions, ideas and critics. I thank him specially for his friendly and simple nature and for being with me during the experiments at Advanced Light Source, Berkeley, CA, USA. Though he was away from the institute he has helped me lot.

I thank **Prof. Dr. G. Denninger** and **Prof. Dr. G. Mahler** for agreeing to be the referees of my thesis.

I thank all the staff members of ALS, especially **Dr. T. Tyliszczak**, beam line scientist at STXM, for his tremendous support during the experiments. I thank **Dr. A. Scholl** and **Mr. A. Doran**, beamline scientists at PEEM II, for their kind help at PEEM and also helping me a lot with the image analyzing software *PEEM vision*.

I thank **Dr. S. UthayKumar** and **Dr. S. P. Dash** for their support and discussions. I thank **Dr. G. Ballentine** and **Dr. J. Albrecht** for reading my thesis. I extend my gratitude to **Mr. S. Macke** at MPI-MF and **Mr. D. Makarov** at the University Konstanz for their kind help in finite element simulations. I would also thank **Dr. T. C. Ulbrich** for the Co/Pt samples and simulations.

I am greatly indebted to **Mr. B. Ludescher**, and **Mrs. T. Dragon** for sample preparation and assisting me at Kerr microscope. I thank **Mrs. S. Kühnemann** for SEM analysis, **Dr. U. Welzel** and **Mrs. M. Dudek** for XRR analysis. I would also thank **Dr. P. Van Aken** and **Mr. P. Kopold** for TEM analysis. I extend my gratitude to all the co-workers in Max Planck Institute, Stuttgart. A special thanks to **Dr. B. Baretzky**, manager of department Schütz and **Mrs. M. Kotz**, secretary, for taking care of all administrative issues.

Out of the academic circle there are lots of hearts whom I should thank. I thank **Rev. Fr. Dr. Roy Lazar** who has supported me all the way since the beginning of my studies.

I thank **Family Butscher** and **Family Arnold**, especially **Mrs. Margit Butscher** and **Mr. Roland Butscher** for helping me in all the ways possible. I thank them for their moral support by sharing my happiness, difficulties and sorrows, for the delicious German dishes on my every visit and also for taking me for a walk that kept me fit. Thanks a lot.

I am greatly indebted to **Mr. Thomas Arul Anand** for helping me a lot during the beginning of my studies in Germany.

Especially I thank my parents **Mr. K. Amaladass** and **Mrs. M. Rani**, for their love and support in all my effort, and giving me the foundation to be who I am. Thank you Appa and Amma. I thank all my relatives, my brothers **A. Dhayalan, A. Sengkuttuvan** and my sister **A. Ephrem Rabia** for their care and affection.

I thank all my friends in India and in Germany for making life enjoyable and cheerful. A special thanks to **Saravanan and Kavya**, **Rajiv**, **Sathish**, **Roshan and his family**, and **Marood and his family**.

Last but not least I thank my loving fiancee **Sahayarani** for the love, support and patience throughout this journey.